

The Multi-layer Nature of Molecular Gas toward the Cygnus Region

SHIYU ZHANG,^{1,2} YANG SU^{†, 1,2} XUEPENG CHEN,^{1,2} MIN FANG,^{1,2} QINGZENG YAN,¹ SHAOBO ZHANG,¹ YAN SUN,^{1,2}
 XIAOLONG WANG,^{3,*} HAORAN FENG,^{1,2} YUEHUI MA,¹ MIAOMIAO ZHANG,¹ ZI ZHUANG,^{1,2} XIN ZHOU,¹ ZHIWEI CHEN,¹ AND
 JI YANG¹

¹Purple Mountain Observatory and Key Laboratory of
 Radio Astronomy, Chinese Academy of Sciences, Nanjing 210034,
 People's Republic of China

²School of Astronomy and Space Science, University of
 Science and Technology of China, 96 Jinzhai Road, Hefei 230026,
 People's Republic of China

³Department of Physics, Hebei Normal University,
 Shijiazhuang 050024, People's Republic of China

ABSTRACT

We study the physical properties and 3D distribution of molecular clouds (MCs) toward the Cygnus region using the MWISP CO survey and Gaia DR3 data. Based on Gaussian decomposition and clustering for ¹³CO lines, over 70% of the fluxes are recovered. With the identification result of ¹³CO structures, two models are designed to measure the distances of the molecular gas in velocity crowding regions. The distances of more than 200 large ¹³CO structures are obtained toward the 150 square degree region. Additionally, tens of the identified MC structures coincide well with masers and/or intense mid-IR emission. We find multiple gas layers toward the region: (1) the extensive gas structures composing the Cygnus Rift from 700 pc to 1 kpc across the whole region; (2) the ~ 1.3 kpc gas layer mainly in the Cygnus X South region; and (3) the 1.5 kpc dense filament at the Cygnus X North region and many cometary clouds shaped by Cygnus OB2. We also note that the spatial distribution of YSO candidates is generally consistent with the molecular gas structures. The total molecular mass of the Cygnus region is estimated to be $\sim 2.7 \times 10^6 M_{\odot}$ assuming an X-factor ratio $X_{\text{CO}} = 2 \times 10^{20} \text{ cm}^{-2} (\text{K} \cdot \text{km} \cdot \text{s}^{-1})^{-1}$. The foreground Cygnus Rift contributes ~25% of the molecular mass in the whole region. Our work presents a new 3D view of the MCs distribution toward the Cygnus X region, as well as the exact molecular gas mass distribution in the foreground Cygnus Rift.

Keywords: Distance measure (395) — Interstellar medium (847) — Molecular clouds (1072)

1. INTRODUCTION

CO surveys are of great importance and helpful for studying MCs directly and coordinating Galactic emission at multiple wavelength bands (Heyer & Dame 2015). Particularly, stars are born in the densest parts of MCs, therefore studies of MCs can accelerate our understanding of the link between star formation and the surrounding molecular gas environment, as well as the large scale structures of the Milky Way (Dame et al. 2001; Umemoto et al. 2017; Schuller et al. 2017).

As one of the most massive nearby star formation region (SFR) (Reipurth & Schneider 2008), the Cygnus region harbors giant MC complexes (e.g., DR21, Schneider et al. 2010; Cao et al. 2022) and several OB associations (e.g., the well-known Cygnus OB2, Massey & Thompson 1991; Knöldlseder 2000; Comerón et al. 2002; Hanson 2003; Wright et al. 2010b, 2015). With Cygnus OB2 in the center, Cygnus X region is divided into the northern and southern parts by Schneider et al. (2006). Hundreds of OB stars toward this region indicate intense star formation activity therein,

Corresponding author: Yang Su

yangsu@pmo.ac.cn

* Physics Postdoctoral Research Station at Hebei Normal University

including extended ionized features from HII regions and supernova remnants (SNRs) (Wendker et al. 1991; Anderson et al. 2014), interstellar bubbles (Abbott et al. 1981; Higgs et al. 1994), and outflows (Duarte-Cabral et al. 2013; Zhang et al. 2020).

We focus on molecular gas in the whole Cygnus region, especially the gas emission within 1 kpc. Including Cygnus X (Schneider et al. 2006), North America/Pelican (NAP, Zhang et al. 2014), and other interesting regions. The Cygnus X region is prominent by its strong and extended Galactic radio continuum emission (Downes & Rinehart 1966; Wendker et al. 1991). The multiple wavelength studies are also fruitful, e.g. CO surveys (Dame et al. 1987; Schneider et al. 2006; Gottschalk et al. 2012; Yamagishi et al. 2018), CII (Schneider et al. 2023; Bonne et al. 2023), millimeter continuum (Motte et al. 2007; Bontemps et al. 2010), and infrared (Egan et al. 1998; Beerer et al. 2010; Hennemann et al. 2012; Schneider et al. 2016; Cao et al. 2019). Recently, many new works have also been presented toward the region (e.g., Takekoshi et al. 2019; Comerón et al. 2020; Ortiz-León et al. 2021; Quintana & Wright 2021, 2022; Beuther et al. 2022; Dharmawardena et al. 2022; Gong et al. 2023). The NAP region is located adjacent to the massive star-forming regions of Cygnus X in projection. L935 is the densest dark cloud in this region, which separates the North America and Pelican nebulae (see Figure 1). Evidence of the star formation process across the complex has been revealed by studying MCs and young stellar objects (YSOs) (Zhang et al. 2014; Fang et al. 2020).

Although the Cygnus region has been extensively studied in multiwavelengths, the distances and properties of clouds in the region are not well determined in a global view. Distance uncertainty is one of the major problems in studying the various star forming regions and gas structures/properties in the direction.

The distances of MCs have been subject of considerable debate with several difficulties. Firstly, it's hard to derive the kinematic distances of clouds because the near-far distance ambiguities in the first quadrant (Mertsch & Vittino 2021). In fact, the kinematic distances of MCs produce a large uncertainty when the velocity field of gas is crowding in a small velocity range (Yan et al. 2020). On the other hand, due to the large degree of overlap between inner and outer Galaxy along the line of sight (LOS), coherent MCs are difficult to be distinguished in position-position-velocity (PPV) space. Particularly, toward the Cygnus X region, a collective cloud emission across tangential point overlaps with each other from several hundred parsec (pc) to 2 kpc and even further in LSR velocities close to zero and velocity gradient smaller than the typical velocity dispersion of interstellar gas (Reipurth & Schneider 2008).

Some methods have been used to deal with the kinematic distance ambiguities. Different layers may be demonstrated based on the HI self-absorption features toward the Cygnus X (Gottschalk et al. 2012). The distances of some massive star formation regions (MSFRs) have been precisely determined by trigonometric parallax of the associated masers (Rygl et al. 2012; Xu et al. 2016). These methods are limited by the small amount of observed samples and can only focus on some small specific areas, thus lacking overall understanding of the whole region.

Before Gaia's age, large distance uncertainties of MCs by photometric methods prevented determining the exact 3D distribution of molecular gas. Thanks to the release and convenient acquisition of Gaia DR3 data, huge amounts of stars with parallaxes and extinctions make it possible to accurately measure the distance of MCs. For example, all sky extinction maps are derived by different models based on dust properties (Chen et al. 2019; Green et al. 2019; Lallement et al. 2019; Hottier et al. 2020). In addition, extinction jump models are applied to distance measurements of MCs (Yan et al. 2019b; Zucker et al. 2019; Sun et al. 2021a; Guo et al. 2022), and SNRs (Zhao et al. 2020; Yu et al. 2019). Toward the Cygnus X region, Orellana et al. (2021) revealed that the OB2 association consists of several sub-structures, ranging from 1.2 kpc to 1.7 kpc based on Gaia DR2 data. The above evidences suggest that the gas and the SFRs toward the direction is a chance superposition of several complexes along the LOS.

Finally, ultra-high energy (UHE) cosmic rays emissions are prevalent in our Galaxy (Cao et al. 2021; Banik & Ghosh 2022). Several UHE sources are detected toward the Cygnus X region (Cao et al. 2023). The origin of these UHE sources is still unknown. Are they from hadronic processes from the interaction of high velocity winds of massive stars (e.g. Cygnus OB2) and/or SNR shock (e.g. γ -Cyg) with the surrounding dense molecular gas? Evaluating the molecular gas distribution toward the Cygnus region might be helpful to reveal the possible origin of UHE emission.

This paper is structured as follows. We will introduce the MWISP CO survey and the Gaia DR3 in Section 2. The data processing methods are described in detail, including Gaussian decomposition in Section 3.1 and the clustering algorithm in Section 3.2. In Section 4, we determined the distances and physical properties of identified ^{13}CO structures. Based on our new distance measurement of MCs, we introduce the physical properties and the 3D distribution of gas structures for several sub-regions in Section 5, and later in Section 6, we mainly focus on molecular gas in the Cygnus Rift, and discuss the big picture of MCs in different layers and estimate the total molecular mass. Finally we give our summary in Section 7. More details of techniques can be seen in Appendixes.

2. DATA

2.1. CO data

The Milky Way Imaging Scroll Painting (MWISP, [Su et al. 2019](#)) project is an ongoing CO survey by using the PMO-13.7 m millimeter-wavelength telescope at Delingha, China. The survey observes ^{12}CO , ^{13}CO and C^{18}O simultaneously toward the northern Galactic plane. The first epoch (MWISP I) has been completed from 2011 to 2021 for the whole region of $10^\circ \leq l \leq 230^\circ$, $|b| \leq 5^\circ$. The MWISP II is launching toward $5^\circ \leq |b| \leq 10^\circ$.

The PMO-13.7 m telescope uses the 3×3 multi-beam side band-separating Superconducting Spectroscopic Array Receiver (SSAR) system (see details in [Shan et al. 2012](#)). Briefly, the total bandwidth of the receiver is 1 GHz with 16,384 channels, providing a frequency interval of 61 kHz and covering a velocity range of $2700 \text{ km} \cdot \text{s}^{-1}$. The channel separations (RMS level) of the data are $0.158 \text{ km} \cdot \text{s}^{-1}$ ($\sim 0.48 \text{ K}$) for ^{12}CO and $\sim 0.166 \text{ km} \cdot \text{s}^{-1}$ ($\sim 0.25 \text{ K}$) for ^{13}CO and C^{18}O , respectively. With moderate spatial resolution ($\sim 51''$), the three-dimensional (3D) FITS data cubes of each cell ($30' \times 30'$) were made with a grid spacing of $30''$.

A preliminary analysis on the noise characteristics ([Cai et al. 2021](#)) has been done to increase the quality of data, including removing bad channels, decreasing edge effects, and correcting baseline distortion.

In this paper, the data cube to Cygnus is clipped in the range, $l: 72 \sim 87 \text{ deg}$, $b: -5.1 \sim 5.1 \text{ deg}$, $v: -100 \sim 50 \text{ km} \cdot \text{s}^{-1}$. We resampled the velocity channels of all three lines to $0.2 \text{ km} \cdot \text{s}^{-1}$ (the corresponding RMS level is 0.42 K for ^{12}CO , 0.22 K for ^{13}CO and C^{18}O) to reduce the bias in data processing. The resultant data are in $-45 \sim 40 \text{ km} \cdot \text{s}^{-1}$, covering the major emission of Cygnus (see Figure 1 and 2).

2.2. Gaia DR3

We use the photometric data and parallaxes from Gaia DR3, which was released in June 13th, 2022 ([Creevey et al. 2023; De Angeli et al. 2023; Andrae et al. 2023](#)). In total, 1.8 billion objects have source classification and probabilities in DR3. Over 470 million sources have astrophysical characterisations from General Stellar Parameterizer from Photometry (GSP-Phot) results for apparent magnitude $G \leq 19$. In our CO coverage, 1,730,905 stars are included with parallax over error larger than 5. Stars with very small A_G errors ($\leq 0.01 \text{ mag}$, see details in Section 4.2.2) are discarded. Finally 1,362,839 stars are used for following MC distance measurement.

Assuming a constant $R_0 = 3.1$, the interstellar extinction was applied to the model grid according to [Fitzpatrick \(1999\)](#). We take A_G from the GSP-Phot results. The reddened spectral energy distributions (SEDs) are integrated over Gaia G pass-band, and the derived magnitude can be compared to the corresponding value without extinction ([Andrae et al. 2023](#)). For estimating the geometric distances from parallaxes, we use a simple Monte Carlo sampling to inverse the parallaxes. Statistical comparisons of distances with different methods have been done by following the work of [Luri et al. \(2018\)](#). We find all methods give consistent results (see Appendix C for detailed analysis).

3. CLOUD IDENTIFICATION

MCs often display extended and irregular morphology. Some clouds show intricate hierarchical morphology, characterized by filamentary networks and clumpy structures. So how to describe or define the structure of a MC need to be explored.

Many agglomerative clustering algorithms have been proposed and applied to construct MC samples from various CO surveys. The Dendrogram ([Rice et al. 2016](#)) is applied to CO data from CfA-Chile 1.2m survey ([Dame et al. 2001](#)). SCIMES is used in various CO lines surveys, for example, ^{12}CO (1-0) from the MWISP ([Ma et al. 2021](#)), ^{12}CO (3-2) from the JCMT CO (3-2) High-Resolution Survey ([Colombo et al. 2019](#)) and ^{13}CO (2-1) from the SEDIGISM ([Duarte-Cabral et al. 2021](#)). Recently, [Yan et al. \(2021b\)](#) provided a catalogue of MCs based on DBSCAN and ^{12}CO data in the MWISP.

Different from the above methods, [Miville-Deschénes et al. \(2017\)](#) used a hierarchical cluster identification method to extract MC samples based on Gaussian decomposition. [Hacar et al. \(2013\)](#) characterized C^{18}O velocity coherent components in PPV space by using the friends in velocity (FIVE) algorithm. And [Henshaw et al. \(2019\)](#) used agglomerative clustering to organize nested structures (ACORNS). Due to the complicated velocity structures in Cygnus, we adopt the ACORNS algorithm based on Gaussian decomposition, and apply it to extract MC structures based on the ^{13}CO emissions from the MWISP survey (Section 3.2).

3.1. Gaussian decomposition

Gaussian decomposition has been widely applied to the fitting of various spectral lines, e.g., HI: (Marchal et al. 2019; Panopoulou & Lenz 2020); ^{12}CO : (Miville-Deschénes et al. 2017); ^{13}CO : (Riener et al. 2020); C^{18}O : (Clarke et al. 2018); HNCO: (Henshaw et al. 2019); OH: (Petzler et al. 2021); NH_3 : (Sokolov et al. 2020), etc. There are several manual tools to fit the spectra, such as Pyspeckit (Ginsburg & Mirocha 2011; Ginsburg et al. 2022), ScousePy (Henshaw et al. 2019), etc. And automatic fitting methods are also developed, such as GaussPy+ (Riener et al. 2019), Amoeba (Petzler et al. 2021), and other methods (e.g., Sokolov et al. 2020).

Manual fitting methods are often applied to small data sets (Henshaw et al. 2019), especially with prior understanding of the data. However, once the amount of data becomes large, it's really a time-consuming work for manual fitting. Additionally, the fitting results might be biased because of human factors. Therefore automatic fitting methods are better suited for large-scale data analysis, such as the MWISP survey.

In the case of sufficient computing resources, the fitting results can be quickly obtained. Then one or more sets of fitting parameters for each pixel are obtained, such as centroid velocity $v_{0,i}$, full width at half maximum ($\text{FWHM}=\sqrt{8\log(2)}\sigma_i$), and peak intensity A_i . In this way, spectral line data of each pixel can be described by several parameters, leading to clear presentation of line intensities and spatial relations among different velocity components. For example, Henshaw et al. (2020) has obtained the velocity structure of molecular gas at different scales by fitting the centroid velocities of multiple lines, and found the fluctuation and periodicity everywhere. Without spectral fitting, such interesting results cannot be obtained from the original PPV data due to the effects of line broadening and blending velocity components.

In this work, we use GaussPy+ module proposed and improved by Riener et al. (2019) to fit and decompose the ^{13}CO lines. The ^{13}CO data is chosen because it's usually optically thin (e.g., Wang et al. 2023; Yuan et al. 2023) and more favorable to trace the inner structure of the MCs. Moreover, Yuan et al. (2022) shows that ^{13}CO emitting area of a large scale cloud can cover $\sim 30\%$ of the corresponding ^{12}CO area. It indicates that ^{13}CO is actually a good tracer to reveal large MCs (also see Su et al. 2020; Wang et al. 2023). In the same time, ^{13}CO spectral lines are often relatively velocity separated compared to ^{12}CO line profile for different MCs. All these features can largely mitigate overfitting problems.

Study on giant molecular clouds (GMCs) in Orion B (Bron et al. 2018) proves that $J = 1-0$ lines of three isotopologues of CO are good at revealing distinct density regimes. In a data-driven approach, Gratier et al. (2021) found that the ^{13}CO line from Orion B cloud is effective for the estimation of the column density in various environments, especially for translucent gas ($2 \leq Av \leq 5$). For clouds traced by ^{13}CO emission, its extinction is neither too large nor too small. Actually the MWISP survey shows that ^{13}CO emission can trace the molecular gas in a range of $N_{\text{H}_2} \sim 3 \times 10^{21} \text{ cm}^{-2}$ to several 10^{22} cm^{-2} (Ma et al. 2021; Wang et al. 2023). As a result it is helpful for distance measurement based on MC samples identified from ^{13}CO emission. Finally, different molecular structures can be well distinguished for velocity-crowded regions using ^{13}CO data.

Based on our experiments, we adopt the following parameters:

1. Signal-to-noise ratio. We set the signal to 5 RMS to skip those weak emission. Signals with level $\gtrsim 1.2 \text{ K}$ are remained;
2. Minimum FWHM. We set it to be at least 2 channels ($0.4 \text{ km} \cdot \text{s}^{-1}$) for the MWISP data;
3. Maximum FWHM. We didn't set this parameter before fitting.
4. Smoothing parameter. We take the optimal smoothing parameters (i.e., $\alpha_1 = 2.18$, $\alpha_2 = 4.94$, Riener et al. 2020) for the MWISP.

For each pixel at sky position, the brightness temperature $T'_B(l, b, v)$ is described as the sum of all Gaussian components, and the total intensity $W_{\text{CO}}(l, b)$ as a function of velocity v is in the form:

$$T'_B(l, b, v) = \sum_{i=1}^N A_i e^{-\frac{(v - v_{0,i})^2}{2\sigma_i^2}} \quad (1)$$

and,

$$W_{\text{CO}}(l, b) = \sum_i^N \int A_i e^{-\frac{(v - v_{0,i})^2}{2\sigma_i^2}} dv = \sqrt{2\pi} \sum_i^N A_i \sigma_i \quad (2)$$

where A_i , $v_{0,i}$ and σ_i is the amplitude, centroid velocity and width of each Gaussian component, respectively.

Our data cube includes 1,801*1,225 (2,206,225) pixels, among which 17.5% of the pixels have been fitted by GaussPy+. According to the fitted results, we can discern some molecular cloud structures by combining the pixels with a coherent single velocity component (see Figure 2g). 79.7% of pixels have only one velocity component along the LOS in the fitted pixels. 14.1% pixels have two and 5% pixels have three components. Only 1.2% pixels are more than three components among fitted pixels. The pixels with two components mainly located in the boundaries of different MC structures (see Figure 2g), showing superposition between them. Pixels with multiple components (≥ 3) are located near the Galactic disk, revealing the crowded velocities therein.

For the whole map, we apply a moment masking criteria (1. pixels within the ^{12}CO emission structure and 2. pixels with three consecutive channels larger than 3 times the noise RMS) to estimate the total valid flux of the raw data. The identification of ^{12}CO emission was following DBSCAN algorithm (see details in Yan et al. 2021a). The total recovered flux from Gaussian reconstruction makes up 74.3% of the flux of the raw data. And we reconstruct the integrated intensity map from the Gaussian fitting shown in Figure 2a. The distribution of other Gaussian parameters (e.g., centroid velocities, velocity dispersion, fitted components numbers and residuals between the reconstructed map and raw image) is presented in Figure 2 c-h.

3.2. Clustering

As mentioned above, many MCs in the Cygnus region display hierarchical structures and nested velocity components along the LOS. And Henshaw et al. (2019) summarized that a single MC structure has the features to be coherent in both space, velocity, and velocity dispersion. In other words, MC structures separated by ACORNS are different from each other in physical properties and statistics. For the Gaussian decomposed ^{13}CO data cube, ACORNS can effectively avoid line blending effects along the LOS, and successfully separating molecular gas emission toward the Cygnus region into substructures. However, the definition of MCs has been debated for decades and as indicated in some simulations (e.g., Zamora-Avilés et al. 2017; Clarke et al. 2018). We will give some discussions in Section 6.3.

We made parametric tuning on the algorithm implemented in the MWISP data. In order to avoid the influence of noise and highlight the major structure, we only focus on the structures with relatively strong emission and large angular areas. As the signal is set to 5 times the noise RMS in Section 3.1, the decomposition results are reliable for clustering. In order to further develop the hierarchy and to reduce over decomposition, we specify the “relax” step. After manually comparing the identified cloud structure with the coherent characteristics of the raw data, a group of parameters are adopted in ACORNS here:

1. *min_radius*. We set it to be a bit smaller than 2 pixel. It ensures that the smallest structure in clustering result has ≥ 9 pixels;
2. *velo_link*. We set it to $0.2 \text{ km} \cdot \text{s}^{-1}$ based on resampled data;
3. *dv_link*. The line width link parameter is set to $0.4 \text{ km} \cdot \text{s}^{-1}$;
4. The coefficients of relax step is set to [3, 2, 0.5] times the cluster criteria (as default if “relax” was activated);
5. The stop criteria is set to 3.

Then, the algorithm further eliminates some small structures that are not merged into the adjacent large structures. Finally the MC samples with coherent ^{13}CO emission are constructed based on the above steps.

After adding another loop to the clustering process (details in Appendix E), 72.6% of the flux is recovered compared to the raw data. It indicates that a large proportion of flux restored by both of Gaussian decomposition (Figure 2a) and clustering (Figure 2b). We find that only small fraction of emission ($\approx 1.7\%$) fails to merge into branches.

Different from the other methods (e.g. SCIMES, Dendrogram, DBSCAN, etc.), we mainly use the results of Gaussian fitting and the ACORNS clustering algorithm to produce the cloud table, so the definition of cloud boundary is different in the spatial projection and in the direction of velocity. In the plane perpendicular to the LOS, the boundary of the cloud can be determined by aggregating all pixel locations. In the forest of clusters, each tree corresponds to a cloud structure. For a tree with a hierarchical structure (with branches and leaves for large scale structures), cloud is a complex that is composed of discrete, non-overlapping substructures. For a tree with no hierarchy, the cloud is an uniform and coherent structure. In either cases, the positions of the outermost pixels form the boundary of the cloud

in the projection plane. In the LOS direction, the Gaussian fitted line width of each component corresponds to the “velocity thickness” of the cloud. For simplicity, we take the position of the line centroid velocity $\pm 3\sigma_v$ (see equation (9)) as the range of cloud in the velocity direction. According to the above clustering criterion, the velocity boundary of adjacent pixels is also similar, so that the cloud in PPV space has a relatively smooth contour.

3.3. Check identified structures

For comparisons, we plot an average spectrum that illustrates the total emission intensity reproduced by GaussPy+ (blue line in Figure 3) as well as clouds clustering (red line in Figure 3). The total integrated intensity reconstructed by fitting components and clustering account for 81.5% and 79.5% of flux (black line in Figure 3), respectively, for all fitted pixels based on Gaussian decomposition (see Section 3.1). Note that the flux of all fitted pixels here is $\sim 10\%$ smaller than the flux of the whole region.

In the Cygnus X North region, the widely studied filament DR21 with HII regions is extracted, as well as other globular structures with brightness temperatures in the vicinity (see Section 5.1). In the Cygnus X South region, a large cloud is identified with a straight clubbed body and waterfall-like arms adjoin in its center (later on we call it L889, see Section 5.2). The filamentary cloud L914 is divided into two segments because the centroid velocity turns sharply between the two MC structures (see Section 5.4). As a typical sub-region with relatively simple velocity components, the identified cloud of L914 after clustering restores about 77% flux of the raw data in a moment masking method (larger than the average 72.6%).

3.4. Cloud parameters

Based on cloud identification from ^{13}CO emission, there is only one single Gaussian component along the LOS in each coherent structure. For a structure with pixels number n_{pixels} , the integrated intensity of the j -th component: $W_{\text{CO}}^{\text{cloud}}(l_j, b_j) = W_{\text{CO}}^j$. Here we define intensity-weighted coordinates of identified structures, with:

$$l_0 = \frac{\sum_j W_{\text{CO}}^j l_j}{\sum_j W_{\text{CO}}^j} \quad (3)$$

and,

$$b_0 = \frac{\sum_j W_{\text{CO}}^j b_j}{\sum_j W_{\text{CO}}^j} \quad (4)$$

The total intensity of cloud is $W_{\text{CO}}^{\text{cloud}} = \sum_j W_{\text{CO}}^j$. The standard deviation along l and b is:

$$\sigma_l = \sqrt{\frac{\sum_j W_{\text{CO}}^j (l_j^2 - l_0^2)}{\sum_j W_{\text{CO}}^j}} \quad (5)$$

and,

$$\sigma_b = \sqrt{\frac{\sum_j W_{\text{CO}}^j (b_j^2 - b_0^2)}{\sum_j W_{\text{CO}}^j}} \quad (6)$$

The total brightness temperature of a cloud at v is provided by summing of all pixels in the identified boundary:

$$T_B^{\text{cloud}}(v) = \sum_j A_j e^{-\frac{(v - v_{0,j})^2}{2\sigma_j^2}} \quad (7)$$

We then can compute the cloud’s intensity-weighted mean velocity and velocity dispersion as:

$$v_0^{\text{cloud}} = \frac{\int v T_B^{\text{cloud}}(v) dv}{W_{\text{CO}}^{\text{cloud}}} \quad (8)$$

and,

$$\sigma_v = \sqrt{\frac{\int v^2 T_B^{\text{cloud}}(v) dv}{W_{\text{CO}}^{\text{cloud}}} - v_0^{\text{cloud}}^2} \quad (9)$$

The angular size of a given cloud is straightforward, which is described in unit $arcmin^2$:

$$S_{\text{ang}} = n_{\text{pixels}} \delta l \delta b \quad (10)$$

and angular radius,

$$R_{\text{ang}} = \sqrt{\frac{S_{\text{ang}}}{\pi}} \quad (11)$$

where δl , δb is the grid size of data cube, respectively. Peak intensity of the cloud T_{peak} is the maximum of derived amplitudes:

$$T_{\text{peak}}(^{13}\text{CO}) = \max\{A_1, A_2, \dots, A_j, \dots\} \quad (12)$$

The column density of MCs here can be estimated by the abundance of ^{13}CO emission as well as the $\text{H}_2 - ^{12}\text{CO}$ conversion factor. The first method uses a radiative transfer model under the local thermodynamic equilibrium (LTE) condition, assuming an equal excitation temperature for ^{12}CO and ^{13}CO lines, while the second method gives a direct relation between line intensity and the H_2 column density. For the identified ^{13}CO MC structures, assuming the emission is optically thin, and the temperature of the Cosmic Microwave Background radiation $T_{\text{bg}} \approx 2.7$ K. The summed column density of a given cloud can be described as (Bourke et al. 1997; Wilson et al. 2009):

$$N_{\text{tot}} = C \times 2.42 \times 10^{14} \frac{\tau(^{13}\text{CO})}{1 - e^{-\tau(^{13}\text{CO})}} \times \frac{1 + 0.88T_{\text{ex}}}{1 - e^{-5.29/T_{\text{ex}}}} W_{^{13}\text{CO}}^{\text{cloud}} \quad (13)$$

Here, C is a ratio between the abundance of H_2 and ^{13}CO . We adopt 8×10^5 , from the empirical abundance ratio $[\text{H}_2/^{12}\text{CO}] = 1.1 \times 10^4$ in Frerking et al. (1982) and $^{12}\text{C}/^{13}\text{C}$ relation from Milam et al. (2005). $\tau(^{13}\text{CO})$ is the optical depth at the peak intensity T_{peak} , which is calculated by the excitation temperature T_{ex} . The values of T_{ex} and τ_{13} can be written as (see also Nagahama et al. 1998; Pineda et al. 2010; Li et al. 2018):

$$T_{\text{ex}} = \frac{5.53}{\ln \{1 + 5.53 / [T_{\text{peak}}(^{12}\text{CO}) + 0.819]\}} \quad (14)$$

and,

$$\tau_{13} = -\ln \left\{ 1 - \frac{T_{\text{peak}}}{5.29 [1 / (e^{5.29/T_{\text{ex}}} - 1) - 0.164]} \right\} \quad (15)$$

Finally, the average column density of each ^{13}CO cloud is:

$$N_{\text{mean}} = \frac{N_{\text{tot}}}{n_{\text{pixels}}} \quad (16)$$

4. DISTANCES AND PROPERTIES OF MCS

In the background eliminated extinction-parallax method (i.e., BEEP, Yan et al. 2019a), the unrelated extinction were removed to calculate distances of MCs by calibrating the stellar extinction toward MCs with the extinction of stars around them. The jump point in the A_G -Distance map is detected using Markov Chain Monte Carlo (MCMC) method by a Bayesian modelling approach. There are five key parameters in distance measurement: the location of the jump point (Distance), the extinction value of the foreground and background stars (μ_1 and μ_2), and the dispersion of the foreground and background extinctions (σ_1 and σ_2). A Gaussian distribution is used as the likelihood function of A_G distribution. We set the jump points in 100 to 3000 pc with a uniform distribution, considering the limitation of Gaia's precision. The initial distance is set to the average value of the selected stars. The initial values and errors transformation of other parameters follow Yan et al. (2019b).

We choose *emcee* (Foreman-Mackey et al. 2013), the affine-invariant ensemble sampler for our model, instead of *Pymc3* and Gibbs samplings (Yan et al. 2019b). We also test the difference between *emcee* and *Pymc3* (Salvatier et al. 2016) for MCMC sampling (see details in Appendix B). *emcee* has better performance.

4.1. Selection of star samples

Yan et al. (2019a) showed that the BEEP method is suitable for distance estimations of MCs at low Galactic latitudes. However cloud identification in their procedures could introduce significant uncertainties for clouds in velocity crowding regions, especially in the first quadrant. As discussed in Section 3, the cloud boundary in projection toward Cygnus region can not be well delineated by direct clustering (e.g., Dendrogram, DBSCAN etc.) in PPV space. The identified structures might include emission from other clouds due to the overlap between neighboring structures in PPV space. The extent of both on-cloud and off-cloud stars is thus not well demarcated by the signal levels (Yan et al. 2019a) or identified boundaries (Yan et al. 2021a). As a result, the influence of other structures along the LOS could lead to inaccurate distance measurement with deviation of jump point. We follow the procedures of BEEP, but with a different cloud identification method. Some improvements are made to solve the puzzles in the velocity crowding regions (see details in Section 4.1.2).

4.1.1. Selection of on-cloud stars

After clustering based on Gaussian decomposition (see Section 3.2), we obtain coherent MC structures with exact boundaries from ^{13}CO emission. As seen in the work of Yan et al. (2019b), the number of star samples within the cloud helps to improve the precision of the distance measurements. We thus include all stars inside the cloud boundary (see red and black area in Figure 4).

A further validation of the reliability of the selection is to consider those stars in the overlapping part (black region in Figure 4). We propose that stars in the overlapping area have more contribution to distance measurement than introduced uncertainties. This was also confirmed in a series of test (see Appendix B), where we used all the on-cloud stars and another set of stars with the removal of the overlapping region. We found that most distances show good coincidence between the two scenarios. While the results from selecting all the source stars show smaller errors and more stable sampling.

4.1.2. Selection of field stars

It's also crucial to construct samples of field stars for accurate distance measurement. That is, the selection of suitable field stars can be used for background elimination to highlight the jump caused by the target MC (Yan et al. 2019a). It's difficult to find a clean reference region near the Galactic disk. Generally, to determine the jump point of A_G -Distance map after background elimination, the extinction of field stars should be rather smaller than on-cloud stars, and the displacement from on-cloud stars should be close enough. So that reference stars can be fitted as an extinction background (hereafter “background extinction” means the unrelated extinction toward MCs) for on-source stars and the A_G jump of the cloud structure can reach a threshold to be detected. Obviously, the above two conditions need to be balanced. So we designed models A and B (see Figure 4) to measure the distance of MCs.

Model A. To highlight the jump features in the A_G -Distance map, we use the region of ^{12}CO emission free (^{12}CO integrated intensity $\leq 1 \text{ K} \cdot \text{km} \cdot \text{s}^{-1}$) as the reference region (see orange region in Figure 4a). The outer boundary of reference region (black dashed contour in Figure 4) is limited to within 30 arcmin from the MC. Obviously here we considered the complicated features of MCs in the velocity crowding region based on ^{12}CO and ^{13}CO . This is due to the fact that MCs with multiple velocity components are filled with ^{12}CO emission with which can contribute non-negligible extinction. On the other hand, enough field stars are needed for the accurate distance measurement.

This scheme allows more ^{13}CO MCs to do background elimination in complex regions. After correcting the field stars effects, the distance of the cloud can be clearly identified (see examples in Figure 5a). 185 clouds (see Table 1) out of 300 large-size clouds (angular sizes $\geq 60 \text{ armin}^2$) are measured by Model A.

Model B. Another scheme is more straightforward. We choose a ring-like area outside the ^{13}CO emission as the reference region. An empirical offset helps reveal the jump point. The inner and outer boundaries of the ring-like structure are 2.5 and 7.5 arcmin away from ^{13}CO emission, respectively. We do not exclude field stars located within the ^{12}CO emission in the ring-like area (see Figures 5b and 6b). The number of field stars is then sufficient to capture the extinction characteristics of the background. The distance measurements from Model B are probably more reliable for some special cases (see Appendix D).

Nevertheless, Model B demands that the target MC should have a higher column density than its surroundings. In other words, Model B only works when CO-dark extended gas has small influence on distance measurement. Otherwise, after subtracting background extinction, the jump value is too small to be detected. Generally, the results from Model B may be less accurate than those from Model A (see simulations in Appendix B).

In total, the distances of 120 MC structures from Model B are roughly consistent with those from Model A (see Table 1 and Figure 7). Additionally, another 22 clouds are successfully measured by Model B, which are not measured by Model A.

4.1.3. *On-cloud stars only*

As a comparison, we also measured a group of results without background elimination (see blue squares in Figure 7). To reduce the contamination from different components along the same LOS, we remove the on-source stars in the overlapped region (from ACORNS). Since the background extinction is not subtracted, distance measurements will be affected by other structures (traced by ^{12}CO emission) as well as the accumulated extinction along the LOS. So the obtained distances tend to jump to the position corresponding to the maximal ΔA_G (i.e., $\mu_2 - \mu_1$), or to the average of multiple components. As a result, this scheme gives more distances to the MC samples, but the measurements are not accurate enough for the identified MC structures in Galactic plane (Zucker et al. 2019; Sun et al. 2021a; Guo et al. 2022).

4.2. *Uncertainties*

4.2.1. *Uncertainty from our model*

Two effects have decisive influence on distance measurements of clouds. One comes from the nested clustering algorithm. Considering the complex cloud structures, the criteria settings (see details in Section 3.2) can only extract the physical structure to some extent. On the other hand, a physical structure might be divided into different parts due to velocity gradients, variations of line widths, and nonuniform intensities. This effect can be retrieved by accurate distance measurement for over decomposed complexes in the procedure.

Another effect comes from the complicated extinction of ISM environment. As discussed in Section 3.1, ^{12}CO emission can trace more extended MC structure of the translucent molecular gas than ^{13}CO emission. Even though we have already considered the extinction effect of ^{12}CO gas in the Model A, the atomic gas and CO dark gas is likely more space-filled in the surrounding region. For the ^{13}CO free region, the envelope of the cloud might still contribute to the considerable extinction. We have to carefully deal with the influence from neighboring gas in complicated environment. The separation of different extinction environment cannot be thoroughly removed due to the multi-phase gas structure in the ISM. Therefore, it is much more difficult to choose on-cloud and off-cloud regions traced by ^{13}CO emission in the complicated extinction environment. Nevertheless our methods (Model A and B) should be better than detecting extinction jumps directly by considering the MCs' morphology of ^{13}CO (see Section 3.2) and background elimination (see Section 4.1.2).

How to check whether identified MC structures in the clustering are from a physical cloud? For some large scale structures, we can measure the different sub-regions to explore the possible connection between them. In Appendix A, some sub-regions (boxes or contours in Figures A1 and A2) are chosen to do distance measurements. We find that most of them are in the similar distances (see lower left panel in Figures A1 and A2). Ambiguities from neighboring clouds can't be totally removed, especially for small structures overlapping with adjacent extensive structures.

Besides the 5%~10% system uncertainties within 3 kpc from Gaia data, the sampling process itself also introduces measurement dispersion. As mentioned above, many effects can cause uncertainties of distance measurements, e.g., fewer on-cloud stars, smaller ΔA_G of background eliminated extinction, and multiple jumps along a certain LOS. We first remove clouds with large dispersion of distance caused by lacking of on-cloud stars (≤ 20). Then some clouds have a small difference between both sides of the jump point (i.e., ΔA_G smaller than 0.2 mag). As for detection of multiple jumps, this problem will be further discussed in a future paper. In this paper, combining Model A and B results can largely reduce this problem.

For some large-scale MC structures, their distances are not detected by either Model A or B. It could be due to the severe extinction environment in front of them. The reddening from dust might be more extensive or saturated by Gaia's observation limit for the foreground dark clouds.

In our model, we assume that cloud is a simple screen perpendicular to our sight lines. We thus ignore clouds' thickness and possible inclination to us. Among MCs with measured distance, some display an abnormal feature near the jump point (e.g., the ascending slope in A_G -Distance map). Especially for some large-scale MC structures with a large number of stars (e.g. L889 in the upper-right panel in Figure A2), it might suggest a continuous medium or cloud inclination along the LOS. These effects can cause the deviations of the jumps we determined.

4.2.2. *Uncertainty from baseline elimination*

The statistical distributions of stars in the foreground and/or background of the cloud follow a Gaussian distribution. In some of LOS, we found that the distribution of A_G is Gaussian with an increasing baseline near the jump point. The reddening of stars increases with gentle slope when distance increases. Note that the off-cloud region is not extinction free. We just identify the jump point of this cloud when the jump is much steeper to the off-cloud region.

Based on the monotonically fitting method (Kruskal 1964; de Leeuw 1977) and using a module called scikit-learn in python, we performed the isotonic regression to fit baseline of background extinction weighted by the inverse-variance of A_G (Yan et al. 2019a). Stars with high weights (standard deviations ≤ 0.01 mag) are removed in this work. As the uncertainty of extinction in the G band of Gaia is not a direct measurement, the posterior distribution of A_G with very small values could be unphysical. On the other hand, the high weights of individual sources might introduce deviations of fitting, especially for the monotonically fitting to the off-cloud stars (Yan et al. 2019a). Nevertheless the scarcity of stars and the large dispersion of A_G in the far end causes large bias to our results. We found that $\Delta A_G \geq 0.2$ mag can mitigate the problems.

A_G is derived from A_0 in the Fitzpatrick extinction law (Fitzpatrick 1999) and absolute M_G magnitude from isochrones (Andrae et al. 2023). The median value of uncertainties of A_G and A_0 is around $0.06 \sim 0.07$ mag, considering the inflation effect. Although Gaia collaboration didn't apply corrections for GSP-Phot uncertainties, we use the inflated value for safety, i.e. the lower limit $\Delta A_G = 0.2$ mag (3σ confidence level) for identifying extinction jumps. For Model B, larger A_G values in reference region make smaller ΔA_G after background elimination, we thus set $\Delta A_G = 0.15$ mag (2σ). Considering the fluctuations of A_G from random errors, biases from monotonically increasing fit, and the variations of stars' A_G dispersion with increased distance, larger ΔA_G from MC structures help to reduce false detection.

Figure 7 shows the distance results of ^{13}CO structures (see Section 4.1.2 and 4.1.3). For most of MC samples, the distance measurements match well in Model A and B. We check all the samples and confirm the jump points presented by Model A and B are the same one.

We find 75% of samples from Model A have slightly smaller distance to Model B. We adopt the result from Model A in the following analysis because of more clear jump in Model A (see example in Figure 5). The differences come from sampling process due to different ΔA_G for on-cloud stars after different background elimination (see simulations in Appendix B).

There are two exceptions, G076.74-0.43 (id 30 in Table 1 and Figure 6) and G084.70+0.44 (id 181 in Table 1). For cloud G076.74-0.43, the distance difference from Model A and B is larger than 200 pc. In fact we find two extinction layers toward the direction (see details in Section 5.2). When reference stars are chosen further away from target cloud (e.g., Model A), the measured distance tends to be affected by other structures along LOS. In Figure 6a, after baseline elimination, extinctions of on-cloud stars fluctuate along the A_G -Distance map, indicating the inconsistency of A_G -Distance relation between on-cloud and off-cloud stars. So the baseline subtracted data from Model A might suffer from fluctuations in sampling result. And the distance of the cloud should be 1041_{-68}^{+67} pc from Model B. Similar to cloud G076.74-0.43, the distance difference of G084.70+0.44 from Model A and B is 137 pc, but Model B has a better background elimination, and present smaller sampling uncertainty.

For more special cases with complex background extinction, Model A is invalid because of insufficient field stars in the nearby region. Model B provides distance measurements for another 22 MC structures (see Appendix D). Among these cases, some structures likely suffer from severe contamination from neighboring clouds.

4.3. Molecular cloud parameters

We summarize the parameters of 207 clouds with distance in Table 1. 120 clouds are measured both by Model A and B (class I). Their distances are used in Figure 7 to Figure 16. 22 clouds are only measured by Model B (class II), and over 60 clouds are alone measured by Model A (class III). Generally, the dust-based distances to specific MCs might introduce $\approx 5\%$ uncertainties out to at least 2 kpc from Gaia data (see the recent review from Zucker et al. 2023). In all the following discussions, we added a 5% system uncertainty to the MC distances.

In the left panel of Figure 7, we plot the distance distribution of the 120 class I clouds. There is a gradient from east to west for the molecular gas traced by ^{13}CO emission within 1 kpc. For example clouds near NAP are located at 759 ± 57 pc, while the western clouds near L889 are systematically larger than 800 pc. In Cygnus X South region, we also find a middle gas layer in ~ 1.3 kpc.

Because of the “extinction wall” effect (Straizys et al. 1993), we fail to obtain the distance of some clouds in the Cygnus X star formation region, including DR21, DR20 and the clouds behind L889 (see details in Section 5.1 to

5.2). After removing the foreground clouds, the distance of the rest of clouds can be determined based on the spatial coincidence between the ^{13}CO structures and the corresponding masers/PDR interfaces (see details in Cygnus North Filament from ^{13}CO in Section 5.1 and PDR interfaces traced by intense infrared emission in Section 5.2).

Once the distances of clouds are determined, we can derive the physical parameters of these MCs, such as: effective radius, mass, and surface density.

Physical radius can be calculated from the angular size R_{ang} and cloud distance d :

$$R = d \tan(R_{\text{ang}}) \quad (17)$$

Then, the mass and surface density of ^{13}CO clouds can be estimated by :

$$M = N_{\text{tot}} d^2 \Omega \mu m_{\text{H}} \quad (18)$$

where Ω is the solid angle of each pixel, $\mu = 2.8$ is the atomic weight of molecular hydrogen. And the surface densities of cloud structures is

$$\Sigma_{\text{cloud}} = \frac{M}{\pi R^2} \quad (19)$$

We compute the virial parameter to characterize the dynamical state of clouds or cores, virial mass is in the form:

$$M_{\text{vir}} = 5 \frac{R \sigma_v^2}{G} \quad (20)$$

where G is the gravitational constant, σ_v is the velocity dispersion of each cloud, which is provided in equation (9), assuming the ^{13}CO cloud has a uniform density profile, and the virial parameter can be described as:

$$\alpha_{\text{vir}} = \frac{5 \sigma_v^2 R}{GM} \quad (21)$$

The cloud distance perpendicular to Galactic disk is directly described by:

$$z = d \sin(b_0) \quad (22)$$

5. SUB-REGIONS TOWARD CYGNUS

5.1. *Cyg-North region*

Based on the measured distances of MCs, we find at least two layers of gas emission in the foreground toward the Cygnus X North region (see Figures 8, 9, 10). One is at ~ 800 pc and another at ~ 1 kpc. Combining the other information (see below), many ^{13}CO structures are located in more distant regions.

800 pc gas layer. The velocities of molecular gas in this layer are mainly concentrated in $1 \text{ km} \cdot \text{s}^{-1}$ to $7 \text{ km} \cdot \text{s}^{-1}$ (see contours in Figure 8b and orange dots in Figure 9), including the filament L914 (see Section 5.4 and Figure 15). In the region of $l=[82, 84]$ deg and $b=[1.5, 2.5]$ deg, some MCs are at higher velocities intervals ($8 \leq v \leq 13 \text{ km} \cdot \text{s}^{-1}$). Including those NAP clouds in the velocity interval of $[-6, 6] \text{ km} \cdot \text{s}^{-1}$ (Section 5.3), we find that a large molecular gas loop is located at ~ 800 pc (see below in Figures 8 and 17).

1 kpc gas layer. In Figure 8abc, we find a gas layer at ~ 1 kpc. MCs in this layer have a large velocity extent from -4 to $14 \text{ km} \cdot \text{s}^{-1}$ (black dots in Figure 9), inferring large velocity dispersion between clouds. We identify them as a MC complex from $(l=81, b=0.8)$ deg to $(l=79, b=-1.8)$ deg. We note that a “twins cluster” structures are located in this layer (marked as cluster a and b in Figure 9 and Figure 10b, also see id 123 and 113 in Table 1). The two clusters’ distances are 962_{-67}^{+64} pc and 1024_{-73}^{+77} pc, respectively. We note that the two structures have almost the same physical properties but very different velocities. Both of them also have higher bright temperature than other clouds in the 800 pc and 1 kpc gas layer. What causes the twin clouds’ velocity to differ by $15 \text{ km} \cdot \text{s}^{-1}$ is still unknown. Further studies would be interesting to find out the kinematic origin of them.

Background layer for more distant gas at ~ 1.5 kpc. The distances of many MC structures with intense ^{13}CO emission are failed to be determined because of the large extinction from the above two layers. We attribute these filamentary structures with fluctuated velocities from $-9 \text{ km} \cdot \text{s}^{-1}$ to $1 \text{ km} \cdot \text{s}^{-1}$ (see Figure 8a) as the Cygnus North Filament. The Cygnus North Filament is very prominent in the north of Cygnus OB2. DR21(OH), DR21, DR23, DR22 are all located along the dense CO filament. The filament can be divided into different substructures

in clustering result due to velocity gradient (see Figure 8d). DR21 and DR21(OH) at $\sim 3 \text{ km} \cdot \text{s}^{-1}$ are on the most bright DR21 filament (see the intensive C¹⁸O emission in grey scale of Figure 8a). The distance of the Cygnus North Filament is estimated to be 1.5 kpc by methanol maser measurement from DR21 and DR20 (Rygl et al. 2012). We also find that some dense molecular gas with slightly high velocities are different from MCs at 800 and 1 kpc layers. For example the MC associated with W 75N (see m11 in Table 2) is overlapped with DR21 filament, but at a nearer distance of 1.3 kpc (Rygl et al. 2012).

Furthermore we also find several corresponding structures between ¹³CO emission and bright infrared features (see Figure 8e). Among them the two globules (see Schneider et al. 2006, 2016) and DR17 with large velocities (from $7 \text{ km} \cdot \text{s}^{-1}$ to $20 \text{ km} \cdot \text{s}^{-1}$) are probably associated with nearby star-forming regions (e.g., Cygnus OB2). We assume these MCs, together with clouds on the Cygnus North Filament, range from 1.3 kpc to 1.7 kpc based on the association between MCs and masers or OB stars. (Rygl et al. 2012; Quintana & Wright 2021). Tentatively we put them together as a background layer with an averaged distance at $\sim 1.5 \text{ kpc}$.

In Figure 9 we plot the ¹³CO bright temperature, velocity dispersion and column density of MCs in different gas layers. The bright temperature and column density of the molecular gas at $\sim 1.5 \text{ kpc}$ are obviously larger than the gas in 800 pc and 1 kpc gas layers.

The 3D illustration in Figure 10 denotes the distribution of three layers toward the Cygnus X North region. Again, the extended molecular gas in the 800 pc and 1 kpc layers is overlapped in front of the $\sim 1.5 \text{ kpc}$ MCs, leading to the failure of distance measurements of these MCs at larger distances based on our models.

5.2. Cyg-South region

The molecular gas in $\sim 4 \times 4 \text{ deg}$ region of Cygnus X South is divided into three velocity intervals: the mid-interval ($-3 \sim 3 \text{ km} \cdot \text{s}^{-1}$), minus interval ($-10 \sim -3 \text{ km} \cdot \text{s}^{-1}$), and positive interval ($3 \sim 12 \text{ km} \cdot \text{s}^{-1}$) based on our clouds identification. These results can be compared with the work from Schneider et al. (2006). We also identified at least three gas layers toward the direction.

950 pc gas layer. In Figure 11a, we found that a bulk of molecular gas are at a distance of $\sim 950 \text{ pc}$ (e.g. the prominent emission from giant molecular complex L889). The mean bright temperature of the clouds in this layer is low, which is different from the gas associated with the star-forming regions (see the background layer below). From Figure 11 and Figure 12, most of clouds the in Cygnus X South region are near $0 \text{ km} \cdot \text{s}^{-1}$, which causes great difficulty to distinguish them. The clouds in $\sim 950 \text{ pc}$ layer are distributed in all velocity intervals. Figure 11f shows agreement between our result and the 3D dust maps by Green et al. (2019). As the largest ¹³CO structure in Table 1 (id 57 for L889), we will further discuss it in Appendix A.

1.3 kpc gas layer. We also identify a group of clouds with larger distances, which construct a layer of molecular gas at $\sim 1.3 \text{ kpc}$ toward the Cygnus X South. The velocities of these clouds are distributed in $[-12, 12] \text{ km} \cdot \text{s}^{-1}$. The spatial distribution of these 1.3 kpc clouds with smaller sizes are relatively discrete from those in the 950 pc gas layer. Because of great extinction caused by the 950 pc layer, the clouds with measured distances in the 1.3 kpc layer are mainly found in the region with weak CO emission from L889 structure (see Figure 11ac).

Interestingly, we find a cloud (see cloud 94 in Table 1) is located at $1271_{-115}^{+116} \text{ pc}$, which agrees well with the maser G079.73+0.99 at 1.36 kpc (Rygl et al. 2012). Another cloud associated with HII region DR7 (see cloud 86 in Table 1) is at $1247_{-100}^{+113} \text{ pc}$ based on our models.

For the DR13 cloud (see cloud 48 in Table 1) with bright CO and infrared emission, its distance by Model B is also at $\sim 1.3 \text{ kpc}$. Next to DR13, the cloud G077.9-1.1 with bright CO emission (see cloud 44 in Table 1) matches the IR dark area very well (see Figure 11 a and e). Our distance measurement confirms it's at $1215_{-87}^{+90} \text{ pc}$. We suppose that cloud G077.9-1.1 is slightly in front of DR13 cloud, leading to the matched morphology between the molecular gas structure and IR dark area. These results demonstrate the accuracy and effectiveness of our methods.

Background layer for more distant gas associated with PDR interfaces. For clouds further away than $\gtrsim 1.4 \text{ kpc}$ toward the Cygnus X South region, only two MCs can be determined by Model B (id 19 and 67 in Table 1). However at least tens of dense CO clouds with cometary, oval-shaped and irregular structures coincide well with bright $8\mu\text{m}$ emission. We also find good agreement in physical properties of these clouds (e.g., ¹³CO peak temperature and column density, see blue dots in Figure 12).

We note that the cometary clouds (see Table 3) show head-to-tail morphology pointing away from the Cygnus OB2, indicating the interaction between the molecular gas and intense UV radiation or stellar wind from nearby OB stars. These results are similar to Schneider et al. (2007). One of those cometary clouds (see m7 in Table 2 and p11 in Table

3, also named globules in Schneider et al. 2006, 2016) is exactly located at 1.61 kpc based on maser measurement of G079.87+01.17 (see IRAS 20286+4105 in Xu et al. 2013). The coincidence of molecular gas and IRAS 20286+4105 demonstrates the above picture.

For these cometary clouds, clouds A and B identified by Schneider et al. (2006) correspond to our cases p1 and p3 (see Table 3). From our clouds identification, we find another cloud C (p5 in Table 3) is next to cloud B (see Figure 11 a and e). The high temperatures of the three clouds in the Cygnus X South region, as well as the high column densities, are different from clouds in 950 pc and 1.3 kpc gas layers (see Figure 12). We suggest that all of them are probably shaped by nearby Cygnus OB2 and subgroups of OB1 associations.

Besides the cometary clouds, the spatial morphology of some oval-shaped clouds also coincide with the structure of HII regions (e.g. DR 6, DR 9 identified by Downes & Rinehart 1966), indicating the physical association between them. For these oval-shaped clouds, we don't have enough evidences to associate them with large scale radiation field, thus their distances cannot be confirmed. Here we temporarily put the oval-shaped and irregular MCs in the background layer (see hollow circles in Figure 12).

We conclude that L889 and the nearby clouds in 950 pc layer contain majority of molecular gas with low peak temperature and column density. Toward the Cygnus X South region, parts of MCs in the 1.3 kpc layer are associated with the nearer HII regions and star-forming regions (e.g., DR 13). We propose MCs associated with W75 N in the Cygnus X North also belong to the 1.3 kpc layer. Clouds embedded in the Cygnus X South star formation region are mainly in a narrow velocity interval $\lesssim 3 \text{ km} \cdot \text{s}^{-1}$, mixing up with 950 pc and 1.3 kpc gas layers. It is different from velocity distributions in the Cygnus X North region (see Figure 9). These clouds with high column densities and temperatures are being affected by stellar feedbacks from massive OB associations.

5.3. North America/Pelican (NAP) region

Our identified clouds in NAP have multiple velocity components from $-6 \text{ km} \cdot \text{s}^{-1}$ to $6 \text{ km} \cdot \text{s}^{-1}$ (see Figure 13b), which is also shown by Kuhn et al. (2020) using the moment1 map from FCRAO ^{13}CO . We also present C^{18}O emission in this area (grey scale in Figure 13a).

In Figure 14a, we plot the measured distances of different trees from ACORNS of the NAP (see clouds id 169 \sim 195 in Table 1). We find that the MC complex is located at about 759 ± 57 pc, which is roughly consistent with previous studies based on Gaia EDR3 YSO samples in the NAP region (~ 785 pc in Kuhn & Hillenbrand 2020). The group E ($l \sim 84.8$, $b \sim -1.2$) identified by Kuhn et al. (2020) has a distance of ~ 746 pc, which is slightly smaller than their average distance of ~ 785 pc for the complex. We note that at least three cloud structures (id 173, 190 and 193 in Table 1) are located at ~ 740 pc toward the Group E. Figure 14b presents a system deviation of distance measurements between our results and Zucker et al. (2020). We propose that the differences come from the upgrade of both A_G and parallaxes from DR2 to DR3 (systematic uncertainty), and different details between two models: (1) on-cloud stars selection based on different cloud decomposition to the stratified gas structure, and (2) model with vs. without background elimination. Moreover, A_G uncertainty is likely to be different along different LOS. For example, our distance measurements toward the Cygnus X region have no prominent systematic deviation with those of Zucker et al. (2020). We suggest that the NAP complex in the “800 pc gas layer” (see Section 5.1) is part of the Cygnus Rift.

5.4. L914 filament

L914 (see clouds id 139 and 161 in Table 1) is a filamentary dark cloud connecting the NAP region and the Cygnus X North region. The filament with a large velocity gradient along the spine has rather small intrinsic velocity dispersion (see Figure 15b). Bright C^{18}O emission also presents a filamentary structure from right to left (hereafter head to tail). We find that the main structure (head, id 139 in Table 1) has a distance of 787_{-44}^{+45} pc. Obviously, L914 and NAP clouds belong to the 800 pc gas layer of the Cygnus X North region. We also note that the substructure in the tail of L914 (id 161 in Table 1) is located at a smaller distance of 723_{-47}^{+51} pc. Considering the spatially continuous distribution of the molecular gas (especially for the coherent filamentary structure traced by C^{18}O in Figure 15a), we propose that they belong to a single structure at ~ 770 pc. There are also some interesting striations (Goldsmith et al. 2008) perpendicular to the spine of L914 (see details in Sun et al. accepted by AAS, 2024).

5.5. S106

S106 is a well known HII region in the Cygnus X South. The dense cloud G076.33-0.74 (see contours in Figure 16, hereafter S106 cloud) is considered to be shaped by nearby OB associations (e.g., see NGC 6913 discussed by Schneider

et al. 2007). Besides, the new results show that the OB stars of Group C identified by Quintana & Wright (2021) could be the source shaping S106 cloud.

Although distance measurement to the S106 cloud is failed for both of Model A and B, we suspect the cloud is located at least 1 kpc away. The 800 pc gas layer (see id 28 in Table 1) extends to the S106 region, that could be why previous measurement to S106 have a closer distance (e.g., 600 pc in Staude et al. 1982). Actually, one nearby cloud (see cloud id 30 in Table 1, see Section 5.2) in the 950 pc gas layer is also overlapped with the S106 cloud. The heavy extinction effect of these clouds leads to the failure of distance measurement for the cloud.

The maser G076.38-0.61 (see m3 in Table 2) is located in S106 region at 1.3 kpc (Xu et al. 2013), suggesting molecular gas at 1.3 kpc layer in this direction. In addition to the S106 cloud, we also identify another cloud structure G076.39-0.66 (see red dots in Figure 16) is superposed with the maser. This structure (see m3 in Table 2) is presented as another velocity component which spatially coincides with the maser G076.38-0.61. Similar to the S106 cloud, MC G076.39-0.66 has high peak temperature and intense ^{13}CO emission. Both structures could be the HMSFR where the maser located in, indicating the S106 cloud probably at the 1.3 kpc gas layer. However, the cometary morphology traced by ^{13}CO and infrared emission for the S106 cloud might be shaped by the nearby OB associations. Thus other opinions suggest the distance to S106 cloud is at ~ 1.7 kpc (Quintana & Wright 2021), while the maser G076.38-0.61 might be associated with G076.39-0.66 at 1.3 kpc.

Interestingly, we find that a cloud G075.79+0.42 (see cloud id 24 in Table 1) is adjacent to the S106 cloud in projection. The cloud is at ~ 800 pc from Model A. In addition, another component at 1.7 kpc can be discerned in a new mulit-jump model (in preparation), indicating the possible gas layer in there. It shows that toward the region, there are complicated gas distribution at different distances. We will study the multi-jump features of molecular gas in a forthcoming paper. In Table 2, we temporarily associate maser G076.38-0.61 with MC G076.39-0.66 (m3 in Table 2).

5.6. Other interesting regions

Cygnus-NW: The dark cloud complex L897 is located in the Cygnus North-West (Cygnus-NW, see Figure 1). Clouds associated with it have velocities ranging from ~ 5 to $10 \text{ km} \cdot \text{s}^{-1}$. Four of them (id 97, 99, 102 and 104 in Table 1) have been measured at a uniform distance of ~ 1 kpc, reflecting the 1 kpc gas layer therein. We also note two structures (id 99 and 104 in Table 1) have very small virial parameter ($\lesssim 1$). Combined with the good agreement with the overdensity of YSOs toward the Cygnus-NW clouds within 1 kpc (see Appendix F), we infer that these MCs are gravity bounded and that the dark cloud is physically associated with the ongoing star-forming region.

Cygnus OB3 and OB8: Cygnus OB3 and OB8 are located at ~ 1895 pc and ~ 1726 pc, respectively (Quintana & Wright 2021).

Toward the Cygnus OB3, we identified a massive ^{13}CO cloud (id 1 in Table 1) at ~ 1.8 kpc, which agrees with the median distance of the OB association. And several small clouds (see id 3 and 5 in Table 1) toward the direction are at ~ 1 kpc.

Toward the Cygnus OB8, we find an interesting ^{13}CO cloud G078.12+3.63 that is associated with a maser G078.12+03.63 at a distance of ~ 1.55 kpc (Reid et al. 2019). The Median distance of Cygnus OB8 from EDR3 (Quintana & Wright 2021) is a bit further than the maser's distance. However, considering the distance uncertainty, they are probably at the same place. Based on our models, another two MCs (id 33 and 35 in Table 1) are located in ~ 1.2 kpc in this direction, indicating that the extended 1.3 kpc gas layer extends in front of the OB8 association (see Figure 17).

Other clouds associated with masers: Two masers G74.03-1.71 and G80.80-1.92 (see m1 and m8 in Table 2) are located at about 1.6 kpc (Xu et al. 2013; Zhang et al. 2012). We find two MCs (i.e., cloud id 16 and 116 in Table 1) are probably at ~ 1.3 kpc and ~ 1 kpc, respectively, based on Model A. However, due to lacking convincing distance measurement from Model B, we suspect that the foreground molecular gas at 1-1.3 kpc is likely overlapped to the masers' cloud. This effect leads to that we just detect the nearer distance of the foreground gas. According to the mulit-jump model (in preparation), jump features in the A_G -Distance map can be discerned at ~ 1.51 kpc and 1.73 kpc, respectively.

We identify that a MC (see m5 in Table 2) with a LSR velocity of $-5 \text{ km} \cdot \text{s}^{-1}$ is associated with AFGL2591 at a distance of 3.3 kpc (Rygl et al. 2011). We find that the m5 cloud is overlapped with L889 filament (see Figure 11d). The cloud has high bright temperature and large line widths, indicating the massive star formation within it. Another small cloud (see m2 in Table 2) with medium bright temperature and column density is associated with 2.7 kpc maser

toward the direction of Cygnus OB1. Finally, for two masers more than 3 kpc G075.76+0.33 ([Xu et al. 2013](#)) and G075.78+0.34 ([Ando et al. 2011](#)), we find that intense CO emission at \sim 800 pc just locate in front of the two masers. As a result we are unable to identify the MCs associated with them.

The difficulty increases when looking for more distant CO emission in our FOV. For more distant clouds, smaller angular sizes, together with large extinction and parallax uncertainty of stars from Gaia DR3, limit us to determine their distances. These more distant clouds also suffer from extinction of foreground layers (i.e. the 800 pc, 1 kpc, and 1.3 kpc gas layer) identified in this paper.

We measured at least seven clouds (class I and II) with distances larger than 1.4 kpc. All of them are in large radius (i.e., at least larger than 5 arcmin based on ^{13}CO emission). Most of them are located in relatively high latitude regions and/or simple extinction environments, leading to less contamination of foreground emission. The above two facts enable us to determine their distances after background elimination.

Table 1. Parameters of 207 MC structures with distance measurement

(1)	(2)	(3))	(4)	(5)	(6)	(7)	(8)	(9)	(10)	(11)	(12)	(13)
id	l	b	v_{LSR}	σ_v	R	d^A	d^B	N_{mean}	$Mass^{\text{LTE}}$	$Mass^{\text{Xfactor}}$	α	Adopted model
	deg	deg	$\text{km} \cdot \text{s}^{-1}$	$\text{km} \cdot \text{s}^{-1}$	pc	pc	pc	cm^{-2}	m_{\odot}	m_{\odot}		
1	72.29	2.31	-2.2	1.2	5.2	$1784^{+27}_{-20} \pm 89$	$1745^{+20}_{-26} \pm 87$	$5.98e+21$	10920	12470	0.8	A
2	72.43	0.38	4.1	1.4	4.1	$2478^{+76}_{-42} \pm 123$	$964^{+22}_{-22} \pm 48$	$1.50e+21$	1740	3000	5.5	A
3	72.62	0.76	5.6	0.7	1.5	$959^{+18}_{-19} \pm 47$	$1001^{+37}_{-33} \pm 50$	$7.21e+20$	110	210	8.3	A
4	72.68	-0.74	5.0	1.2	2.5	$1072^{+28}_{-28} \pm 53$	$1095^{+24}_{-34} \pm 54$	$1.39e+21$	570	870	6.9	A
5	73.23	0.58	5.4	0.6	1.4	$1001^{+37}_{-33} \pm 50$	$994^{+39}_{-36} \pm 49$	$1.03e+21$	140	240	3.9	A
6	73.23	-0.69	7.1	0.9	1.9	$1671^{+32}_{-31} \pm 83$	$1052^{+36}_{-35} \pm 52$	$1.68e+21$	400	360	4.1	A
7	73.31	-0.06	3.1	1.2	6.5	$1060^{+22}_{-20} \pm 53$	$1038^{+25}_{-26} \pm 51$	$2.39e+21$	6750	10240	1.5	A
8	73.44	-0.69	3.7	1.3	2.5	$1909^{+74}_{-63} \pm 95$	$1872^{+50}_{-74} \pm 93$	$1.67e+21$	710	940	6.4	A
9	73.99	3.56	-4.5	1.2	3.6	$1060^{+22}_{-20} \pm 55$	$1038^{+25}_{-26} \pm 51$	$4.62e+21$	3930	4610	1.6	A
10	74.08	0.38	1.9	1.7	4.4	$1108^{+22}_{-20} \pm 55$	$1038^{+25}_{-26} \pm 51$	$2.70e+21$	3460	5350	4.2	A
11	74.09	-0.50	6.2	0.9	2.1	$1000^{+33}_{-41} \pm 50$	$899^{+35}_{-27} \pm 44$	$1.91e+21$	570	790	3.6	A
12	74.18	-4.79	10.1	1.0	1.6	$959^{+22}_{-23} \pm 47$	$969^{+24}_{-24} \pm 48$	$8.91e+20$	160	240	12.5	A
13	74.31	0.16	2.3	1.3	2.8	$1014^{+36}_{-34} \pm 50$	$1258^{+42}_{-57} \pm 62$	$2.60e+21$	1390	2180	4.3	A
14	74.35	-2.47	3.1	1.2	1.7	$908^{+20}_{-20} \pm 45$	$798^{+31}_{-33} \pm 39$	$2.33e+21$	430	820	6.9	B
15	74.88	-4.67	11.9	0.5	1.8	$1329^{+46}_{-51} \pm 66$	$784^{+26}_{-35} \pm 39$	$1.01e+21$	220	290	2.8	A
16	74.94	-2.35	4.0	0.9	2.0	$947^{+72}_{-52} \pm 47$	$1482^{+90}_{-61} \pm 74$	$1.27e+21$	340	690	5.4	A
17	75.06	0.06	6.8	0.7	1.2	$831^{+11}_{-10} \pm 41$	$774^{+24}_{-42} \pm 38$	$1.03e+21$	100	140	6.0	B
18	75.13	0.07	0.4	1.7	1.9	$816^{+35}_{-39} \pm 40$	$765^{+36}_{-44} \pm 38$	$3.20e+21$	770	1390	8.5	A
19	75.21	-2.11	-4.2	0.8	2.2	$857^{+36}_{-41} \pm 42$	$864^{+34}_{-35} \pm 43$	$6.54e+21$	600	930	2.9	B
20	75.28	-0.13	4.1	1.4	2.0	$1502^{+84}_{-71} \pm 75$	$809^{+19}_{-22} \pm 40$	$1.58e+21$	450	1110	10.9	A
21	75.48	-0.12	0.3	1.6	2.3	$1141^{+38}_{-42} \pm 57$	$777^{+27}_{-37} \pm 38$	$1.73e+21$	610	1860	10.5	A
22	75.67	0.02	3.9	1.6	1.8	$816^{+35}_{-39} \pm 40$	$987^{+61}_{-51} \pm 49$	$1.64e+21$	360	860	14.9	A
23	75.71	0.30	-0.8	2.1	2.0	$793^{+16}_{-18} \pm 39$	$843^{+16}_{-22} \pm 42$	$4.54e+21$	1820	2440	5.7	A
24	75.79	0.42	2.0	1.7	2.0	$831^{+11}_{-10} \pm 41$	$1041^{+15}_{-16} \pm 52$	$4.98e+21$	1330	1660	5.1	A
25	75.81	0.18	-2.4	1.7	2.0	$832^{+10}_{-10} \pm 42$	$1041^{+15}_{-16} \pm 52$	$3.59e+21$	980	1700	7.2	A
26	75.99	0.13	1.4	3.1	1.1	$816^{+35}_{-39} \pm 40$	$809^{+34}_{-33} \pm 44$	$4.65e+21$	390	740	31.7	A
27	76.09	0.73	5.6	0.9	1.7	$880^{+34}_{-33} \pm 44$	$843^{+16}_{-22} \pm 42$	$3.87e+21$	790	900	2.0	A
28	76.15	-0.09	-0.8	1.6	2.5	$864^{+36}_{-37} \pm 40$	$1041^{+15}_{-16} \pm 52$	$4.14e+21$	1800	2580	4.2	A
29	76.21	0.16	0.5	1.5	3.4	$832^{+10}_{-10} \pm 41$	$947^{+18}_{-22} \pm 47$	$3.25e+21$	2520	3660	3.4	A
30	76.74	-0.43	-3.8	1.6	4.4	$1742^{+44}_{-44} \pm 87$	$1040^{+44}_{-61} \pm 52$	$5.54e+21$	3110	6470	4.1	B
31	76.94	2.22	1.4	1.1	4.4	$1040^{+44}_{-61} \pm 52$	$944^{+35}_{-36} \pm 47$	$1.95e+21$	270	8620	0.8	A
32	76.96	0.20	-0.1	1.2	1.4	$1040^{+44}_{-61} \pm 52$	$944^{+35}_{-36} \pm 47$	$1.95e+21$	270	550	8.2	A

Table 1 continued on next page

Table 1 (*continued*)

(1)	(2)	(3))	(4)	(5)	(6)	(7)	(8)	(9)	(10)	(11)	(12)	(13)
id	<i>l</i>	<i>b</i>	<i>v</i> _{LSR}	σ_v	R	<i>d</i> ^B	<i>d</i> ^A	<i>N</i> _{mean}	<i>Mass</i> _{LTE}	<i>Mass</i> _{Xfactor}	α	Adopted model
deg	deg	km · s ⁻¹	km · s ⁻¹	km · s ⁻¹	pc	pc	pc	cm ⁻²	<i>m</i> _⊙	<i>m</i> _⊙		
33	77.11	3.63	-12.9	1.0	2.5	1216 ⁺³⁵ ₋₃₂ ± 60	1239 ⁺⁶⁸ ₋₄₁ ± 61	2.28e+21	970	1290	3.0	A
34	77.11	0.08	9.2	1.5	1.7	948 ⁺³³ ₋₅₇ ± 47	2.41e+21	490	920	9.5	B	
35	77.22	3.29	15.1	0.8	1.9	1179 ⁺²⁸ ₋₂₂ ± 58	1166 ⁺²⁸ ₋₂₈ ± 58	2.22e+21	560	640	2.8	A
36	77.40	0.90	-0.8	2.1	2.4	935 ⁺²³ ₋₂₀ ± 46	935 ⁺²³ ₋₂₀ ± 46	3.18e+21	1270	3000	9.5	A
37	77.43	2.18	14.3	0.8	1.7	1154 ⁺⁵⁴ ₋₅₁ ± 57	1069 ⁺⁴² ₋₆₃ ± 53	1.92e+21	390	480	3.3	A
38	77.47	1.85	1.4	1.4	2.8	1022 ⁺²² ₋₂₃ ± 51	1.04e+22	5360	4850	1.2	A	
39	77.48	0.58	6.4	2.1	1.8	969 ⁺²⁹ ₋₂₅ ± 48	894 ⁺⁴⁵ ₋₃₁ ± 44	2.14e+21	460	980	19.2	A
40	77.66	0.65	7.5	1.9	2.2	909 ⁺⁴⁸ ₋₃₄ ± 45	909 ⁺⁴⁸ ₋₃₄ ± 45	2.55e+21	860	1570	10.8	A
41	77.66	2.55	1.6	0.9	1.8	1176 ⁺¹¹⁵ ₋₇₉ ± 58	1176 ⁺¹¹⁵ ₋₇₉ ± 58	1.78e+21	400	660	4.4	A
42	77.68	0.99	1.7	1.1	3.1	979 ⁺¹⁴ ₋₂₀ ± 48	979 ⁺¹⁴ ₋₂₀ ± 48	2.81e+21	1870	3050	2.3	A
43	77.78	1.66	1.4	1.4	1.3	956 ⁺³⁶ ₋₃₂ ± 47	929 ⁺³⁵ ₋₃₆ ± 46	2.70e+21	300	570	9.3	A
44	77.89	-1.10	-1.7	1.6	3.1	1215 ⁺²⁹ ₋₂₆ ± 60	1207 ⁺²² ₋₂₄ ± 60	6.21e+21	4060	5860	2.3	A
45	77.98	1.77	-1.9	1.0	2.0	1003 ⁺²¹ ₋₂₆ ± 50	1003 ⁺²¹ ₋₂₆ ± 50	8.15e+21	2190	2050	1.0	A
46	78.03	-1.00	0.5	2.0	6.8	1261 ⁺²³ ₋₂₁ ± 63	1326 ⁺⁶⁵ ₋₅₆ ± 66	7.27e+21	22460	31330	1.4	A
47	78.05	-0.25	15.1	0.7	1.8	1320 ⁺¹¹⁶ ₋₉₁ ± 66	1320 ⁺¹¹⁶ ₋₉₁ ± 66	2.15e+21	460	660	2.4	B
48	78.16	-0.31	-0.5	2.1	2.1	1215 ⁺²⁹ ₋₂₆ ± 60	1217 ⁺⁵⁰ ₋₅₀ ± 60	6.40e+21	1870	2800	5.5	B
49	78.17	-1.42	0.2	2.6	7.4	1238 ⁺¹³ ₋₁₃ ± 61	1238 ⁺¹³ ₋₂₁ ± 63	6.07e+21	22100	33890	2.6	A
50	78.20	2.15	13.4	0.5	2.4	1064 ⁺²⁶ ₋₂₀ ± 53	939 ⁺³¹ ₋₄₂ ± 46	2.31e+21	910	920	0.6	A
51	78.24	0.23	14.1	1.0	1.7	1200 ⁺⁴⁷ ₋₃₇ ± 60	1200 ⁺⁴⁷ ₋₃₇ ± 60	1.92e+21	370	780	5.1	B
52	78.32	-0.63	10.2	1.6	1.8	1217 ⁺⁵⁰ ₋₅₀ ± 60	1217 ⁺⁵⁰ ₋₅₀ ± 60	2.42e+21	540	1130	10.0	B
53	78.33	1.74	1.7	1.3	1.6	1002 ⁺⁷⁴ ₋₇₄ ± 50	1002 ⁺⁷⁴ ₋₇₄ ± 50	2.11e+21	350	610	8.9	A
54	78.40	0.19	9.3	1.2	3.9	1.296 ⁺⁶⁷ ₋₅₇ ± 64	1043 ⁺⁵⁵ ₋₄₆ ± 52	3.82e+21	3950	5310	1.7	B
55	78.44	3.57	14.4	0.7	1.7	870 ⁺²¹ ₋₂₂ ± 43	846 ⁺¹⁵ ₋₁₈ ± 42	1.17e+21	230	430	4.5	A
56	78.48	2.24	-3.0	0.9	2.5	935 ⁺⁴ ₋₃ ± 46	911 ⁺⁵ ₋₅ ± 45	1.38e+21	590	1050	3.8	A
57	78.50	0.39	-0.0	2.4	14.1	967 ⁺¹⁰ ₋₁₀ ± 48	940 ⁺¹¹ ₋₁₃ ± 47	3.71e+21	49490	68310	1.9	A
58	78.50	-0.25	-4.8	1.2	1.7	893 ⁺²⁷ ₋₁₈ ± 44	871 ⁺²⁷ ₋₂₈ ± 43	1.87e+21	370	720	7.4	B
59	78.54	-1.61	1.6	1.6	3.3	904 ⁺²⁷ ₋₂₀ ± 45	864 ⁺²² ₋₃₂ ± 43	2.53e+21	1870	3040	5.6	A
60	78.57	2.47	10.2	1.1	1.8	1161 ⁺⁵³ ₋₇₅ ± 58	1197 ⁺⁷³ ₋₈₇ ± 64	2.81e+21	620	1060	3.9	A
61	78.58	0.99	-7.6	1.6	1.6	919 ⁺²² ₋₂₂ ± 45	921 ⁺²³ ₋₂₆ ± 46	2.99e+21	530	1100	9.5	A
62	78.66	2.70	9.0	0.8	1.2	830 ⁺³⁰ ₋₄₉ ± 41	759 ⁺⁴⁶ ₋₇₃ ± 37	1.91e+21	170	330	5.5	A
63	78.74	2.72	2.6	0.8	1.7	893 ⁺²⁷ ₋₁₈ ± 44	871 ⁺²⁷ ₋₂₈ ± 43	3.78e+21	740	850	1.7	A
64	78.75	2.70	12.7	0.9	2.3	1257 ⁺³⁵ ₋₃₅ ± 62	1243 ⁺⁴² ₋₄₂ ± 62	2.77e+21	930	1270	2.6	A
65	78.75	1.58	10.9	0.7	2.2	1146 ⁺⁵⁸ ₋₅₇ ± 57	1146 ⁺⁵⁸ ₋₅₇ ± 57	2.30e+21	550	1050	1.3	A
66	78.83	1.74	9.3	0.7	1.9				680	680	1.8	B

Table 1 *continued on next page*

Table 1 (*continued*)

(1)	(2)	(3))	(4)	(5)	(6)	(7)	(8)	(9)	(10)	(11)	(12)	(13)
id	<i>l</i>	<i>b</i>	v_{LSR}	σ_v	R	d^B	d^A	N_{mean}	$Mass^{\text{LTE}}$	$Mass \times \text{factor}$	α	Adopted model
deg	deg	km · s ⁻¹	km · s ⁻¹	km · s ⁻¹	pc	pc	pc	cm ⁻²	m_{\odot}	m_{\odot}		
67	78.89	-0.22	-0.5	1.5	2.6	939 ⁺²⁹ ₋₂₁ ± 46	1493 ⁺¹²⁷ ₋₁₁₀ ± 74	4.34e+21	1920	3320	3.3	B
68	78.91	2.69	12.8	0.5	1.5	931 ⁺⁸ ₋₇ ± 46	828 ⁺⁴³ ₋₆₁ ± 41	1.43e+21	210	310	2.0	A
69	78.93	-1.52	1.1	1.5	5.0	905 ⁺⁴⁵ ₋₄₁ ± 45	920 ⁺¹⁰ ₋₁₀ ± 46	2.07e+21	3460	5620	3.9	A
70	78.96	2.76	7.1	1.0	1.6	931 ⁺⁴⁴ ₋₄₅ ± 46	931 ⁺⁴⁴ ₋₄₅ ± 46	4.23e+21	690	780	2.7	A
71	78.97	0.33	3.5	0.9	1.4	762 ⁺²³ ₋₂₁ ± 38	762 ⁺²³ ₋₂₁ ± 38	1.82e+21	230	350	5.2	B
72	79.03	0.22	2.4	1.4	1.4	793 ⁺³¹ ₋₂₂ ± 39	2.51e+21	2.51e+21	310	540	9.4	B
73	79.05	-0.20	1.2	1.4	4.2	903 ⁺¹⁶ ₋₁₉ ± 45	903 ⁺¹⁶ ₋₁₉ ± 45	2.15e+21	2560	4680	3.8	A
74	79.12	2.30	10.2	1.1	3.5	983 ⁺¹³ ₋₁₆ ± 49	976 ⁺¹¹ ₋₁₃ ± 48	2.37e+21	1890	2930	2.5	A
75	79.13	0.39	10.1	1.8	3.9	944 ⁺²² ₋₂₂ ± 47	944 ⁺²² ₋₂₂ ± 47	3.86e+21	3980	7520	3.6	A
76	79.20	0.61	-1.2	1.2	1.4	883 ⁺³⁷ ₋₃₇ ± 44	883 ⁺³⁷ ₋₃₇ ± 44	2.84e+21	400	610	6.5	B
77	79.21	1.25	5.3	1.8	2.8	1034 ⁺³⁹ ₋₆₆ ± 51	1034 ⁺³⁹ ₋₆₆ ± 51	5.24e+21	2720	3300	3.6	A
78	79.21	0.98	7.0	0.9	2.0	1242 ⁺⁴⁸ ₋₄₇ ± 62	1242 ⁺⁴⁸ ₋₄₇ ± 62	8.98e+21	2500	2060	0.8	A
79	79.25	2.80	8.4	0.7	1.4	970 ⁺³⁰ ₋₃₉ ± 48	941 ⁺³⁷ ₋₃₀ ± 47	1.14e+21	160	320	5.8	A
80	79.26	-1.41	6.2	1.5	1.3	907 ⁺²⁴ ₋₃₆ ± 45	905 ⁺⁴⁴ ₋₅₈ ± 48	4.98e+21	570	860	5.8	A
81	79.36	2.92	-5.5	2.0	1.2	939 ⁺²⁶ ₋₃₄ ± 46	826 ⁺⁴⁰ ₋₆₄ ± 41	1.98e+21	210	550	27.0	A
82	79.38	-0.31	5.8	1.8	2.1	886 ⁺⁴³ ₋₃₃ ± 44	906 ⁺³⁹ ₋₂₇ ± 45	2.35e+21	710	1610	11.6	A
83	79.40	-0.46	9.1	1.6	1.3	971 ⁺³⁴ ₋₂₅ ± 48	971 ⁺³⁴ ₋₂₅ ± 48	1.73e+21	200	520	19.9	A
84	79.41	0.94	-2.5	1.4	4.6	1255 ⁺³² ₋₃₅ ± 62	1255 ⁺³² ₋₃₅ ± 62	2.98e+21	4190	5960	2.4	A
85	79.46	-1.40	5.3	1.0	1.3	917 ⁺³³ ₋₄₃ ± 45	917 ⁺³³ ₋₄₃ ± 45	2.83e+21	330	520	5.0	A
86	79.52	1.38	11.8	1.1	1.7	1247 ⁺⁵¹ ₋₃₈ ± 62	1178 ⁺⁷⁰ ₋₅₈ ± 58	1.78e+21	330	660	6.6	A
87	79.53	-0.63	6.2	1.5	6.0	933 ⁺¹⁴ ₋₁₃ ± 46	933 ⁺¹⁴ ₋₁₃ ± 46	2.60e+21	6280	10020	2.6	A
88	79.56	-0.73	-1.3	0.8	1.7	1223 ⁺⁵⁵ ₋₄₉ ± 61	981 ⁺¹⁰³ ₋₆₂ ± 49	9.19e+20	170	390	7.9	B
89	79.57	1.36	-0.0	0.5	1.7	1275 ⁺⁵⁴ ₋₄₇ ± 63	1275 ⁺⁵⁴ ₋₄₇ ± 63	1.18e+21	240	350	2.5	A
90	79.59	-1.60	-1.8	0.9	1.6	925 ⁺³⁰ ₋₃₃ ± 46	944 ⁺³⁶ ₋₃₅ ± 47	1.99e+21	340	520	4.3	A
91	79.61	-0.24	-2.6	1.4	1.4	875 ⁺²⁶ ₋₂₃ ± 43	854 ⁺³¹ ₋₂₃ ± 42	2.37e+21	330	640	9.7	A
92	79.62	0.34	-1.8	0.8	1.2	889 ⁺⁵⁴ ₋₆₀ ± 44	984 ⁺⁴⁸ ₋₈₃ ± 49	1.45e+21	140	260	7.0	A
93	79.63	-0.29	-1.9	1.8	2.3	941 ⁺¹⁶ ₋₁₇ ± 47	902 ⁺³⁸ ₋₂₅ ± 45	2.25e+21	830	1780	10.4	A
94	79.74	1.01	-1.6	1.0	1.8	1271 ⁺⁵⁴ ₋₅₁ ± 63	1239 ⁺⁴¹ ₋₄₄ ± 61	3.37e+21	740	950	3.1	A
95	79.79	-0.38	3.2	1.1	1.5	905 ⁺¹⁹ ₋₁₉ ± 45	873 ⁺²⁰ ₋₃₅ ± 43	2.19e+21	330	650	6.3	A
96	79.87	-0.41	-0.8	1.5	1.8	930 ⁺³² ₋₃₈ ± 46	974 ⁺⁶⁰ ₋₅₀ ± 48	1.95e+21	440	1000	10.4	A
97	79.89	2.48	10.4	1.1	2.3	977 ⁺¹⁰ ₋₉ ± 48	948 ⁺²³ ₋₁₉ ± 47	2.31e+21	850	1530	3.7	A
98	79.97	1.25	12.9	0.8	2.2	1276 ⁺⁷² ₋₇₈ ± 63	1276 ⁺⁷² ₋₇₈ ± 63	1.34e+21	450	930	3.3	A
99	79.97	2.67	5.6	0.8	4.6	976 ⁺⁶ ₋₆ ± 48	967 ⁺¹⁰ ₋₈ ± 48	4.52e+21	6360	6490	0.6	A
100	80.00	-0.35	0.8	1.5	1.5	899 ⁺²⁷ ₋₃₂ ± 44	888 ⁺⁴² ₋₃₄ ± 44	3.31e+21	480	700	7.5	A

Table 1 continued on next page

Table 1 (continued)

(1)	(2)	(3))	(4)	(5)	(6)	(7)	(8)	(9)	(10)	(11)	(12)	(13)
id	<i>l</i>	<i>b</i>	<i>v</i> _{LSR}	σ_v	R	<i>d</i> ^B	<i>d</i> ^A	<i>N</i> _{mean}	<i>Mass</i> _{LTE}	<i>Mass</i> _{Xfactor}	α	Adopted model
deg	deg	km · s ⁻¹	km · s ⁻¹	km · s ⁻¹	pc	pc	pc	cm ⁻²	<i>m</i> _⊙	<i>m</i> _⊙		
101	80.01	-1.27	-2.1	1.3	5.4	927 ⁺⁷ ₋₈ ± 46	923 ⁺¹⁰ ₋₈ ± 46	3.13e+21	6020	8270	1.8	A
102	80.07	2.45	8.6	1.5	2.4	1026 ⁺¹⁸ ₋₂₂ ± 51	2.82e+21	1100	2060	5.8	A	A
103	80.11	0.62	3.6	1.6	2.4	1348 ⁺⁹⁴ ₋₆₃ ± 67	1319 ⁺¹⁰⁰ ₋₈₇ ± 65	2.98e+21	1160	2100	6.3	A
104	80.23	2.91	6.9	0.7	3.0	978 ⁺¹² ₋₈ ± 48	964 ⁺¹⁶ ₋₁₆ ± 48	3.15e+21	1890	2070	1.0	A
105	80.24	-1.00	-3.7	1.4	2.3	909 ⁺¹⁸ ₋₁₉ ± 45	919 ⁺²³ ₋₂₄ ± 45	2.67e+21	950	1460	5.5	A
106	80.39	-2.33	-4.1	1.1	3.8	1110 ⁺²⁰ ₋₁₅ ± 55		2.86e+21	2710	4260	2.0	A
107	80.46	-2.95	0.7	1.2	1.2	853 ⁺²⁰ ₋₂₅ ± 42	873 ⁺³⁶ ₋₅₅ ± 43	1.37e+21	130	320	15.3	A
108	80.46	0.27	7.3	1.1	1.8	1016 ⁺³⁴ ₋₃₅ ± 50	1000 ⁺⁵⁰ ₋₅₀ ± 50	1.80e+21	370	750	6.2	A
109	80.49	0.67	-30.4	1.4	2.0	1128 ⁺⁵³ ₋₅₆ ± 56		2.39e+21	640	860	6.7	A
110	80.49	-1.19	-0.9	0.6	1.4	1018 ⁺⁵⁶ ₋₆₇ ± 50	1005 ⁺⁷¹ ₋₈₆ ± 50	2.49e+21	330	270	1.9	A
111	80.57	-0.04	1.2	1.4	1.9	1011 ⁺²⁷ ₋₂₈ ± 50		4.71e+21	1130	1550	3.9	A
112	80.58	-1.00	10.8	2.0	1.5	1006 ⁺²⁶ ₋₂₈ ± 50		1.89e+21	270	690	25.7	A
113	80.68	0.65	-2.0	1.4	3.2	1024 ⁺²⁶ ₋₂₆ ± 51	1049 ⁺³¹ ₋₂₃ ± 52	4.08e+21	2830	4000	2.7	A
114	80.72	-0.62	-4.5	1.0	2.1	1087 ⁺²⁴ ₋₂₄ ± 54		4.40e+21	1320	1910	2.0	A
115	80.73	-0.96	6.4	1.9	2.5	1090 ⁺³⁴ ₋₃₄ ± 54		2.52e+21	1020	2070	10.4	A
116	80.88	0.36	-2.1	1.4	2.3	1055 ⁺²⁶ ₋₁₈ ± 52		6.77e+21	2300	2580	2.4	A
117	80.91	-2.69	-1.2	1.3	2.3	844 ⁺¹¹ ₋₁₁ ± 42	804 ⁺¹⁸ ₋₁₈ ± 40	1.24e+21	430	1080	10.4	A
118	80.93	-0.07	5.5	1.7	10.1	982 ⁺⁹ ₋₉ ± 49	952 ⁺⁷ ₋₇ ± 47	3.14e+21	21370	34610	1.5	A
119	81.05	1.00	9.1	0.9	1.9	1058 ⁺³⁶ ₋₃₄ ± 52		2.47e+21	590	820	3.1	A
120	81.08	-0.19	-4.9	1.0	1.5		1001 ⁺³⁶ ₋₃₂ ± 50	6.63e+21	990	1090	1.6	B
121	81.14	-1.90	7.2	0.8	1.7	947 ⁺³⁵ ₋₄₀ ± 47	890 ⁺⁵⁷ ₋₆₆ ± 44	1.35e+21	250	510	5.1	A
122	81.17	1.31	-1.2	0.8	1.4	1016 ⁺⁶⁰ ₋₃₉ ± 50		1.19e+21	150	330	7.6	A
123	81.19	0.69	13.3	1.8	3.2	962 ⁺¹⁶ ₋₁₉ ± 48	825 ⁺⁴¹ ₋₄₆ ± 41	5.52e+21	3770	6550	3.0	A
124	81.22	0.88	14.6	1.6	1.8	986 ⁺²⁵ ₋₂₁ ± 49		1.08e+22	2350	3100	2.2	A
125	81.40	1.43	-4.0	1.0	1.2	808 ⁺⁶⁸ ₋₈₄ ± 40		1.20e+21	120	280	12.2	A
126	81.43	0.57	2.6	0.6	1.5		994 ⁺⁷⁰ ₋₆₆ ± 49	2.52e+21	400	360	1.7	B
127	81.45	0.35	3.2	0.9	4.1	815 ⁺¹⁰ ₋₁₀ ± 40	835 ⁺²⁵ ₋₁₈ ± 41	2.63e+21	2990	3570	1.2	A
128	81.52	-0.89	8.2	0.6	3.3	791 ⁺⁸ ₋₁₀ ± 39	832 ⁺²⁵ ₋₃₂ ± 41	2.08e+21	1510	2130	1.0	A
129	81.59	2.04	-8.9	1.1	2.6		1369 ⁻⁸⁰ ₋₇₄ ± 68	3.15e+21	1400	1850	2.8	B
130	81.63	-2.42	-2.4	1.1	2.5	827 ⁺⁸ ₋₆ ± 41	811 ⁺²⁰ ₋₂₂ ± 40	1.96e+21	820	1310	4.0	A
131	81.72	2.33	-0.3	1.2	2.0	1287 ⁺⁷⁷ ₋₉₁ ± 64		1.85e+21	480	960	6.4	A
132	81.76	0.11	8.3	1.4	3.7	828 ⁺¹⁷ ₋₁₉ ± 41		4.83e+21	4390	6100	1.9	A
133	81.79	1.76	1.3	1.1	2.5	774 ⁺¹¹ ₋₁₁ ± 38		3.62e+21	1520	2020	2.4	A
134	81.83	1.26	11.3	1.3	1.4	817 ⁺³⁵ ₋₃₈ ± 40		9.95e+21	1330	1290	2.1	A

Table 1 continued on next page

Table 1 (continued)

(1)	(2)	(3))	(4)	(5)	(6)	(7)	(8)	(9)	(10)	(11)	(12)	(13)
id	<i>l</i>	<i>b</i>	v_{LSR}	σ_v	R	d^A	d^B	N_{mean}	$Mass^{\text{LTE}}$	$Mass \times \text{factor}$	α	Adopted model
deg	deg	km · s ⁻¹	km · s ⁻¹	km · s ⁻¹	pc	pc	pc	cm ⁻²	m_{\odot}	m_{\odot}		
135	81.93	-0.60	6.9	1.6	3.5	$784^{+19}_{-16} \pm 39$		$2.74e+21$	2210	4130	4.9	A
136	81.95	1.40	4.6	1.8	4.1	$776^{+8}_{-9} \pm 38$	$751^{+9}_{-10} \pm 37$	$3.59e+21$	3950	5710	4.1	A
137	82.08	2.31	-2.7	1.5	4.1	$1048^{+36}_{-22} \pm 52$		$3.58e+21$	4050	5720	2.7	A
138	82.13	0.12	8.2	2.1	6.2	$843^{+9}_{-8} \pm 42$		$4.67e+21$	11830	16450	2.7	A
139	82.22	-1.79	3.5	1.1	7.1	$787^{+6}_{-5} \pm 39$	$772^{+6}_{-5} \pm 38$	$3.12e+21$	10550	10220	0.9	A
140	82.33	2.09	-4.2	0.8	1.3	$965^{+47}_{-50} \pm 48$		$2.39e+21$	290	340	3.2	B
141	82.42	-2.56	0.7	0.7	1.4	$822^{+21}_{-21} \pm 41$	$903^{+52}_{-70} \pm 45$	$1.26e+21$	160	280	5.0	A
142	82.78	2.52	-10.3	0.9	1.7	$993^{+37}_{-36} \pm 49$		$1.45e+21$	280	520	5.8	A
143	82.78	1.22	2.7	1.5	2.4	$761^{+13}_{-19} \pm 38$		$2.78e+21$	1030	1170	5.8	A
144	82.83	1.87	3.4	1.5	2.4	$805^{+16}_{-14} \pm 40$	$749^{+16}_{-20} \pm 37$	$2.50e+21$	990	2150	6.7	A
145	82.84	-1.47	3.1	0.7	2.1	$778^{+11}_{-11} \pm 38$	$758^{+11}_{-10} \pm 37$	$1.40e+21$	430	690	2.7	A
146	82.91	-0.14	-0.1	0.5	1.0	$725^{+37}_{-47} \pm 36$	$715^{+37}_{-33} \pm 35$	$6.04e+20$	40	90	7.8	A
147	82.95	-1.82	3.9	0.9	2.9	$806^{+11}_{-13} \pm 40$	$749^{+8}_{-12} \pm 37$	$1.84e+21$	1040	1340	2.8	A
148	82.97	3.23	-0.7	0.6	2.4		$1316^{+41}_{-43} \pm 65$	$1.31e+21$	500	890	1.8	B
149	82.98	3.31	-3.1	1.0	2.9	$1478^{+29}_{-31} \pm 73$	$1453^{+29}_{-24} \pm 72$	$2.52e+21$	1440	1990	2.3	A
150	82.98	1.64	12.7	0.8	2.3	$752^{+13}_{-16} \pm 37$	$718^{+13}_{-20} \pm 35$	$1.60e+21$	550	770	3.0	A
151	83.00	1.99	8.0	1.4	1.4	$385^{+31}_{-57} \pm 44$		$2.80e+21$	350	650	8.2	A
152	83.02	1.94	5.3	1.5	4.0	$801^{+10}_{-10} \pm 40$	$731^{+14}_{-17} \pm 36$	$2.07e+21$	2170	4490	4.7	A
153	83.21	0.24	14.8	0.8	2.8	$928^{+50}_{-41} \pm 46$	$1049^{+35}_{-31} \pm 52$	$1.56e+21$	810	1230	2.6	A
154	83.22	1.37	1.3	0.7	1.1	$811^{+44}_{-67} \pm 40$		$1.67e+21$	140	160	4.1	A
155	83.22	-3.29	2.6	1.4	2.1	$677^{+13}_{-14} \pm 33$	$733^{+32}_{-31} \pm 36$	$1.46e+21$	440	840	11.1	A
156	83.22	3.26	-4.2	0.6	2.2	$1379^{+44}_{-42} \pm 68$	$1334^{+53}_{-48} \pm 66$	$1.88e+21$	610	830	1.7	A
157	83.24	-0.15	0.7	0.6	1.8	$816^{+19}_{-19} \pm 40$	$801^{+29}_{-46} \pm 40$	$2.22e+21$	480	700	1.7	A
158	83.25	2.26	6.3	1.5	3.4	$907^{+12}_{-13} \pm 45$	$942^{+16}_{-20} \pm 47$	$1.92e+21$	1490	2800	5.6	A
159	83.25	1.46	3.0	1.1	3.4	$758^{+6}_{-8} \pm 37$	$734^{+8}_{-9} \pm 36$	$1.48e+21$	1150	2320	4.0	A
160	83.40	-1.59	4.3	1.3	2.1	$768^{+16}_{-21} \pm 38$	$721^{+15}_{-23} \pm 36$	$2.34e+21$	700	1620	6.3	A
161	83.47	-2.06	2.2	1.1	3.1	$723^{+15}_{-11} \pm 36$	$705^{+14}_{-12} \pm 35$	$3.77e+21$	2410	2820	2.0	A
162	83.55	1.75	5.1	0.8	1.9	$852^{+16}_{-23} \pm 42$	$882^{+27}_{-38} \pm 44$	$1.16e+21$	280	520	5.4	A
163	83.63	-3.65	5.3	1.3	1.2	$697^{+12}_{-18} \pm 34$	$673^{+26}_{-38} \pm 33$	$1.70e+21$	170	260	14.6	A
164	83.76	-1.91	0.3	0.8	1.3	$733^{+30}_{-37} \pm 36$	$731^{+30}_{-41} \pm 36$	$1.49e+21$	160	260	6.3	A
165	83.77	1.19	-0.8	1.0	1.4	$762^{+16}_{-17} \pm 38$	$685^{+42}_{-26} \pm 34$	$9.56e+20$	130	310	12.3	A
166	83.78	-1.33	1.1	1.7	3.4	$771^{+8}_{-9} \pm 38$	$720^{+9}_{-7} \pm 36$	$1.84e+21$	1460	3730	7.9	A
167	83.88	0.04	1.1	0.8	3.0	$769^{+10}_{-12} \pm 38$	$738^{+9}_{-9} \pm 36$	$3.10e+21$	1830	2080	1.1	A
168	83.90	-3.53	12.6	0.7	1.3	$955^{+53}_{-28} \pm 47$	$981^{+47}_{-43} \pm 49$	$1.14e+21$	140	180	5.7	A

Table 1 continued on next page

Table 1 (*continued*)

(1)	(2)	(3))	(4)	(5)	(6)	(7)	(8)	(9)	(10)	(11)	(12)	(13)
id	<i>l</i>	<i>b</i>	<i>v</i> _{LSR}	σ_v	R	<i>d</i> ^B	<i>d</i> ^A	N _{mean}	<i>Mass</i> _{LTE}	<i>Mass</i> _{Xfactor}	α	Adopted model
deg	deg	km · s ⁻¹	km · s ⁻¹	km · s ⁻¹	pc	pc	pc	cm ⁻²	<i>m</i> _⊙	<i>m</i> _⊙		
169	84.01	-1.43	2.0	1.8	1.0	787 ⁺³⁷ ₋₅₂ ± 39		2.20e+21	160	540	25.0	A
170	84.25	-0.73	2.6	1.8	5.9	745 ⁺⁴ ₋₃ ± 37	729 ⁺¹⁰ ₋₉ ± 36	2.85e+21	6570	13070	3.2	A
171	84.27	-1.93	5.6	1.0	1.2	724 ⁺¹⁸ ₋₂₂ ± 36	708 ⁺³⁵ ₋₄₆ ± 35	1.37e+21	130	310	9.5	A
172	84.47	0.17	1.3	1.4	1.4	803 ⁺²⁹ ₋₄₅ ± 40	748 ⁺¹⁴ ₋₁₈ ± 37	4.78e+21	610	1180	5.5	A
173	84.54	-1.15	6.0	1.0	2.4	732 ⁺¹¹ ₋₁₄ ± 36	738 ⁺¹³ ₋₁₀ ± 36	2.54e+21	970	1420	2.9	A
174	84.58	1.12	-6.2	1.5	3.2	782 ⁺¹¹ ₋₁₁ ± 39		3.71e+21	2530	3280	3.2	A
175	84.59	0.25	-2.7	0.7	1.1	778 ⁺³³ ₋₃₀ ± 38	737 ⁺³⁶ ₋₂₃ ± 36	7.75e+21	670	650	1.0	A
176	84.60	0.22	-0.9	0.9	1.4	765 ⁺²⁷ ₋₂₈ ± 38	742 ⁺²⁸ ₋₂₁ ± 37	1.13e+22	1410	1270	0.9	A
177	84.60	0.18	-1.8	0.9	1.1	752 ⁺⁷⁰ ₋₃₀ ± 37	760 ⁺⁶³ ₋₃₄ ± 38	1.27e+22	950	770	1.1	A
178	84.65	-0.08	2.2	1.3	1.1	725 ⁺⁵⁶ ₋₅₁ ± 36		3.53e+21	300	520	7.7	A
179	84.67	-0.25	7.9	0.8	1.8	752 ⁺²⁷ ₋₁₉ ± 37		1.20e+21	250	440	4.6	A
180	84.68	0.04	2.1	1.3	3.0	763 ⁺¹⁵ ₋₁₅ ± 38		3.96e+21	2380	2960	2.5	A
181	84.70	0.44	-1.8	1.0	2.1	927 ⁺⁴⁹ ₋₈₀ ± 46	790 ⁺²⁷ ₋₃₁ ± 39	6.98e+21	2070	2160	1.3	B
182	84.72	-1.25	3.9	1.1	1.1	830 ⁺⁴⁸ ₋₅₀ ± 41	811 ⁺⁴⁷ ₋₄₆ ± 40	2.38e+21	210	490	7.0	A
183	84.74	-4.08	5.8	0.9	1.1	695 ⁺³⁴ ₋₃₅ ± 34	681 ⁺³⁷ ₋₃₅ ± 34	1.40e+21	120	260	9.7	A
184	84.78	-1.14	1.1	1.5	3.5	762 ⁺⁶ ₋₅ ± 38	753 ⁺⁹ ₋₈ ± 37	6.63e+21	5490	6220	1.6	A
185	84.88	-0.20	-2.8	1.1	2.6	772 ⁺⁹ ₋₁₁ ± 38	686 ⁺⁸ ₋₁₁ ± 34	2.40e+21	1100	1960	3.1	A
186	84.89	-0.50	3.4	1.4	2.1	736 ⁺¹¹ ₋₁₅ ± 36	688 ⁺¹² ₋₁₂ ± 34	2.00e+21	610	1230	7.6	A
187	84.91	-0.42	0.3	1.8	1.1	794 ⁺²⁸ ₋₃₀ ± 39	704 ⁺²⁶ ₋₂₂ ± 35	2.24e+21	170	430	24.1	A
188	84.92	1.08	-2.0	0.6	1.4	833 ⁺²² ₋₂₇ ± 41	811 ⁺²⁶ ₋₂₂ ± 40	2.92e+21	390	450	1.7	A
189	84.93	-0.55	-4.5	0.9	1.4	760 ⁺²⁰ ₋₂₇ ± 38	687 ⁺¹⁴ ₋₁₅ ± 34	4.08e+21	560	760	2.6	A
190	84.99	-1.22	2.7	1.5	2.5	735 ⁺¹⁰ ₋₇ ± 36	707 ⁺²⁰ ₋₂₀ ± 35	4.48e+21	1920	2990	3.4	A
191	85.06	-0.25	-5.5	1.1	1.9	781 ⁺¹³ ₋₁₆ ± 39	688 ⁺⁹ ₋₁₀ ± 34	6.05e+21	1500	1660	1.8	A
192	85.07	0.41	-1.9	1.1	2.8	789 ⁺¹⁵ ₋₁₈ ± 39	761 ⁺²³ ₋₂₄ ± 38	4.31e+21	2250	2360	1.7	A
193	85.07	-1.15	4.2	1.3	3.4	745 ⁺¹⁰ ₋₈ ± 37	731 ⁺⁸ ₋₈ ± 36	4.18e+21	3160	4530	2.0	A
194	85.07	-0.22	0.8	1.0	1.4	774 ⁺¹¹ ₋₁₄ ± 38		2.19e+21	290	540	5.4	A
195	85.08	0.06	-0.4	0.7	1.2	770 ⁺²⁰ ₋₂₅ ± 38		1.96e+21	200	370	3.9	A
196	85.29	-4.15	5.9	1.0	1.5	704 ⁺²⁷ ₋₂₁ ± 35	699 ⁺⁴¹ ₋₃₁ ± 34	1.56e+21	230	500	8.1	A
197	85.33	-4.68	7.2	0.7	1.0	740 ⁺³¹ ₋₃₅ ± 37	731 ⁺³⁵ ₋₄₈ ± 36	1.06e+21	70	140	8.8	A
198	85.35	-2.16	13.5	1.1	1.0	561 ⁺²⁵ ₋₄₂ ± 28	688 ⁺³³ ₋₃₆ ± 34	1.15e+21	80	130	19.2	A
199	85.39	-3.16	10.7	0.8	0.8	514 ⁺²² ₋₂₈ ± 25		8.91e+20	40	70	16.1	A
200	85.84	-2.16	1.9	0.5	1.0	556 ⁺²¹ ₋₃₂ ± 27		8.52e+20	50	90	5.8	A
201	85.85	-2.07	12.9	1.5	1.6	543 ⁺⁸ ₋₉ ± 27	540 ⁺⁸ ₋₉ ± 27	1.34e+21	240	530	18.7	A
202	86.46	0.29	-15.0	1.1	1.3	654 ⁺²⁴ ₋₂₆ ± 32	649 ⁺²⁵ ₋₂₁ ± 32	1.82e+21	200	330	9.7	A

Table 1 *continued on next page*

Table 1 (*continued*)

(1)	(2)	(3))	(4)	(5)	(6)	(7)	(8)	(9)	(10)	(11)	(12)	(13)
id	<i>l</i>	<i>b</i>	v_{LSR}	σ_v	R	d^A	d^B	N_{mean}	$Mass^{\text{LTE}}$	$Mass^{\text{Xfactor}}$	α	Adopted model
deg	deg	km · s ⁻¹	km · s ⁻¹	pc	pc	pc	pc	cm ⁻²	m_{\odot}	m_{\odot}		
203	86.48	0.34	0.5	1.3	2.0	$682^{+11}_{-12} \pm 34$	$684^{+9}_{-13} \pm 34$	$3.18e+21$	830	1340	4.8	A
204	86.52	3.06	5.6	0.8	3.6	$2272^{+90}_{-117} \pm 113$	$1.17e+21$	1000	1540	2.4	B	
205	86.61	-2.09	13.5	1.2	1.8	$536^{+6}_{-6} \pm 26$	$535^{+16}_{-24} \pm 26$	$1.12e+21$	250	600	12.8	A
206	86.69	2.40	-3.5	1.0	4.4	$2387^{+50}_{-44} \pm 119$	$2389^{+47}_{-42} \pm 119$	$1.71e+21$	2230	4350	2.2	A
207	86.87	-4.10	5.1	0.8	1.0	$705^{+21}_{-27} \pm 35$	$709^{+19}_{-33} \pm 35$	$1.24e+21$	90	120	9.3	A

NOTE—(see the online version for a full machine-readable version of this table.)

(1) id: Cloud ID in this work of distanced measured molecular clouds, sorted by longitude.

(2) *l*: Longitude of cloud center weighted by intensity, see Equation (3).

(3) *b*: Latitude of cloud center weighted by intensity, see Equation (4).

(4) v_{LSR} : Velocity of cloud center weighted by intensity, see Equation (8).

(5) σ_v : Intensity weighted velocity dispersion of clouds, see Equation (9).

(6) R: Physical size of molecular cloud, in unit of pc, see Equation (17).

(7) d^A : Median value of cloud distance measured using Model A. The uncertainties represent 16-th/84-th value in MCMC samples of cloud distance measured using Model A (Lower/Upper value of 1 σ confidence interval).

(8) d^B : Median value of cloud distance measured using Model B. The uncertainties represent 16-th/84-th value in MCMC samples of cloud distance measured using Model B (Lower/Upper value of 1 σ confidence interval).

(9) N_{mean} : The mean column density of each cloud based on LTE, which is calculated by Equation (13) and (16).

(10) $Mass^{\text{LTE}}$: LTE mass derived from ^{13}CO emission with determined distance, which is calculated by column density of ^{13}CO emission, see Equation (13) and (18).

(11) $Mass^{\text{Xfactor}}$: Mass calculated by ^{12}CO emission with determined distance, in a ^{13}CO traced cloud boundary. The CO-to-H₂ Conversion Factor adopts $X_{\text{CO}} = 2 \times 10^{20} \text{ cm}^{-2} (\text{K} \cdot \text{km} \cdot \text{s}^{-1})^{-1}$.

(12) Virial parameter of ^{13}CO traced cloud, which is calculated by Equation (21).

(13) Adopted model: Determine which model to give a more accurate distance.

Table 2. Physical Properties of molecular clouds matched with masers

id	<i>l</i>	<i>b</i>	parallax ^a	parallax error ^a	<i>v</i> _{maser} ^a	<i>v</i> _{LSR}	σ_v	<i>T</i> _{peak}	Column Density	<i>R</i> _{eff}	mass	α_{vir}
			(°)	(°)	mas	mas	km · s ⁻¹	km · s ⁻¹	km · s ⁻¹	K	cm ⁻²	pc
m1 ⁽¹⁾	73.93	-1.86	0.629	0.017	5.0	5.6	1.3	6.9	3.4e+21	5.8	7580	1.4
m2 ⁽²⁾	74.56	0.79	0.367	0.083	-1.0	-0.6	1.0	4.6	2.8e+21	2.7	1420	2.3
m3 ⁽¹⁾	76.39	-0.66	0.770	0.053	-2.0	-2.1	1.3	10.6	9.6e+21	1.1	810	2.8
m4 ⁽³⁾	78.12	3.63	0.645	0.030	-6.0	-3.3	1.3	7.9	9.8e+21	0.6	250	4.6
m5 ⁽⁴⁾	78.60	0.89	0.300	0.010	-5.7	-5.3	1.7	10.8	3.1e+21	14.1	41530	1.2
m6 ⁽⁵⁾	79.74	1.01	0.737	0.062	-3.0	-1.6	1.0	4.5	3.3e+21	1.9	840	2.9
m7 ⁽¹⁾	79.87	1.19	0.620	0.027	-5.0	-4.2	1.2	8.0	9.9e+21	0.6	290	3.6
m8 ⁽⁶⁾	80.39	-2.33	0.620	0.047	-3.0	-4.1	1.1	8.4	2.9e+21	5.5	5770	1.3
m9 ⁽⁵⁾	80.88	0.36	0.687	0.038	-3.0	-2.1	1.4	11.7	7.0e+21	3.1	4510	1.7
m10 ⁽⁵⁾	80.91	-0.28	0.666	0.035	-3.0	-3.4	1.0	10.9	9.5e+21	1.1	770	1.7
m10 ⁽⁷⁾	80.98	-0.13	0.666	0.035	-3.0	-3.1	0.8	10.6	1.0e+22	1.3	1180	0.8
m10 ⁽⁷⁾	80.99	-0.09	0.666	0.035	-3.0	-2.4	0.9	10.0	6.9e+21	0.8	300	2.7
m10 ⁽⁷⁾	81.08	-0.19	0.666	0.035	-3.0	-4.9	1.0	14.1	7.8e+21	2.2	2620	0.9
m10 ⁽⁷⁾	81.22	0.88	0.666	0.035	-3.0	14.6	1.6	10.9	1.1e+22	2.7	5790	1.4
m10 ⁽⁷⁾	81.35	-0.05	0.666	0.035	-3.0	-5.0	1.2	16.3	1.1e+22	3.6	9440	0.7
m10 ⁽⁷⁾	81.54	0.09	0.666	0.035	-3.0	-6.0	1.0	11.0	7.5e+21	2.3	2740	0.9
m10 ⁽⁷⁾	81.57	0.71	0.666	0.035	-3.0	-1.6	1.0	14.4	8.0e+21	3.8	7700	0.5
m10 ⁽⁷⁾	81.61	-0.03	0.666	0.035	-3.0	9.6	1.0	10.1	5.7e+21	2.3	2110	1.4
m10 ⁽⁷⁾	81.64	0.49	0.666	0.035	-3.0	-2.0	0.7	10.1	1.4e+22	0.5	230	1.1
m10 ⁽⁷⁾	81.64	0.75	0.666	0.035	-3.0	8.5	0.8	10.4	5.9e+21	1.4	770	1.2
m10 ⁽⁷⁾	81.74	0.58	0.666	0.035	-3.0	-4.1	1.7	17.3	2.2e+22	0.9	1390	2.4
m10 ⁽⁷⁾	81.83	0.97	0.666	0.035	-3.0	-0.7	1.1	14.6	7.5e+21	2.9	4140	1.0
m10 ⁽⁷⁾	81.83	1.26	0.666	0.035	-3.0	11.3	1.3	13.3	1.0e+22	2.6	4630	1.1
m10 ⁽⁷⁾	81.86	0.88	0.666	0.035	-3.0	-2.1	1.1	15.9	1.2e+22	2.3	4160	0.7
m11 ⁽⁵⁾	81.95	0.71	0.772	0.042	7.0	11.2	1.7	11.6	6.4e+21	2.6	2990	3.1

Note.

a: Parameters derived from masers measurement;

(1): Cloud parameters of m3 (Xu et al. 2013) are alternatively from S106 cloud or G076.39-0.66, here is the latter one (see Section 5.5) ;

(2): (Burns et al. 2014);

(3): (Moscadelli et al. 2011; Nagayama et al. 2015);

(4): (Rygl et al. 2011);

(5): DR20 (m9), DR21 (m10), W 75N (m11) (Rygl et al. 2012);

(6): (Zhang et al. 2012);

(7): Clouds associated with DR21 filament (Rygl et al. 2012).

6. DISCUSSION

6.1. Big picture

6.1.1. The Cygnus Rift

Cygnus Rift is a foreground molecular structure in Cygnus complex (Hiltner & Johnson 1956; Dame & Thaddeus 1985), which makes heavy obscuration in optical images. Dame & Thaddeus (1985) assumed that the Rift is confused together with Cygnus X above $l=74^\circ$. However, the exact spatial and distance distribution is still on debate, especially in the part overlapping with the background Cygnus X star-forming region. What's the real extension of Cygnus Rift in true 3D space? What's the accurate distances for different gas distribution for the whole Cygnus region? What's the difference between the molecular gas in Cygnus X star-forming region and those in Cygnus Rift?

The overall distributions of MCs toward the Cygnus region (including both the Cygnus X star-forming region and the foreground Cygnus Rift) show multiple gas layers based on our new measurements (see Section 5). We reveal that clouds in 800 pc gas layer mainly concentrate along the 800 pc loop, mainly including the foreground emission of the

Table 3. Physical Properties of MCs matched with PDR interfaces

id	<i>l</i>	<i>b</i>	<i>v</i> _{LSR}	σ_v	<i>T</i> _{peak}	Column Density	<i>R</i> _{eff}	mass	α_{vir}
	($^{\circ}$)	($^{\circ}$)	$\text{km} \cdot \text{s}^{-1}$	$\text{km} \cdot \text{s}^{-1}$	K	cm^{-2}	pc	M_{\odot}	
p1 ^a	76.94	2.22	1.4	1.1	17.2	6.0e+21	4.3	7440	0.8
p2 ^b	77.22	1.52	0.0	0.8	7.8	3.3e+21	0.8	140	4.0
p3 ^a	77.47	1.85	1.4	1.4	13.3	1.1e+22	4.6	16170	0.6
p4 ^c	77.97	0.03	-2.5	1.2	6.5	3.6e+21	2.7	1830	2.6
p5 ^a	77.98	1.77	-1.9	1.0	11.7	8.4e+21	3.4	6490	0.6
p6 ^c	78.00	0.56	-2.5	2.0	7.3	6.3e+21	2.0	1610	5.5
p7 ^c	78.16	-0.31	-0.5	2.1	7.1	6.4e+21	2.7	3080	4.3
p8 ^b	78.46	2.67	0.5	0.8	15.2	1.4e+22	1.0	980	0.9
p9 ^a	79.18	2.21	-2.2	0.8	11.1	8.3e+21	1.4	1120	1.0
p10 ^d	79.26	0.25	3.4	1.0	10.0	6.2e+21	1.0	440	2.8
p11 ^d	79.87	1.19	-4.2	1.2	8.0	9.9e+21	0.7	330	3.4
p12 ^d	79.98	0.84	-10.8	1.2	12.5	9.6e+21	1.3	1150	1.8
p13 ^d	80.38	0.44	8.3	0.9	16.8	1.3e+22	1.0	890	1.0
p14 ^d	80.84	0.56	11.6	1.0	8.8	8.4e+21	1.0	600	2.1
p15 ^e	80.91	-0.28	-3.4	1.0	10.9	9.5e+21	1.2	980	1.5
p16 ^e	80.98	-0.13	-3.1	0.8	10.6	1.0e+22	1.5	1510	0.7
p17 ^e	81.08	-0.19	-4.9	1.0	14.1	7.8e+21	2.5	3360	0.8
p18 ^a	81.27	1.05	15.5	0.7	7.9	7.4e+21	0.8	350	1.3
p19 ^a	81.50	0.48	7.0	0.8	11.6	7.7e+21	1.5	1120	1.1

Note.

a: Cometary clouds are likely shaped by Cygnus OB associations.

b: Irregular clouds.

c: Oval-shaped HII regions identified by Downes & Rinehart (1966), in order: DR9, DR6 and DR13.

d: Globules near the center of FUV sources.

e: Clouds match a hub-like HII region in Cygnus X North, see panel (e) of Figure 8.

Table 4. Mass Evaluation

Region	Comments	LTE M_{\odot}	X-factor M_{\odot}	by ^{13}CO (2-1) ^a M_{\odot}
Cygnus	by Table 1	2.4×10^5	3.5×10^5	
	by Table 1~3	4×10^5	5.3×10^5	
	Whole	1.1×10^6	2.7×10^6	
Cygnus within 1 kpc	by Table 1	2.6×10^5	6.2×10^5	
Cygnus X	Cygnus X North (0~3 kpc)	2.3×10^5	4×10^5	
	Cygnus X North (1.3~1.7 kpc)	1.7×10^5	3.2×10^5	2.8×10^5
	Cygnus X South (0~3 kpc)	4.1×10^5	8.3×10^5	
	Cygnus X South (1.3~1.7 kpc)	3.2×10^5	7×10^5	4.5×10^5

Table 4. The mass estimated in different sub-regions/distance intervals.

a: Estimated by Schneider et al. (2006) based on ^{13}CO (2-1) and the LTE method;

Cygnus X North and NAP region therein (see Sections 5.1 and 5.3). Based on the MC distance measurements toward the whole region, the 800 pc gas layer also extends to the Cygnus X South region. The 800 pc gas layer extends to at least ~ 135 pc along the longitude and a thickness of ~ 80 pc (i.e., the fwhm of Gaussian fitting from distances distribution of MCs). The average value and variance of the column density in this layer ($700 \text{ pc} \leq d \leq 900 \text{ pc}$) are $3.1 \times 10^{21} \text{ cm}^{-2}$ and $2.3 \times 10^{21} \text{ cm}^{-2}$, respectively.

The 1 kpc gas layer is also widespread in both of the Cygnus X North and Cygnus X South regions. We find that these clouds have similar velocity distributions, peak temperature, and mean column density. Based on our results, we attribute them as a whole gas layer at ~ 1 kpc, nevertheless the clouds in the Cygnus X North region are slightly more distant. Similarly, we estimate the length and depth of the 1 kpc gas layer with ~ 145 pc along the longitude and a thickness of ~ 70 pc, respectively. The average value and variance of the column density in this layer ($900 \text{ pc} \leq d \leq 1100 \text{ pc}$) are $2.5 \times 10^{21} \text{ cm}^{-2}$ and $1.2 \times 10^{21} \text{ cm}^{-2}$, respectively.

Combining the 800 pc and 1 kpc gas layers, the Cygnus Rift is distributed across a large spatial extent of at least in $l=[72, 87]$ deg and $b=[-5, 4]$ deg. The distance of Cygnus Rift ranges from nearer NAP region ($\gtrsim 700$ pc) to further gas layers (e.g., Cygnus X North, Cyg-NW at 1 kpc) according to MCs' distances. These dark clouds toward the region, composing multiple gas layers with slightly different distances. The accumulation of molecular gas along these layers makes large extinction in some directions (i.e. the “extinction wall” effect, [Straizys et al. 1993](#)). Therefore it is hard to determine the distances for the distant MCs behind the Cygnus Rift. For example, the contamination from foreground emission at the Cygnus Rift leads to biased distance measurement in previous studies to S106. The average value and variance of the column density of combined layers are $2.8 \times 10^{21} \text{ cm}^{-2}$ and $1.9 \times 10^{21} \text{ cm}^{-2}$, respectively.

As is presented above, the molecular gas in Cygnus Rift is better identified and measured. It plays an important role on revealing the 3D view along the LOS. Studying molecular gases (e.g., distributions and physical properties) in the foreground is also helpful to reveal the MCs behind them. For example, we may reveal the detailed gas structures associated with the high-energy emission from Cygnus Cocoon ([LHAASO Collaboration 2024](#)) We need more advanced methods (e.g., multi-jump) to properly separate the gas at different distances. Finally, a big picture of the whole region will be well delineated.

6.1.2. Molecular Gas behind the Cygnus Rift

The distribution of clouds in the 1.3 kpc gas layer is different between the Cygnus X North and South region. The majority of clouds in this layer are located in South region based on our distance measurements (see Section 5.2, also see the special cases measured only by Model B in Appendix D). The result also agrees with the previous studies ([Zucker et al. 2020](#); [Dharmawardena et al. 2022](#)). However, it does not mean that there is no molecular gas at 1.3 kpc gas layer in the Cygnus X North region. We propose clouds (see m11 in Table 2 and Figure 10a) associated with W 75N (~ 1.3 kpc, [Rygl et al. 2012](#)) in the Cygnus X North are also in this layer. These clouds' distances are relatively smaller than that of the Cygnus North filament (~ 1.5 kpc for DR20 and DR21 in [Rygl et al. 2012](#)). We notice clouds in this layer have slightly larger brightness temperature and mean column densities than the clouds within 1 kpc (see Figure 12). The clouds are probably heated by nearby star-forming regions, i.e. substructures of Cygnus OB2 identified by [Berlanas et al. \(2019\)](#) and [Orellana et al. \(2021\)](#).

We note 1.3 kpc layer is also distributed extensively (see middle layer in Figure 17) based on the MWISP data and our results. It's interesting that some clouds associated with HII regions (DR6, DR9, DR13 etc.) have similar physical properties with those clouds in 1.3 kpc layer (see Figure 12). Furthermore, DR13 cloud (see id 48 in Table 1) has been measured in 1320_{-157}^{+182} pc, supporting the association between the heated molecular gas and PDR interfaces. Therefore some clouds with intense infrared emission are probably located in the 1.3 kpc layer, although we temporarily put the clouds matching with infrared structures (Table 3) at ~ 1.7 kpc.

On the contrary, few clouds in the 1.3 kpc gas layer toward the Cygnus X North are successfully measured in our method. We suspect that the majority of molecular gas behind the 800 pc and 1 kpc gas layers are likely located at ~ 1.5 kpc. For example, the massive Cygnus North Filament (see Figure 10a) contributes to the majority of CO emission in this region, which also agrees with the presence of a densest region toward Cygnus X North at ~ 1.5 kpc ([Dharmawardena et al. 2022](#); [Rygl et al. 2012](#)).

Clouds associated with background PDR interfaces in both regions are likely related to the Cygnus OB2, while cometary clouds in Cygnus X South (labeled in A, B, C and S106, see Figures 11 and 16) could also be influenced by star members in Cygnus OB1 (~ 1.7 kpc from [Quintana & Wright 2021](#); [Rastorguev et al. 2023](#)). In addition, the molecular gas is likely concentrated in 1.5 kpc toward the Cygnus X North region (see blue histogram in right panel

in Figure 7). On the other hand, the gas in the Cygnus X South region is mainly at ~ 1.3 and ~ 1.7 kpc. Actually, only two MCs (id 19 and 67 in Table 1) in the Cygnus X South region are at 1.5 kpc with Model B. These indicate the different molecular gas distribution between the Cygnus X North and South regions. We suggest that the Cygnus X star-forming region is not an integral structure located in the same distances based on maser measurements and our new MC distance measurements from Gaia DR3.

6.1.3. Comparison with the distribution of YSOs

Furthermore, we use selected YSO candidates (see Appendix F) to trace the spatial distribution of young stars toward the Cygnus region. We find that the majority of YSO candidates spatially coexist very well with the ^{13}CO structures, especially for molecular gas within 1 kpc (see Figure 17). Along the 800 pc gas loop (see 800 pc layer in Section 5.1), the significant over-density of YSO candidates can be found toward the NAP region and the superposed sub-region toward the Cygnus X North (see Figure 10b), while the coincidence between the YSOs and molecular gas is also discerned in L914 and molecular gas at $[l \sim 83, b \sim 2]$ deg. Additionally, over-density of YSO candidates also coincides with the molecular gas in the Cygnus X South region. Different from the Cygnus X North region, the distribution of YSO candidates extends to further gas layers. It again indicates the 1.3 kpc middle gas layer is mainly distributed toward the Cygnus X South region.

Behind the Cygnus Rift, YSOs still roughly follow the distribution of molecular gas. Interestingly, the spatial distribution of YSO candidates is much more extended toward the star-forming regions at $\gtrsim 1.4$ kpc. We find that the over-densities of YSOs are roughly associated with identified molecular gas and OB associations in those regions.

For the multiple gas layers, the results reveal that a significant over-density of potential young stars occurs in the vicinity of molecular gas traced by ^{13}CO , indicating the connection between them.

6.2. Molecular gas mass toward the Cygnus Region

A summary to the derived masses is listed in Table 4. Here we first discuss the total mass of the molecular gas based on ^{13}CO emission in LTE (see equation 14 and 18). Obviously the fractional detection rate (FDR) of clouds with distance has a major influence on the total mass estimation. FDR can be estimated by the ratio of flux between distance measured clouds (see Tables 1-3) and raw data.

Firstly we defined FDR_1 (here 48.6% for the whole region) as the flux ratio between MCs with distance and the total identified ^{13}CO clouds. Secondly, FDR_2 , the flux ratio between the total identified ^{13}CO clouds and masked raw data is 72.6% (see Section 3.2). Thus we obtain $FDR = FDR_1 \times FDR_2 = 35.3\%$. The total mass of clouds with known distances in Cygnus traced by ^{13}CO structures, including clouds within 1 kpc and Cygnus X massive star formation regions, is about $M_{\text{Table1-3}} \sim 4 \times 10^5 M_\odot$, leading to the total mass $M_{\text{overall}} \sim 1.1 \times 10^6 M_\odot$ for the whole region.

We note that FDR_1 in different layers are not the same, which has a dominant influence on the total mass estimation in Cygnus traced by ^{13}CO . In addition, the beam filling factor (Yan et al. 2021c; Sun et al. 2021b) and the smaller coverage of ^{13}CO emission would lead to the underestimation of the molecular gas mass. So the total mass estimated above is still a lower limit toward the whole Cygnus region traced by ^{13}CO emission.

Alternatively, we further use ^{12}CO emission to estimate the total mass of molecular gas toward the whole Cygnus region. For each identified ^{13}CO structure, we give an X-factor mass from corresponding ^{12}CO emission in the same PPV space. Similarly, the molecular mass can be estimated to be $M_{\text{Table1-3}}^{\text{Xfactor}} \sim 5.3 \times 10^5 M_\odot$ for the corresponding ^{13}CO structure by adopting $X_{\text{CO}} = 2 \times 10^{20} \text{cm}^{-2} (\text{K} \cdot \text{km} \cdot \text{s}^{-1})^{-1}$ (Bolatto et al. 2013). The ^{12}CO flux ratio between the identified structures with distance and the raw data is about 19.5%, leading to the total molecular mass of $M_{\text{overall}}^{\text{Xfactor}} \sim 2.7 \times 10^6 M_\odot$ in the whole Cygnus region. Considering the underestimation of FDR_1 in above calculation, the estimated mass of $M_{\text{overall}}^{\text{Xfactor}} \sim 2.7 \times 10^6 M_\odot$ is still a lower limit.

In Table 4, we make further efforts to estimate the mass of molecular gas within 1 kpc (mainly from Cygnus Rift). Similar to above analysis, we use $FDR_2 = 72.6\%$ and $FDR_1 \sim 1$ to evaluate the total mass within 1 kpc. According to Table 1, the total molecular mass within 1 kpc is estimated to be $M_{1\text{kpc}}^{\text{LTE}} \sim 2.6 \times 10^5 M_\odot$. Assuming the same ratio from $M_{\text{overall}}^{\text{Xfactor}} / M_{\text{overall}}^{\text{LTE}}$ for the gas layers within 1 kpc, the low limit of $M_{1\text{kpc}}^{\text{Xfactor}}$ is about $6.2 \times 10^5 M_\odot$ because the emissions of those small structures are ignored.

For comparison with previous work (e.g., Schneider et al. 2006), we evaluate the mass of the Cygnus X region. For the Cygnus X North region ($FDR_1 = 59.3\%$, $FDR_2 = 83.9\%$), the total mass (0-3 kpc) of molecular gas is $M_{\text{CygNorth}}^{\text{LTE}} \sim 2.3 \times 10^5 M_\odot$ and $M_{\text{CygNorth}}^{\text{Xfactor}} \sim 4 \times 10^5 M_\odot$, respectively. Assuming $FDR_1 \approx 1$ for foreground molecular gas within 1 kpc, we estimated that molecular mass from background emission (mainly from 1.3 to 1.7 kpc) is

$M_{\text{CygNorth}}^{\text{LTE}} \sim 1.7 \times 10^5 M_{\odot}$ and $M_{\text{CygNorth}}^{\text{Xfactor}} \sim 3.2 \times 10^5 M_{\odot}$ by subtracting the foreground mass. Similarly, for the Cygnus X South region ($FDR_1 = 48.9\%$, $FDR_2 = 74.6\%$), the total molecular mass is $M_{\text{CygSouth}}^{\text{LTE}} \sim 4.1 \times 10^5 M_{\odot}$ and $M_{\text{CygSouth}}^{\text{Xfactor}} \sim 8.3 \times 10^5 M_{\odot}$. Additionally, the molecular mass associated with the nearby star-forming region are $M_{\text{CygSouth}}^{\text{LTE}} \sim 3.2 \times 10^5 M_{\odot}$ and $M_{\text{CygSouth}}^{\text{Xfactor}} \sim 7 \times 10^5 M_{\odot}$ for $1.3 \sim 1.7$ kpc.

The total mass toward Cygnus X in $1.3 \sim 1.7$ kpc is $M_{\text{CygX}}^{\text{LTE}} \sim 4.9 \times 10^5 M_{\odot}$, $M_{\text{CygX}}^{\text{Xfactor}} \sim 1 \times 10^6 M_{\odot}$, respectively. We note $\sim 20\%$ flux toward the direction is from the molecular gas within 1 kpc. We also attached the mass evaluated by ^{13}CO (2→1) (Schneider et al. 2006) based on LTE method. Our new results are supposed to be smaller than those of Schneider et al. (2006), knowing that we put part of the MCs in a closer place (e.g., the gas layers within 1 kpc). On the other hand, the difference of estimated molecular mass between the two works is likely from the different transitions from ^{13}CO .

6.3. From PPV to PPP

It is sometimes assumed that the CO emission in PPV space corresponds to coherent structures in PPP space. However, in the simulation results in Beaumont et al. (2013), there are two possible problems in cloud decomposition from PPV to PPP. The one is that the gas emission with different velocity components (thus probably with different distances) are combined into the same spatial structure. And the other is that clouds belonging to a coherent structure in real three dimensional space exhibit two or more velocity components that are separated in PPV space. Due to the prevalent feedbacks from star-forming activities, great caution must be exercised when discussing the properties of identified features in PPV space (Clarke et al. 2018). Many of structures with a single feature in PPV space would not be directly identified as coherent features in PPP space. For example Perseus Arm in longitude–velocity diagram is not a continuous structure in true spatial space (Peek et al. 2022) based on 3D dust map (Green et al. 2019). We also find that some identified gas structures with different velocities are located at the same distance (e.g., see Figures 9, 12 and 14).

Without distance measurement, cloud clustering methods can actually introduce two problems. One is over decomposition to the whole MC complex linked by many substructures with different velocity features, while the other is that a mistaken aggregation of unrelated structures in PPP space because of close velocities. In our work, we confirmed that the clouds in NAP region are from a whole MC complex, although the algorithm decompose the complex into different velocity structures (see Section 5.3, Figures 13 and 14). On the contrary, it's necessary to avoid wrong aggregation of different spatial structures, considering the complicated velocity structure toward Cygnus region. For the first case, with the distance measurement, substructures from the over decomposition can be linked together to form larger cloud complexes (see the 800 pc loop with a large extension of $\sim 4 \times 4$ deg in Figure 17). Finally, many identified MCs with close velocities are indeed located in different distances based on our cloud clustering and distance measurements (see Figures 8 and 11). Therefore, accurate distance measurements, together with appropriate cloud clustering, allow us to better describe the true distribution of molecular gas in the milky way.

Adler & Roberts (1992) indicate that the size-line-width relationship from modeling galactic disk is not a reliable indicator of the physical nature of cloud complexes. We also caution against using the results of clustering MCs with various methods and size-line-width relation from PPV space (Shetty et al. 2010; Pan et al. 2015) without accurate distance measurement. Our results clearly demonstrate a very wide range of distances for clouds with close velocities toward the Cygnus region. And conversely, clouds located in the same layers might have very different velocity features (see Figures 9 and 12). From this work, we propose that the studies of MCs within 3 kpc should be revisited in details at the Gaia's age of precise astronomy (Zucker et al. 2023). The true 3D distribution of MCs is essential to construct large-scale structure of our Galaxy.

7. SUMMARY

We study the properties and distribution of MCs toward the Cygnus region (~ 150 deg 2) from the MWISP CO survey. Here we summarise the main conclusions in this work:

(1) We identified 3829 structures based on coherent spatial and velocity structures of ^{13}CO emission. About 72.6% fluxes are recovered after Gaussian decomposition and clustering from GaussPy+ and ACORNS.

(2) Combining the identified cloud structures and data from Gaia DR3, we design two models (A and B) to measure distances of molecular gas in the Cygnus region. Among the identified ^{13}CO structures, we obtain distances for over 200 large clouds (i.e., ≥ 60 arcmin 2). 120 clouds are measured both by Model A and B (class I). 22 clouds are only

measured by Model B (class II), and over 60 clouds are alone measured by Model A (class III). The flux of MCs with distance (Class I and II in Table 1) contributes to about 31.2% total flux of the identified ^{13}CO structures.

(3) About 20 clouds are coincident well with bright mid-IR emission (see panel e in Figures 8 and 11, also see Table 3). The association between the MCs and surrounding star-forming regions are also supported by MC properties (cometary morphology, high peak temperature and intense emission of the gas, etc.). Moreover, based on our models, some clouds with oval-shaped and irregular morphology (e.g., DR13) are indeed measured to be ~ 1.3 kpc. These clouds associated with PDR interfaces are probably related to OB subgroups at ~ 1.3 kpc.

(4) Additionally, we find that tens of MC structures are associated well with masers in Table 2. The distances of these MCs can be obtained based on the association between masers and the corresponding molecular gas. We also find that our independent measurement of a cloud (cloud 94 in Table 1) is consistent with the corresponding maser's distance of 1.36 kpc (Rygl et al. 2012).

(5) The spatial distribution of YSOs candidates coincides well with ^{13}CO structures within 1 kpc, indicating the tight connection between them. These cases in (2)(3)(4)(5) show that our models are effective for distance measurement to MCs in velocity crowding regions.

(6) Our distance measurements of MCs, combined with the additional information from molecular gas associated with masers and nearby OB associations, show that there are multiple layers of gas structure toward Cygnus region: (I) The gas in 800 pc and 1 kpc layer composing Cygnus Rift, (II) the 1.3 kpc layer majorly in Cygnus X South, and (III) the Cygnus North Filament and the adjacent dense gas at 1.5 kpc, as well as many cometary MCs directly shaped by Cygnus OB associations at ~ 1.7 kpc (see Figure 17). The results reveal the complex distribution of molecular gas toward Cygnus region, both in spatial and velocity distribution. The total masses of molecular gas of the whole Cygnus region is $\sim 1.1 \times 10^6 M_{\odot}$ by LTE, and $\sim 2.7 \times 10^6 M_{\odot}$ by X-factor (see Table 4).

(7) Our work determines the large spatial extent of Cygnus Rift at least in $l=[72, 87]$ deg and $b=[-5, 4]$ deg. The distances of the MCs are well determined in the range of 700 pc to 1 kpc, revealing the multi-layer nature toward the Cygnus Rift (see Figures 7 and D1). For example, the foreground gas toward the Cygnus X North region is composed by 800 pc and 1 kpc layers. The superposition of gas structures toward L889 in the Cygnus X South also exists. The large extinction of the foreground gas in these directions cause the failure of distance measurement for MCs at larger distances (i.e., “extinction wall” effect). The molecular mass of the foreground Cygnus Rift (within 1 kpc) contains $\sim 25\%$ of the whole region.

(8) We propose that molecular gas associated with Cygnus X star-forming region does not come from an integral structure. Actually, there are different molecular structures at different distances, such as ~ 1.3 kpc molecular gas that are likely associated with subgroups of Cygnus OB2, the dense gas in Cygnus North Filament at ~ 1.5 kpc, and the cometary MCs shaped by Cygnus OB associations at ~ 1.7 kpc (see histogram in right panel of Figure 7). Toward the Cygnus X star formation region, the molecular gas within $1.3 \sim 1.7$ kpc is about $\sim 4.9 \times 10^5 M_{\odot}$ by LTE, and $\sim 1 \times 10^6 M_{\odot}$ by X-factor.

We find that abnormal jumps and/or multi-jump features of $A_{\text{G}}\text{-Distance}$ map are common toward the Cygnus region. Besides the gas layers discussed above, there are likely other gas structures at different distances in the whole region. For example, some MCs at ~ 550 pc (i.e. clouds 198 to 203 and 205 in Table 1, also see light red contours in Figure 17) are in front of Cygnus Rift in the region $l \geq 85.3$ deg. These clouds have relatively small sizes and column density, thus contribute to small proportion of mass within 1 kpc (see histograms in Figure 7). These clouds at 500-600 pc are probably related to the MC complex toward the Cygnus OB7. We indeed detect that two jump features are exactly at ~ 550 pc and ~ 760 pc in NAP region, corresponding to the different gas layer therein. We propose that multi-layer nature of molecular gas is ubiquitous. We will develop a multiple jumps detection model to further reveal the 3D molecular gas distribution of Cygnus region in a forthcoming paper.

Acknowledgments. We would like to thank the anonymous referee for the valuable comments and suggestions that have largely improved the manuscript. This research made use of the data from the Milky Way Imaging Scroll Painting (MWISP) project, which is a multiline survey in $^{12}\text{CO}/^{13}\text{CO}/\text{C}^{18}\text{O}$ along the northern Galactic plane with the PMO 13.7 m telescope. We are grateful to all the members of the MWISP working group, particularly the staff members at the PMO 13.7m telescope, for their long-term support. MWISP was sponsored by the National Key R&D Program of China with grants 2023YFA160800, 2017YFA0402701, and the CAS Key Research Program of Frontier Sciences with grant QYZDJ-SSW-SLH047. This work is supported by NSFC grants 12173090, 12073079. X. Chen acknowledges the support by the CAS International Cooperation Program (grant No. 114332KYSB20190009). This work also made use of data from the European Space Agency (ESA) mission Gaia (<https://www.cosmos.esa.int/gaia>), processed by the Gaia Data Processing and Analysis Consortium (DPAC, <https://www.cosmos.esa.int/web/gaia/dpac/consortium>). Funding for the DPAC has been provided by national institutions, in particular the institutions participating in the Gaia Multilateral Agreement.

Facilities: PMO-13.7 m telescope, Gaia space telescope

Software: astropy (Astropy Collaboration et al. 2013, 2018, 2022), scikit-learn (Pedregosa et al. 2011), emcee (Foreman-Mackey et al. 2013), Pymc3 (Salvatier et al. 2016), Matplotlib (Hunter 2007).

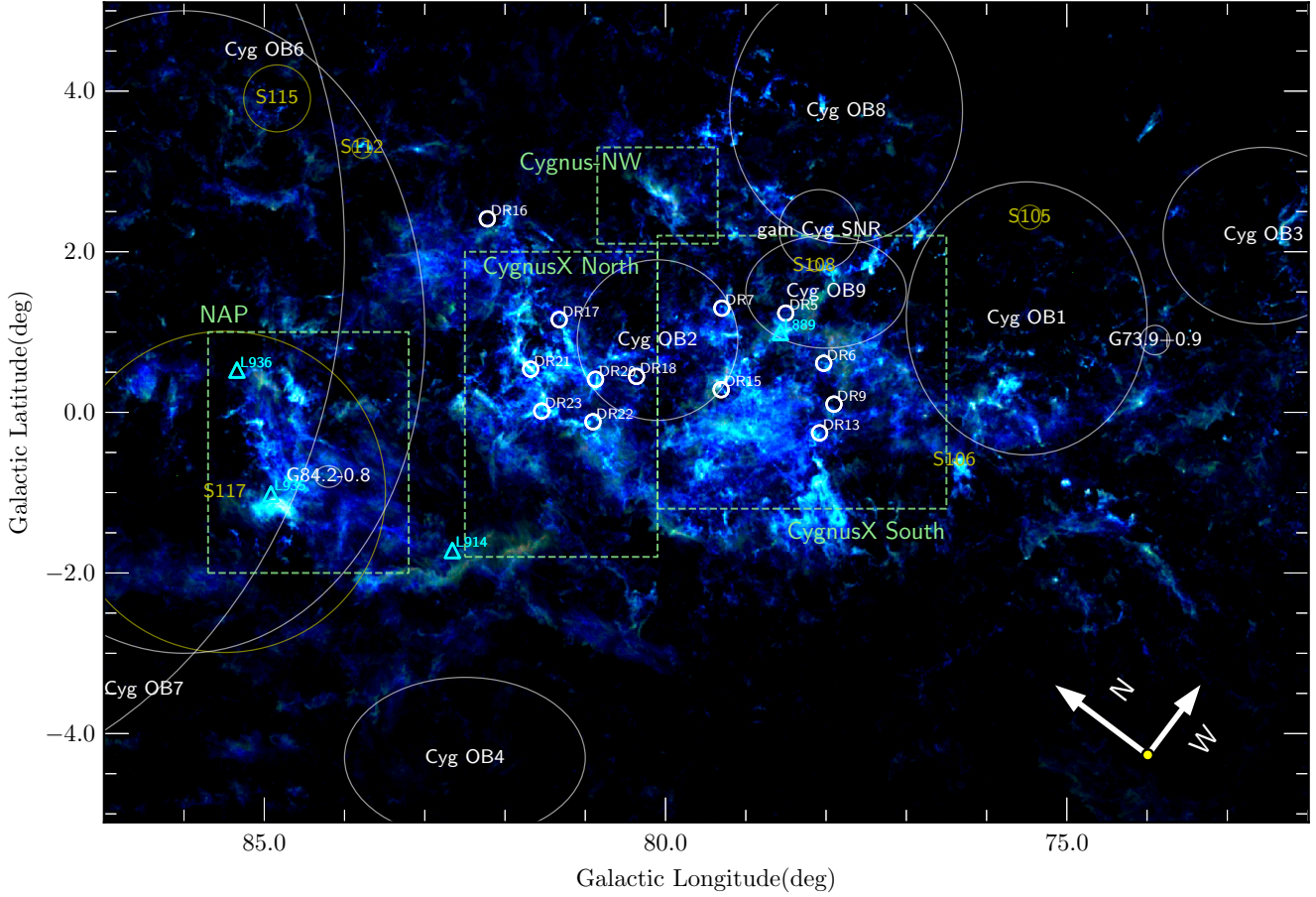


Figure 1. A composite guide map colored in R (C¹⁸O), G (¹³CO), B (¹²CO) based on the MWISP data. The map is made by moment masking method. That is, pixels with three continuous channels beyond three times of the noise level have been kept. Many prominent structures are denoted on this map, including OB associations and SNR γ Cygni (labeled with large circles or ellipses), dark clouds (triangles), and radio sources collected by Downes & Rinehart (1966)(white small circles), as well as several HII regions (yellow circles). The light green rectangles indicate some interesting sub-regions discussed in Section 5.

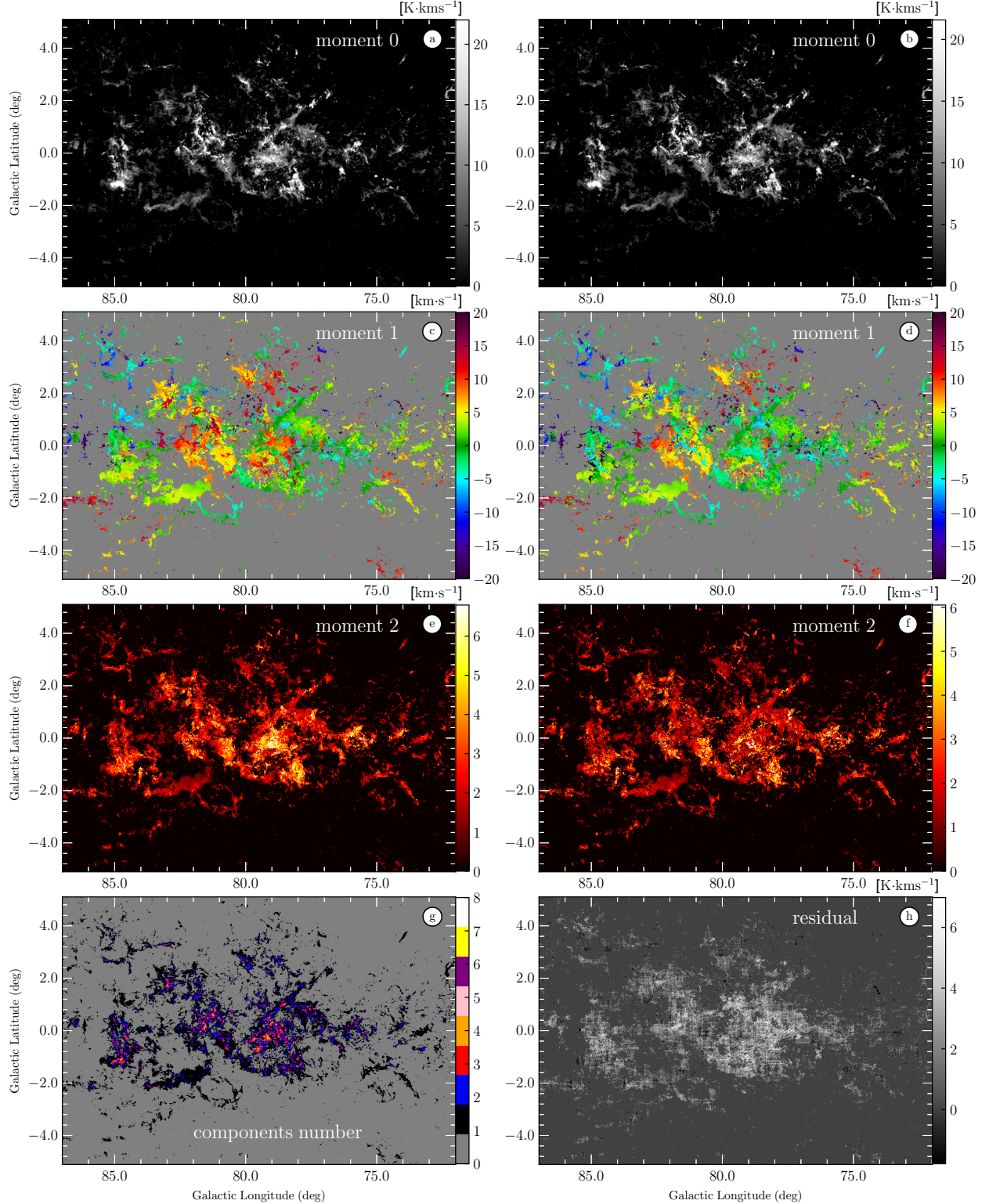


Figure 2. (a) Reconstruction of moment 0 map of ^{13}CO emission, the values in grey scale are fluxes summed up by all Gaussian components in each sight line. (b) Similar to (a), but only for the emission with Gaussian components after clustering. (c) Reconstruction of moment 1 map, showing the centroid velocity of Gaussian components. We choose most positive velocities on the top (top positive), but not a weighted average. (d) The same with (c), but smallest velocities on the top (top minus). (e) The moment2 map, showing the line width of most positive velocities on the top. (f) The same with (e), but smallest velocities on the top. (g) The distribution of the number of Gaussian components in the whole region. And (h) the residuals between integrated emission of raw data and reconstructed image by Gaussian decomposition.

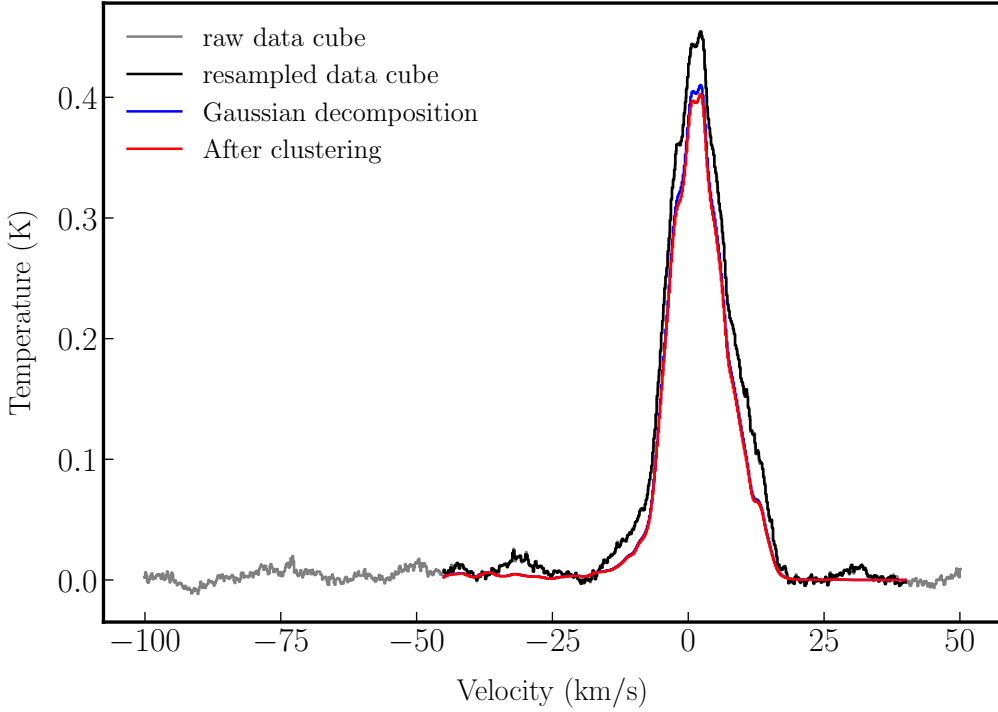


Figure 3. The average spectrum of ^{13}CO toward the Cygnus region. Grey line shows the raw data truncated from $-100 \text{ km} \cdot \text{s}^{-1}$ to $50 \text{ km} \cdot \text{s}^{-1}$, while black line denotes the average spectrum after resampling. Blue curve indicates the average of all signals restored by Gaussian decomposition, while red line shows the average spectrum after clustering based on ACORNS (Henshaw et al. 2019). Toward the Cygnus region, we note that a collective cloud emission overlapped together within a narrow velocity range ($-20 \text{ km} \cdot \text{s}^{-1}$ to $20 \text{ km} \cdot \text{s}^{-1}$). The flux reconstructed by Gaussian decomposition and clustering are 81.5% and 79.5% (see Section 3.3), respectively.

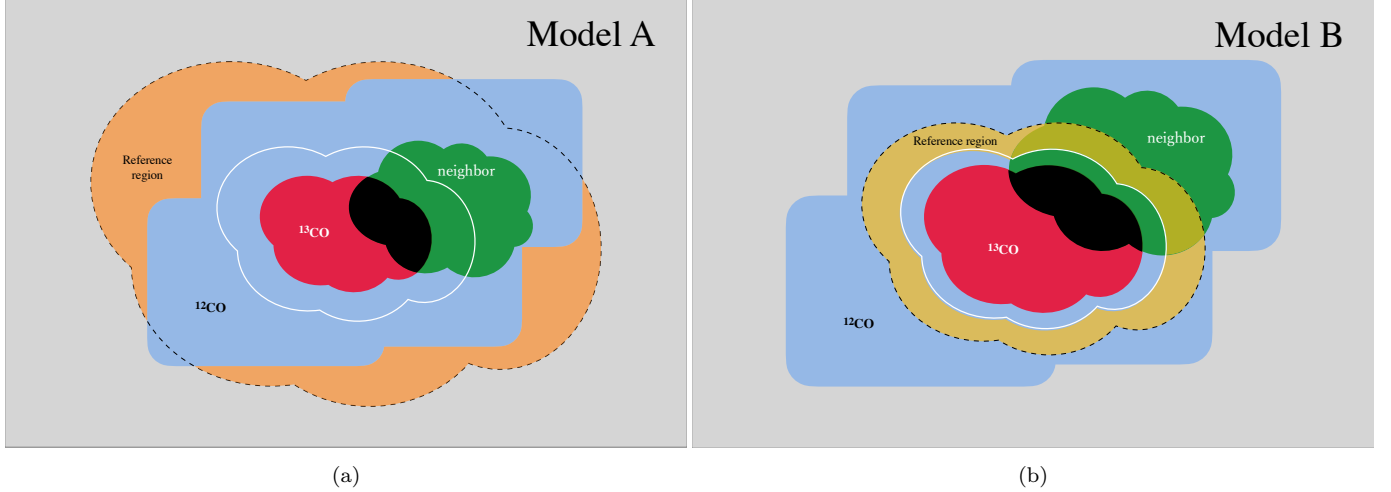


Figure 4. The sketches illuminate our method based on BEEP (Yan et al. 2019a). On-sources are selected within the ^{13}CO structure. (a) Use ^{12}CO emission to choose field stars. (b) Use ^{13}CO its own morphology to select field stars in its periphery. Red region is the identified ^{13}CO cloud, which is partly overlapped by a neighboring cloud in green. The black part is the region with superposition, which include more than one Gaussian components. White solid contour and black dashed contour denote different dilation of cloud boundary. Orange part represents the reference region. Blue area represents the widespread ^{12}CO emission. Obviously Model A considers the ^{12}CO free region as the reference region, while Model B refers to ^{13}CO morphology to select the reference stars (see Section 4.1.2).

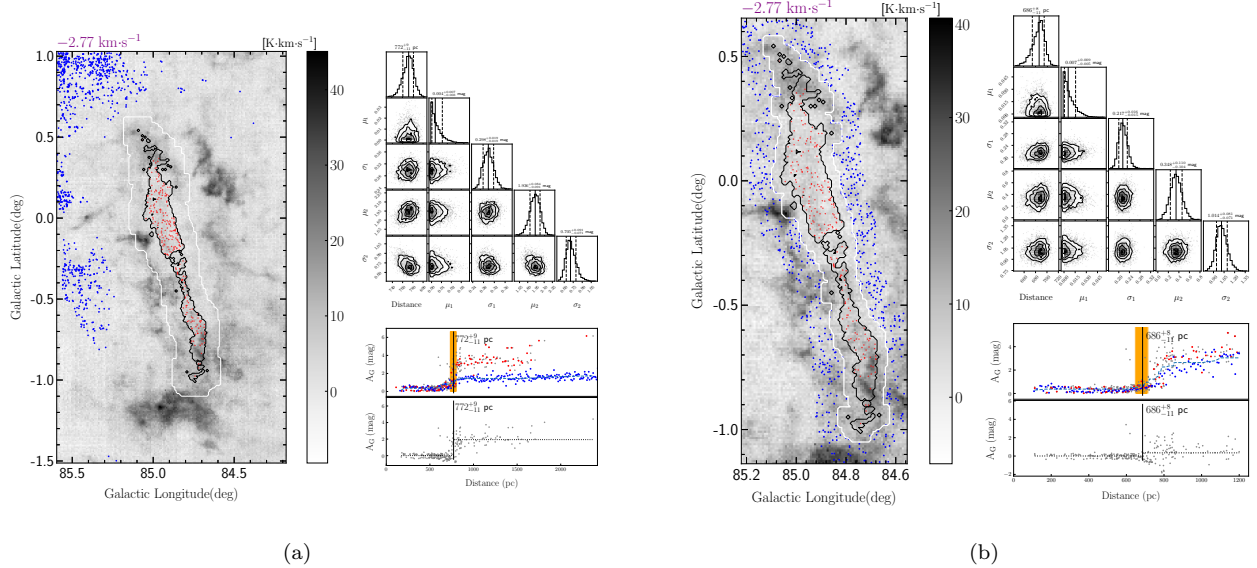


Figure 5. The distance measurement of cloud G084.88-0.20 (id 185 in Table 1) from Model A and B. The Grey scale map in the left side presents the ^{13}CO integrated intensity of the cloud and its neighbours. Black contour plot the MC structure identified with ACORNS based on the Gaussian decomposition, while white contour expand the MC structure boundary with 5 arcmin. All on-cloud stars locate within the cloud are marked as red dots, while referenced stars (blue dots) are chosen out of white contour, see details in Figure 4. Corner Plot in the upper right gives the MCMC sampling results from emcee. We set 3 parameters in our model, nwalker=50, the number of burn-in samples for Markov chain with 1000, and steps with 2000. All binary relations among parameters are presented as 2-d Gaussian distributions. We compute median value (solid line) of all samples for result, and 1σ confidence interval in dashed lines (16-th and 84-th percentile). Subplot in the lower right presents an A_G -Distance relation for on-cloud stars. The upper one gives A_G values before baseline elimination, while the lower one gives the result by subtracting a monotonous fitting of reference stars (see Section 4.2.2). Grey dots are raw data from Gaia DR3, while red and blue dots are binned values in a 10 pc interval for on-cloud and off-cloud stars, respectively. Orange vertical lines denote all the jump points in MCMC sampling. Model A give a significant jump, and it matches better with distances in literature of NAP region.

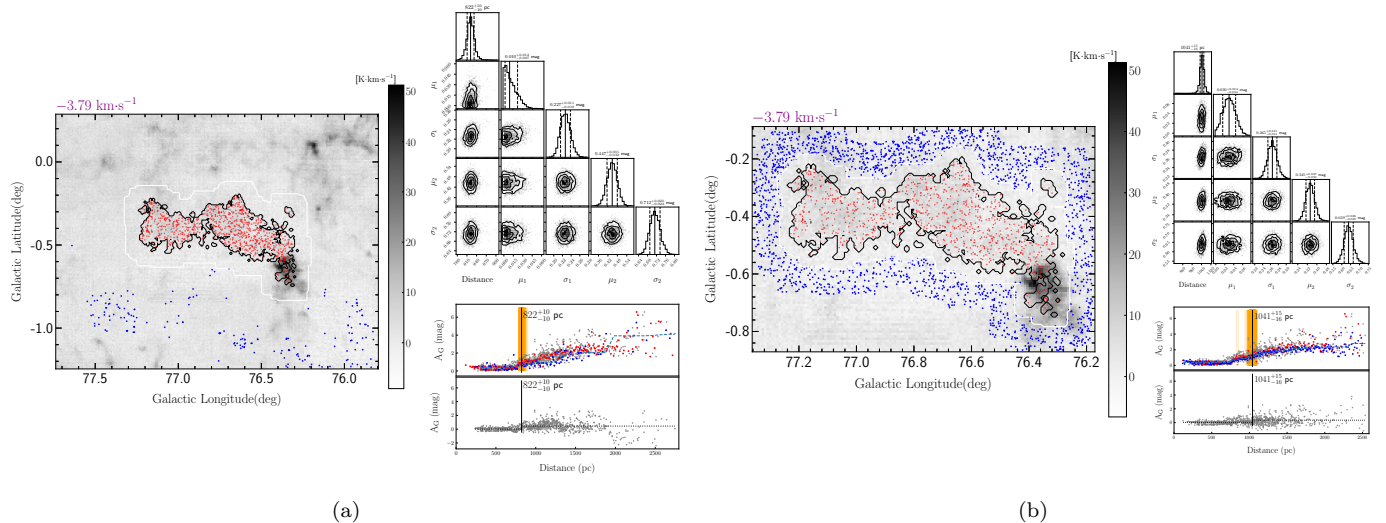


Figure 6. The same as Figure 5, but for cloud G76.74-0.43 (id 30 in Table 1). The fluctuation of A_G -Distance relation for on-cloud stars for Model A denotes worse baseline fitting. We thus choose the result from Model B (see Section 4.2.2).

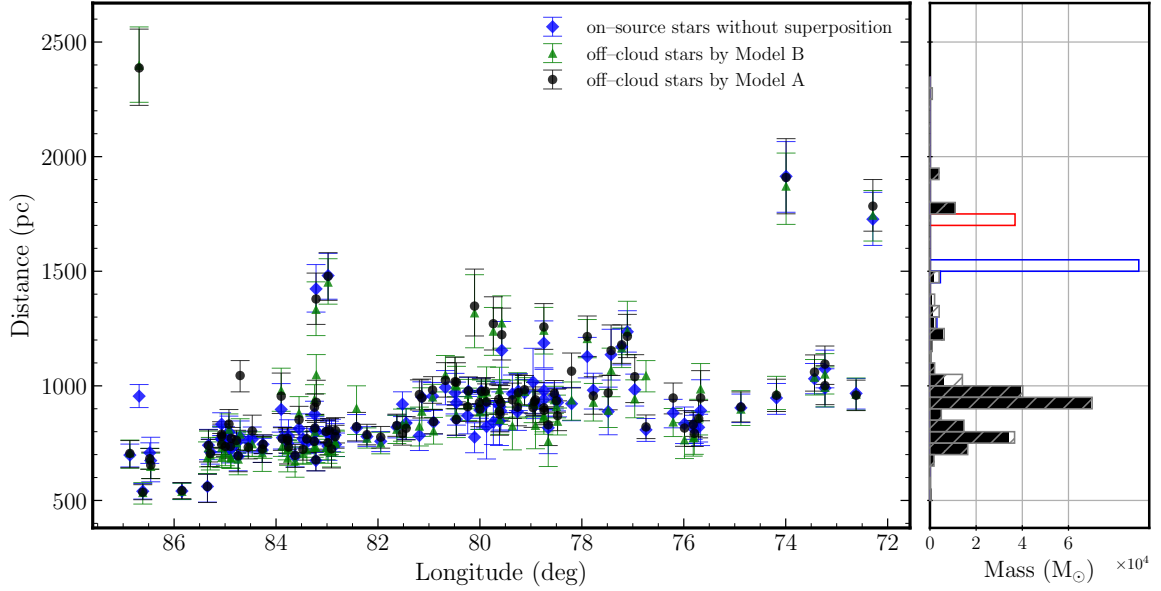


Figure 7. Left panel: Our results for 120 robust distance measurements both in Model A and B (class I, see details in Section 4.3). We find that all differences between Model A and Model B are smaller than 150 pc, except cloud G76.74-0.43 (id 30 in Table 1). Right panel: LTE Mass statistics based on our cloud catalogue, i.e. black histogram from samples of class I in Table 1, grey histogram with slashes included class II results from Table 1, while blue and red histograms from Tables 2 and 3.

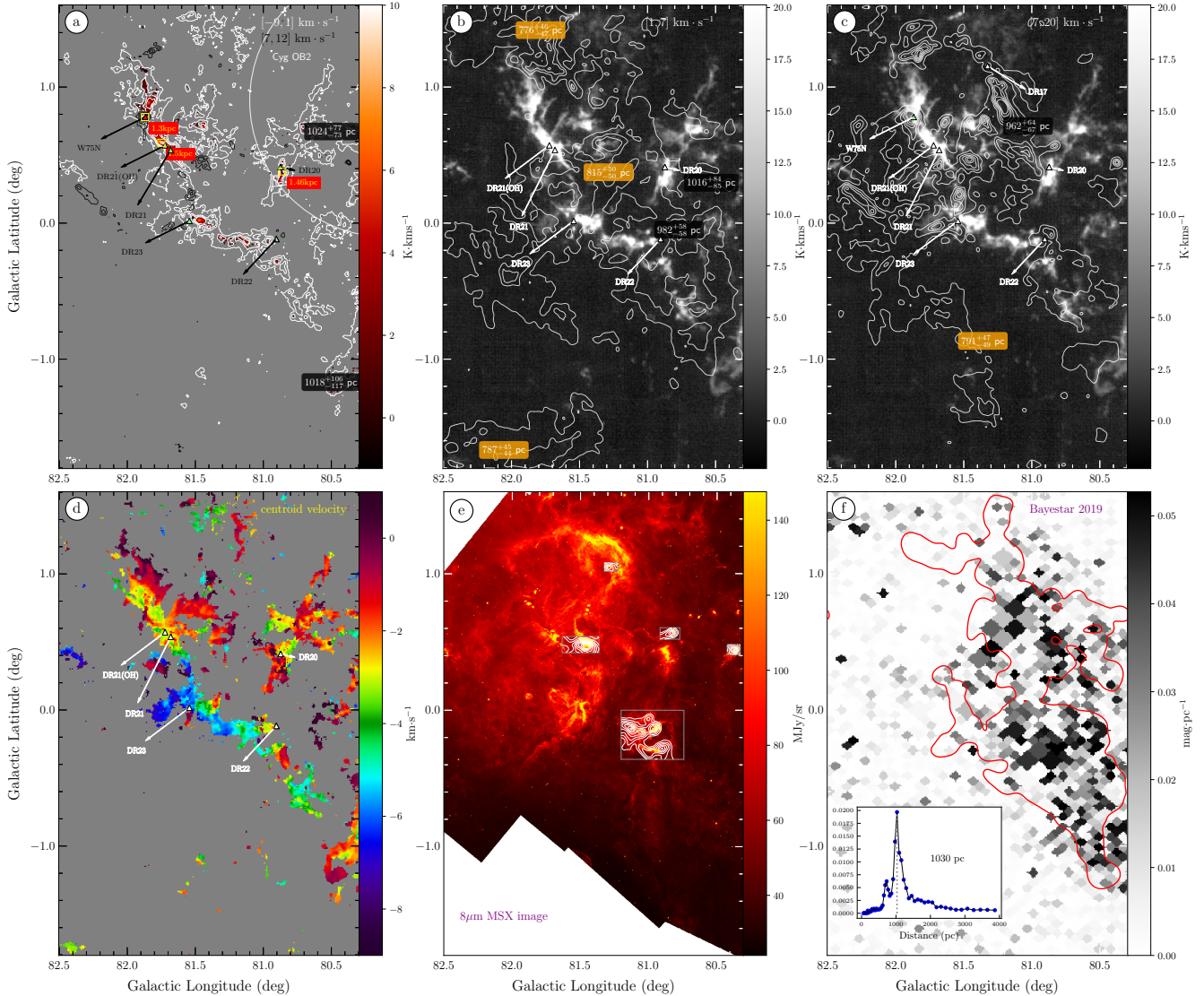


Figure 8. Subplots for the Cygnus X North region. Panel (a) shows ^{13}CO (white contours in $[5, 20, 35, 50] \times \sigma$, σ is the noise level of intensity map) and C^{18}O (colormap) emission in $[-9, 1] \text{ km} \cdot \text{s}^{-1}$. Massive star-forming regions are sited along the dense filamentary structure, i.e. DR21, DR23 and DR22. Black contours also denote the dense molecular gas in $[7, 12] \text{ km} \cdot \text{s}^{-1}$ in same levels, e.g. W 75N is overlapped on the DR21 filament. Some HII regions are marked with triangles. The extent of Cygnus OB2 is plotted in a white circle. Distances with 5% system error of our measured clouds and those from masers are presented, different gas layers are also labeled with different colors. Panel (b): The grey scale map is ^{13}CO emission from velocity interval of $[-9, 1] \text{ km} \cdot \text{s}^{-1}$, overlaid with smoothed data from $[1, 7] \text{ km} \cdot \text{s}^{-1}$ (white contours in $[2, 6, 10, 14, 18, 22] \text{ K} \cdot \text{km s}^{-1}$). Panel (c): All the same with Panel (b), but contours for velocities in $[7, 20] \text{ km} \cdot \text{s}^{-1}$. Panel (d): A moment 1 map of centroid velocities extracted from Gaussian decomposition for clouds in $[-9, 1] \text{ km} \cdot \text{s}^{-1}$. Obviously, prominent velocity gradient along filamentary structure can be seen. Panel (e): An 8 μm MSX image toward the Cygnus X North region. Grey edged rectangles mark the identified molecular cloud with the associated mid-IR features. The extent of these rectangles is derived from the $\pm 3\sigma$ of v, l, b relative to cloud center in Table 3. Panel (f): A 1030 pc slice of 3D dust map from Bayestar 2019 (Green et al. 2019), overlaid with the 1 kpc MC layer (red contours) from our samples (class I in Table 1) with well determined distances. Note that our results are in good agreement with Green et al. (2019).

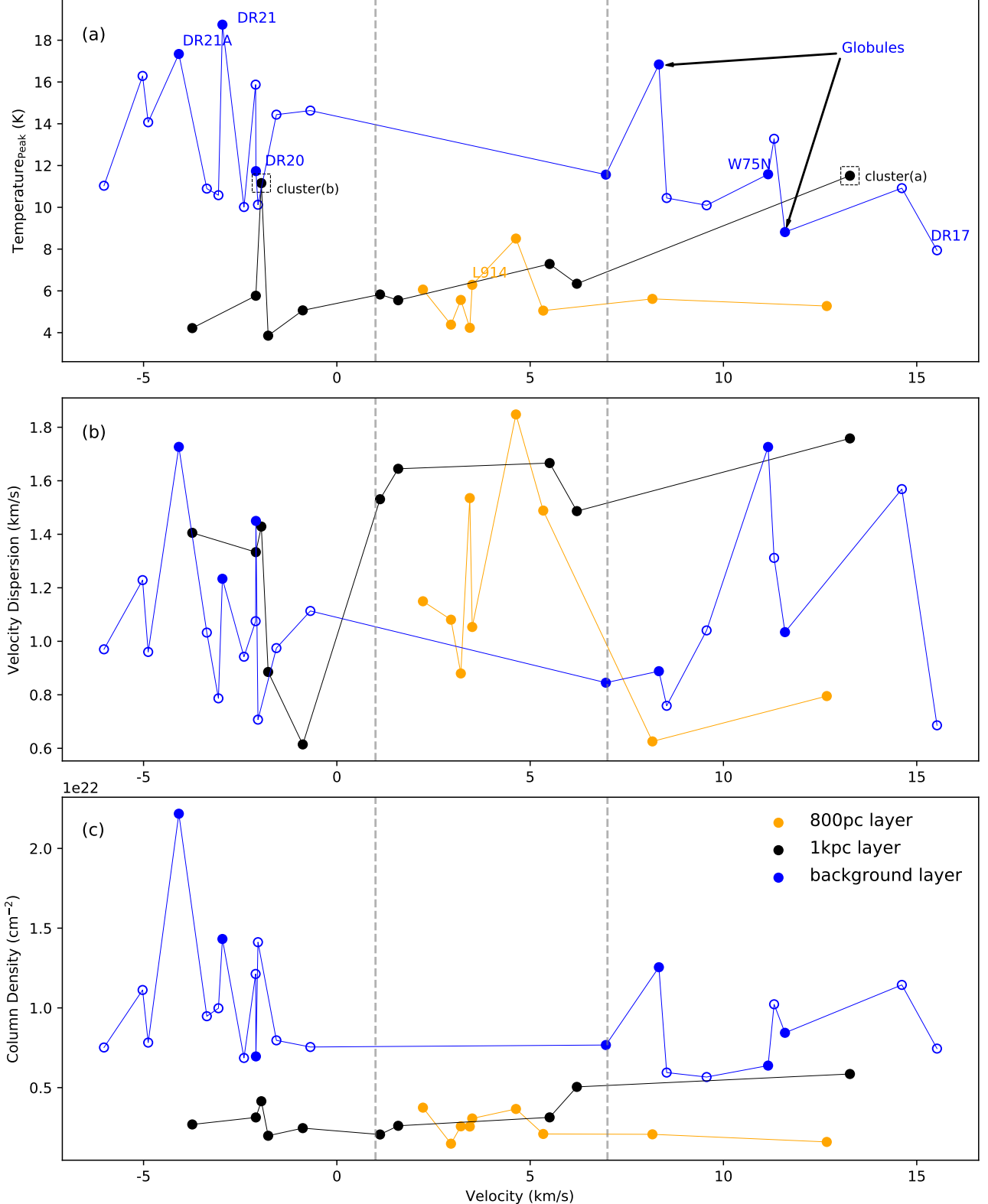


Figure 9. Physical properties of clouds in the Cygnus X North region. Panel (a): ^{13}CO peak temperature of MCs. Different colors are marked for clouds in different layers. Clouds in background layer are associated with masers or bright cometary mid-IR features (filled blue dots) and the nearby dense gas structures (empty dots) along the filamentary structure of Cygnus X North star-forming region. Panel (b) and (c), the same with Panel (a), but for velocity dispersion and column densities of the MCs.

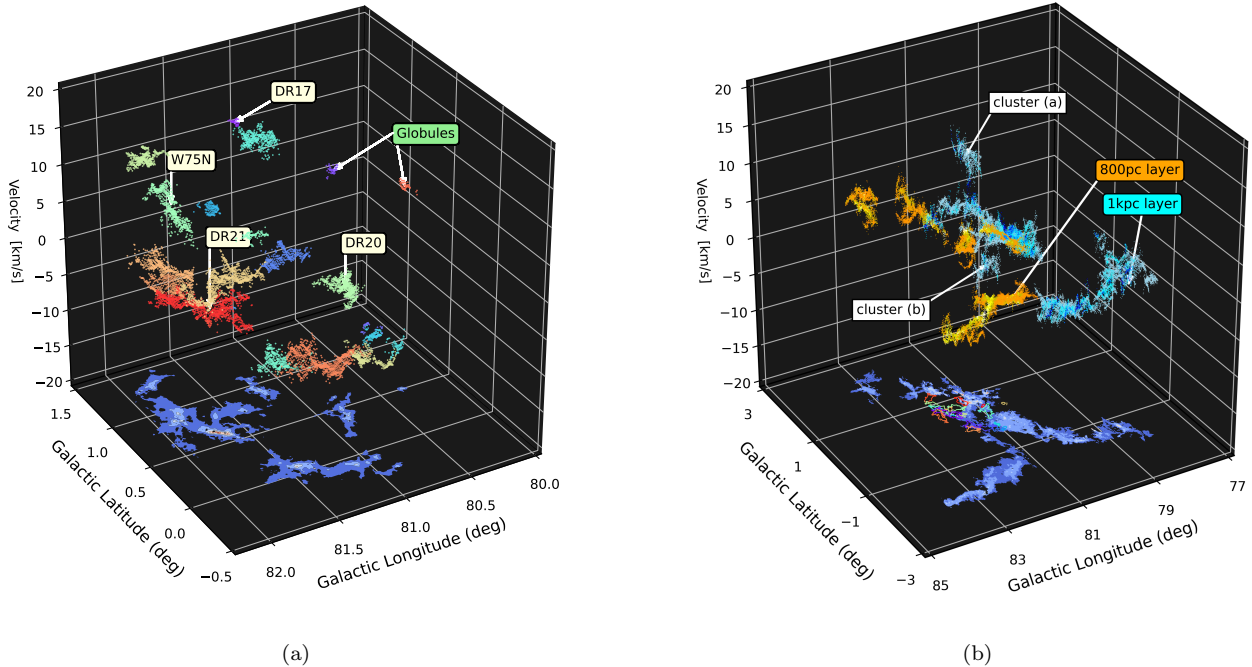


Figure 10. 3D plot of different gas layers toward the Cygnus X North region. Panel (a): Scatter plot of clouds in background layer (i.e., 1.3~1.7 kpc). Colors mark different ^{13}CO structures identified by ACORNS and each dots present pixel by pixel centroid velocities. Their summed intensities are projected at the bottom. Panel (b): Scatter plot of clouds in 800 and 1 kpc layers. Clouds in 800 pc are in orange, while clouds in 1 kpc are in cyan. Both of the two layers display large filamentary complexes overlapped together. Clouds in 1.3~1.7 kpc layer are also plotted as colored contours on the bottom, which shows the spatial relation of different clouds on projection.

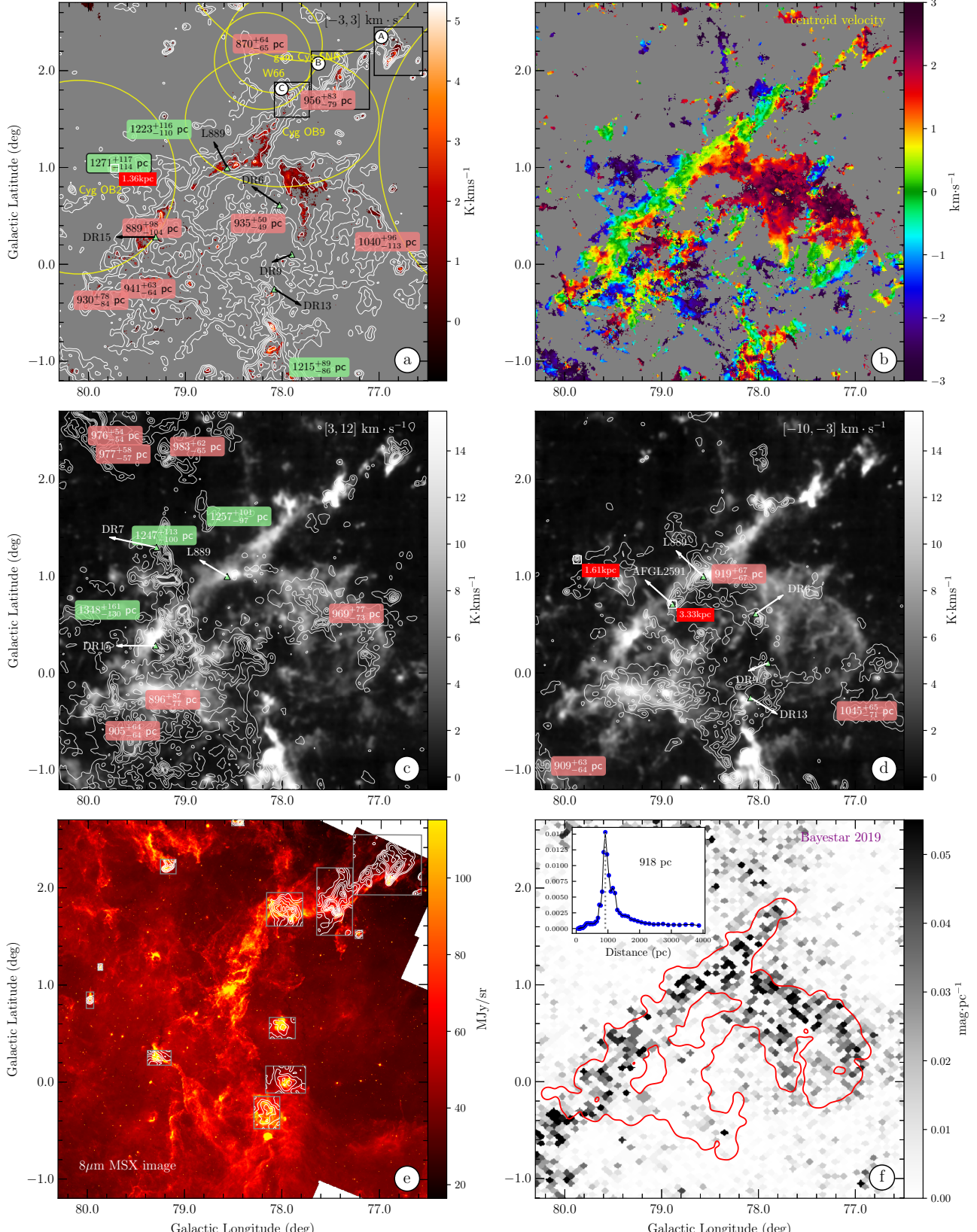


Figure 11. Subplots toward the Cygnus X South region. Panel (a): ^{13}CO (white contours in $[5, 10, 20, 35, 50, 70] \times \sigma$, σ is the noise level of intensity map) and C^{18}O (colormap) emission in $[-3, 3] \text{ km} \cdot \text{s}^{-1}$. These HII regions and dense cores of L889 are marked with triangles. The extent of OB associations and SNRs are plotted in yellow ellipses. Distances (with 5% system error) of our measured clouds and those from masers are also presented. Panel (b): Moment 1 map in $[-3, 3] \text{ km} \cdot \text{s}^{-1}$. Panel (c): The grey scale map is ^{13}CO emission from $[-3, 3] \text{ km} \cdot \text{s}^{-1}$, overlaid with smoothed data from $[3, 12] \text{ km} \cdot \text{s}^{-1}$ with levels $[10, 25, 40, 55, 70, 85] \times \sigma$. Panel (d): All the same with Panel (c), but contours for velocities in $[-10, -3] \text{ km} \cdot \text{s}^{-1}$. Panel (e): Same with Figure 8e, but for Cygnus X South region. Panel (f): A 918 pc slice of 3D dust map from Bayestar 2019 (Green et al. 2019), overlaid with L889 cloud at ~ 935 pc (red contour) from our samples (see cloud 57 in Table 1).

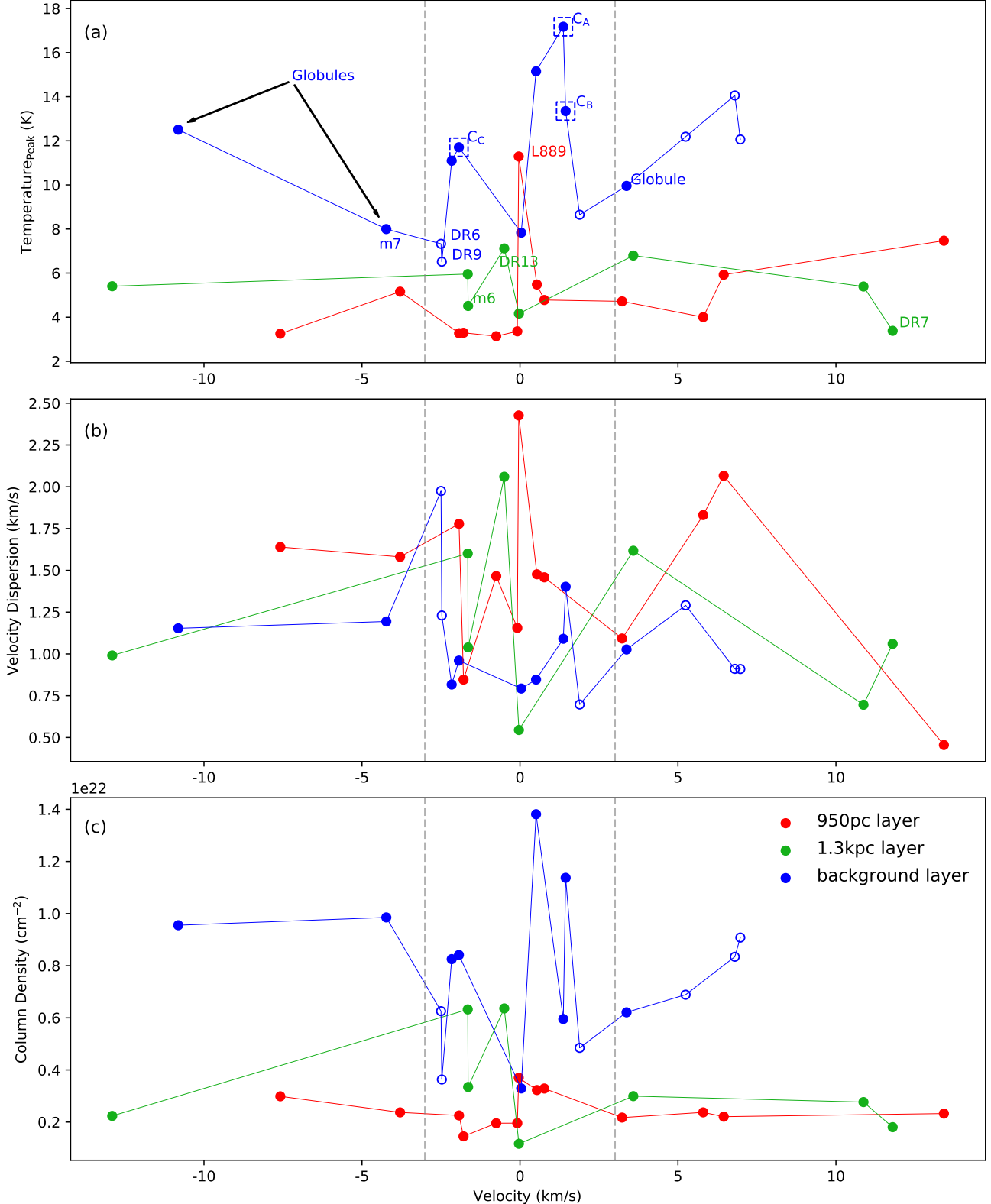


Figure 12. Physical properties of clouds in the Cygnus X South region. Panel (a): ^{13}CO peak temperature of MCs. Different colors are marked for clouds in different gas layers. Clouds in background layer (blue dots) are all associated with bright mid-IR features. Clouds in filled dots have cometary or globular morphology, which is a strong evidence been shaped by massive OB star groups, e.g., cloud A, B marked by Schneider et al. (2006), while clouds in empty dots are oval-shaped or irregular, e.g. DR6 and DR9. Panel (b) and (c): The same with Panel (a), but show velocity dispersion and column densities of the clouds.

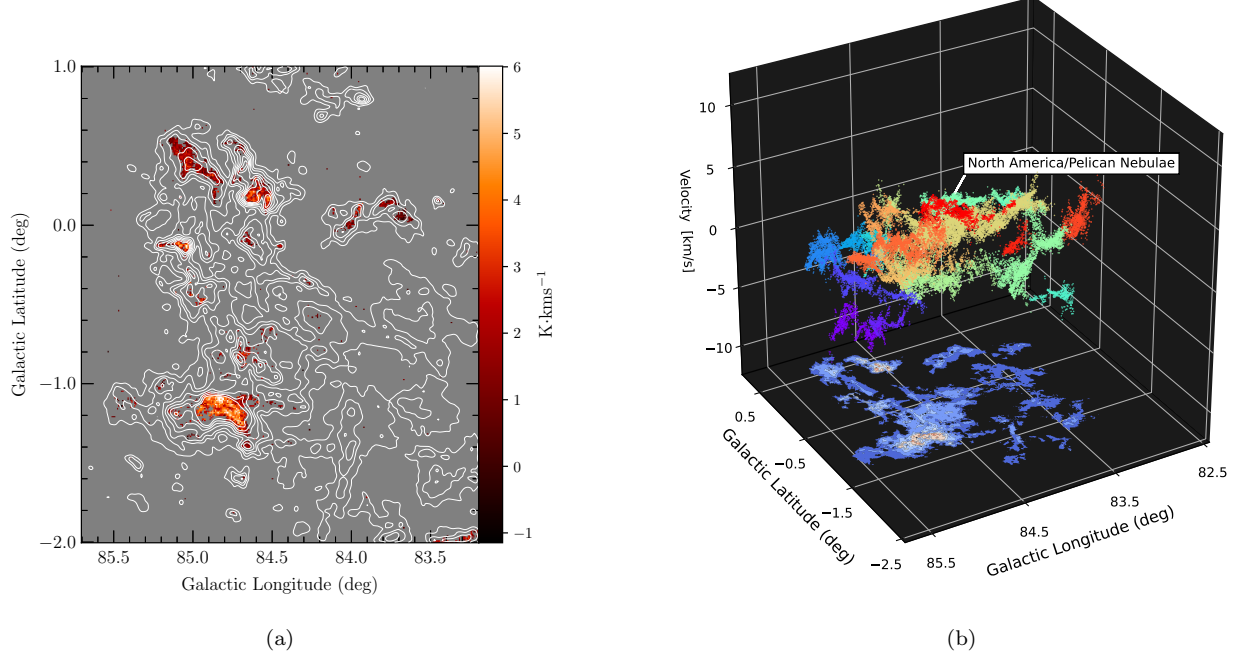


Figure 13. Panel (a): ^{13}CO (White contours in $[10, 20, 30, 45, 60, 75, 90] \times \sigma$, σ is the noise level of intensity map) and C^{18}O (colormap) emission in $[-10, 10] \text{ km} \cdot \text{s}^{-1}$ toward the NAP region. Panel (b): A 3D plot for all ^{13}CO structures with measured distances in the region.

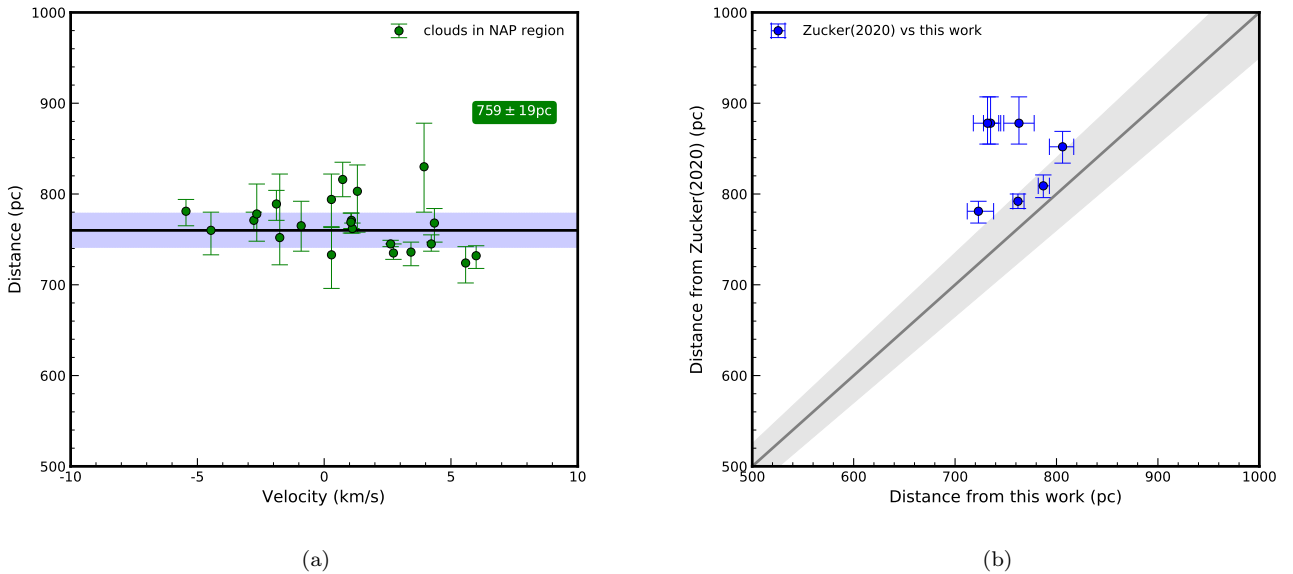


Figure 14. Panel (a): Measured distances of different ^{13}CO structures toward the NAP region. Black line and blue shadow show the averaged distance and dispersion (without the 5% system error) weighted by clouds masses. Panel (b): Distances compare to [Zucker et al. \(2020\)](#) with labeled 5% system error (grey shadow) relative to distance, a systematic deviation can be found (see details in 4.3.3).

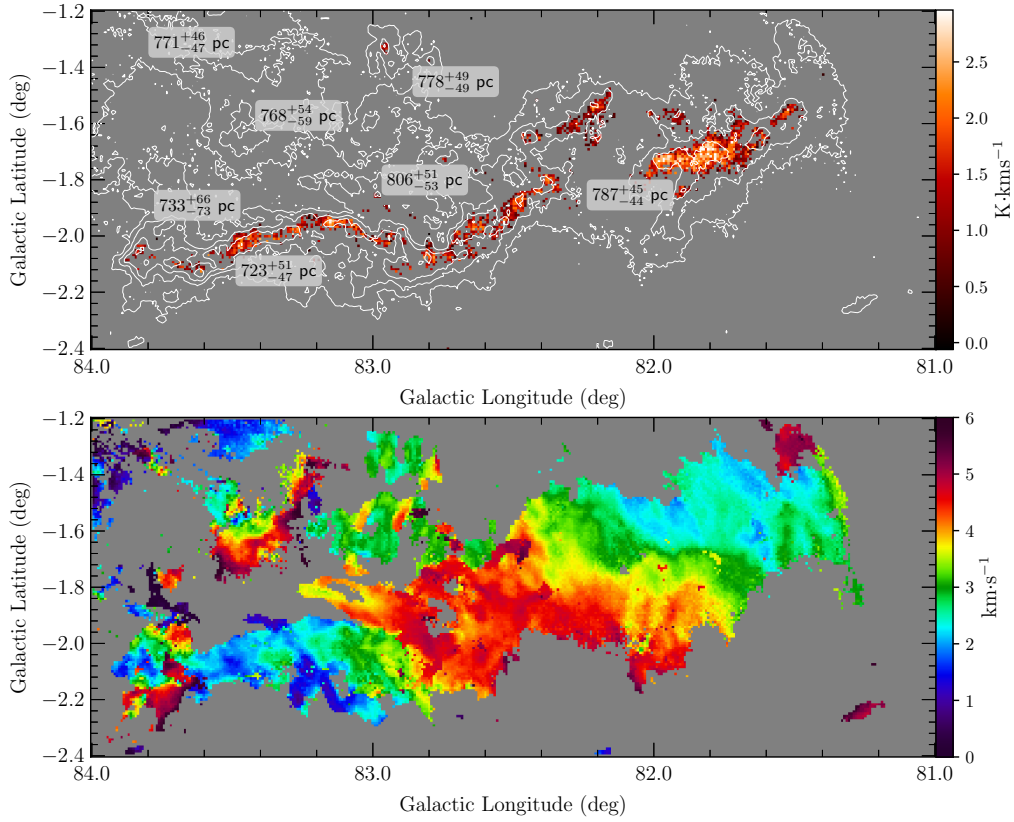


Figure 15. Upper panel: ^{13}CO (white contours in $[5, 15, 25, 35, 45, 55] \times \sigma$, σ is the noise level of intensity map) and C^{18}O emission (colormap) in $[0, 6] \text{ km} \cdot \text{s}^{-1}$ toward L914. 5% system error of the distances is labeled for identified ^{13}CO structures. Lower Panel: Moment 1 map of centroid velocities extracted from Gaussian decomposition for the above velocity interval.

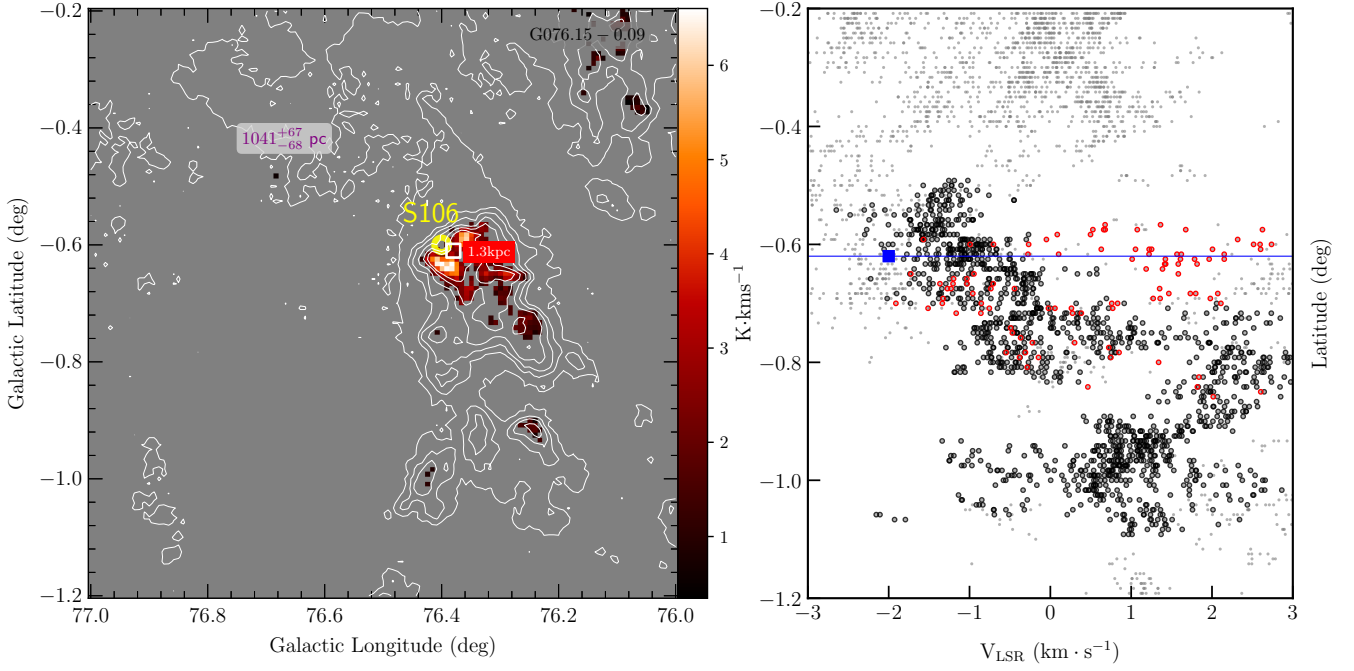


Figure 16. Left panel: ^{13}CO (white contours in $[5, 15, 25, 35, 45, 55] \times \sigma$, σ is the noise level of intensity map) and C^{18}O emission (colormap) in $[-3, 3] \text{ km} \cdot \text{s}^{-1}$ toward S106. 5% system error of the distances is labeled for identified ^{13}CO structures. The location of HII region (yellow circle) and maser (white box) are also labeled on the map. Right Panel: The different velocity structures labeled in black and red dots in the velocity-latitude coordinates from Gaussian decomposition (see details in Section 5.5). The blue square with error represents the observed maser from Xu et al. (2013).

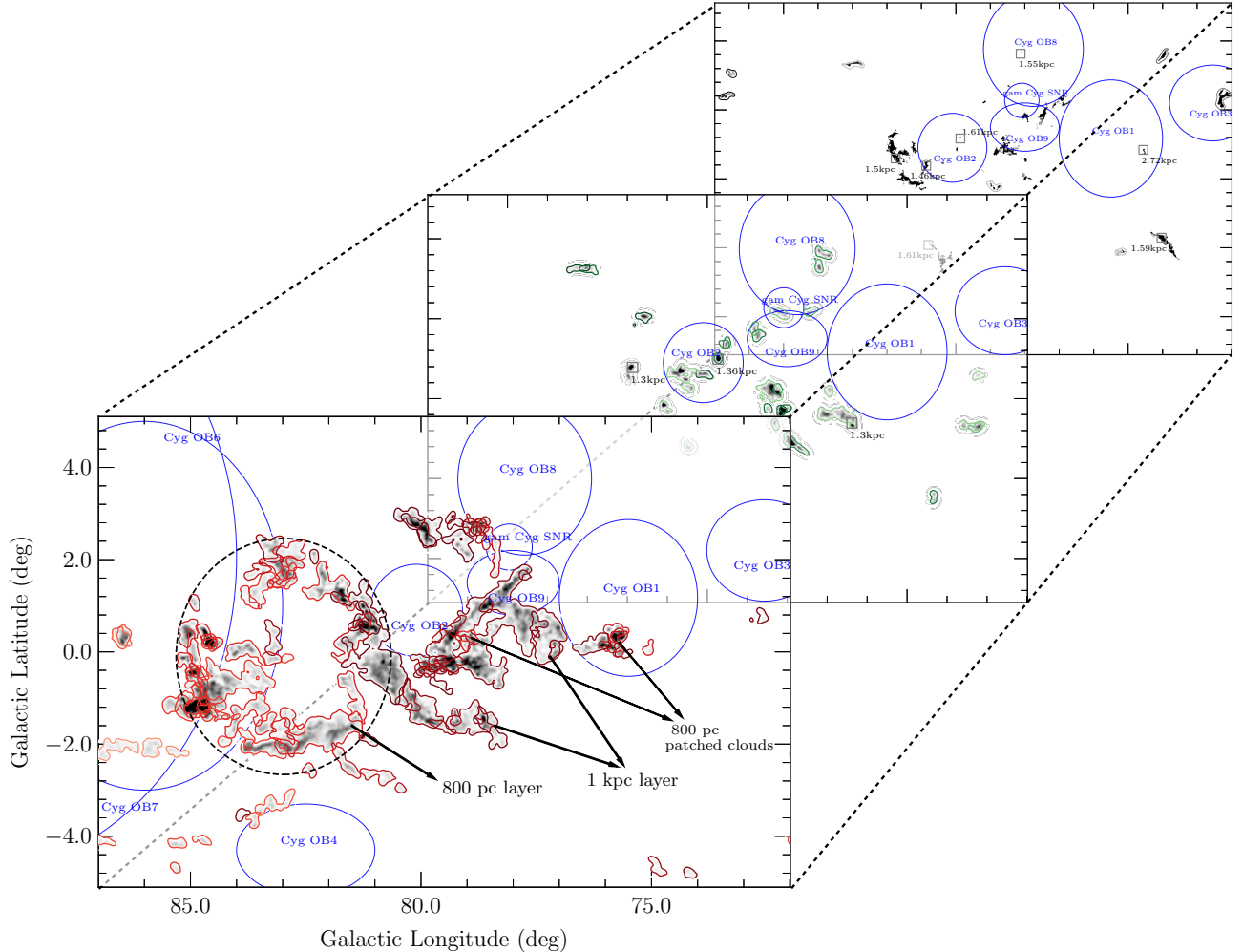


Figure 17. Big picture of multiple gas layers toward the Cygnus region. We divide clouds with distance measurement (see Tables 1, 2 and 3) into three intervals: [500, 1000] pc in red, [1000, 1400] pc in green, and [1400, 3000] pc in black. Lighter contours indicate nearer distance for each layer, while the darker show the further distances. Grey scale maps are reconstructed by identified clouds from ACORNS, while their boundaries are delineated using a low-pass filtering method (*butterworth* in Python). The dashed ellipse shows a large scale molecular loop with diameter of ~ 56 pc at a distance of 800 pc. Different layers are also annotated in the [500, 1000] pc map. Middle map includes two layers, the ≈ 1 kpc clouds in light green, and ~ 1.3 kpc clouds in green. Clouds in ≥ 1.4 kpc layer without contours are MCs associated with masers and/or mid-IR bright features in Tables 2 and 3. 7 clouds in Table 1 are successfully measured in this layer. Blue ellipses show OB associations and SNR, while boxes show the masers in Table 2.

APPENDIX

A. COHERENCE OF IDENTIFIED LARGE STRUCTURES

The large-size MC structures traced by ^{13}CO usually display hierarchical and spatially extended structure (see details in Section 3.1 and 3.2). See Figure A1a for an example, this large cloud at 982 pc (see cloud 118 in Table 1 and Figure A1b) spanning two degrees along latitude, probably suffers different extinction environment.

We choose sub-regions along different LOS to measure their distances to check whether the substructures belong to a physical cloud. Firstly, the 225 arcmin 2 boxes were chosen along the structure to cover various sub-regions as well as enough on-cloud stars. Alternatively we took the secondary trunks in the hierarchy provided by ACORNS to include on-cloud stars. Using the same field stars for reference, we implement Model A the same way to derive their distances (blue squares for the boxes samples and green triangles for the trunks in Figure A1c).

We find that the measured distance of the whole cloud is consistent with the mean value of distances of every small parts (see Figure A1bc). It indicates that the whole structure identified by our method does not suffer from significant contamination of unrelated emission at different distances. Similar results can also be found toward other large scale structures, e.g. Figure A2. We suggest the large scale structures identified by the ^{13}CO emission are at similar distances.

Some sub-regions probably tends to be contaminated by other different MC structures along LOS (see the left three samples in Figure A1c). These small substructures in the east side are measured to be nearer (i.e. ~ 800 pc). We find that these sub-regions are just located at the overlapping regions of 800 pc and 1 kpc gas layers of the Cygnus X North (see Figure A1d and details in Section 5.1). Our further study with multi-jump detection model (in preparation) indeed shows that two layers of molecular gas are overlapped in the direction, i.e. ~ 800 pc and ~ 1 kpc gas in the east side of the cloud.

For another case of L889 cloud (Figure A2), deviation of distance measurements in individual regions likely indicate the contamination from further 1.3 kpc layer and foreground emission (see Figure A2d and details in Section 5.2). The above discussions tell us that the overlapping between different identified structures may lead to deviations of distance measurements for sub-regions of a cloud.

B. COMPARISON FOR DIFFERENT ON-CLOUD STARS SELECTION AND MCMC SAMPLING MODULES

All on-cloud stars versus stars after removing overlapping regions: We test the influence of different on-cloud star samples on measured distances by Model A (see Figure B1). In this work, we adopt all stars within cloud boundary identified by ^{13}CO as on-cloud stars (see Section 4.1.1). Alternatively, we also exclude stars in the overlapping region. That is, we reject stars in black area, and keep those in red area in Figure 4a.

We find that both of on-cloud star samples generally give consistent measurements relative to their uncertainties. Distances from overlap-removed stars give an overall larger uncertainties due to fewer on source samples. Additionally, the samples based on overlap-removed stars will decrease the number of clouds with measured distance (29 cloud structures, about 16% in all Model A samples).

Emcee working on the mock data: Aiming to examine how does the *emcee* work on single-jump-point detection, mock data of extinction&distance of stars learning from the Cygnus region were randomly generated. In the simulation, the preset jump point (*Distance*) is randomly distributed in [500, 2000] pc, while stars samples are uniformly produced in [100, 2500] pc in number density 0.2 pc^{-1} . ΔA_G (i.e. $\mu_2 - \mu_1$) follows a truncated exponential distribution from 0.2 mag and a rate parameter of 0.5 mag. To simplify the simulation, we fix σ_1 (0.2 mag) and σ_2 (0.4 mag). Based on star samples toward the Cygnus region, the median error over distance and dispersion of errors are set to 0.1 and 0.06, respectively. And the mean error of A_G is set to 0.04 mag and dispersion of error of A_G is set to 0.04 mag. 200 groups of stars sample (see two examples in Figure B2) were produced.

We present deviations and uncertainties of distances derived from *emcee* in a relation with increasing ΔA_G (see Figure B3). Both the deviations from preset distance and the uncertainties from posterior distribution decrease with the increasing ΔA_G . Since the fitted background extinction is likely to be larger for Model B after background elimination, Model A gives a statistically better fit when they reveal the same jump. The deviations from most of samples ($\gtrsim 90\%$) are smaller than 150 pc, and the uncertainties and deviations are comparable at least in $\Delta A_G \geq 0.2$

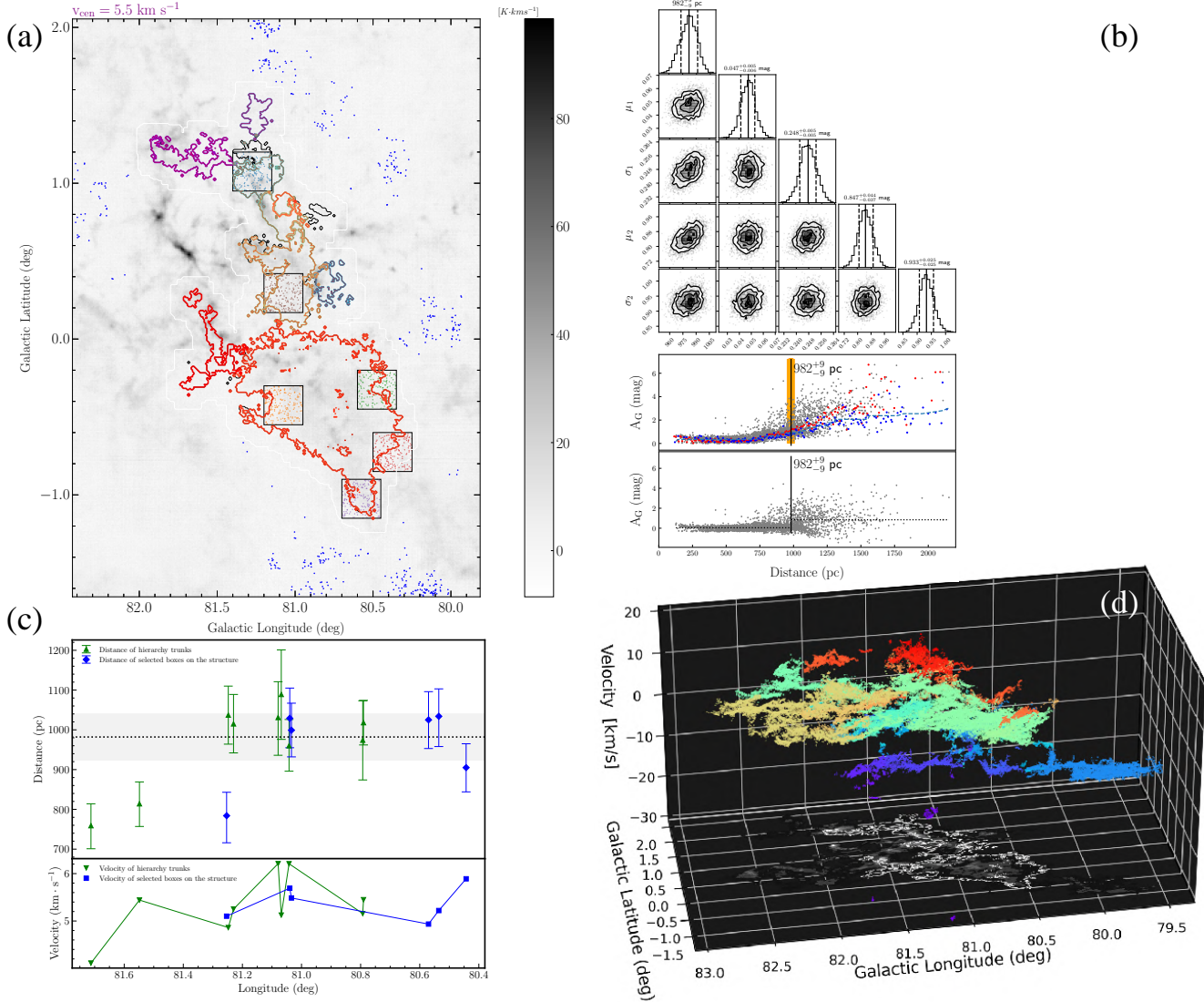


Figure A1. A validation of coherent structures (id 118 in Table 1) identified by ACORNS based on Gaussian decomposition. We chose substructures of the large MC structure by manually marked boxes and hierarchical trunks (colored contours). Their distances are marked by blue squares and green triangles, respectively, while their confidence intervals (added 5% system error of Gaia) are denoted by error bars. The 1σ confidence interval of distance is plotted in grey area of panel c. In lower right panel, it is a 3D PPV scatter plot of centroid velocities of the cloud. All structures (other colors) overlaid with the cloud (in green) along LOS are also drawn, showing coherent velocity structures in PPV space.

mag. These explain why almost all the samples have distance differences within 150 pc between two Models (A and B) when they detect the same jump point (see Section 4.2.2). It proves that in current uncertainties of Gaia DR3, the *emcee* module provides robust results to cloud distance measurement.

Comparison with different sampling modules (*emcee* versus *Pymc3*):

Pymc3 (Salvatier et al. 2016) module implicitly builds up a *Theano* function from the space of our parameters to their posterior probability density up to a constant factor. The probability distribution of A_G can be treated as a piecewise function. We use *SWITCH* function to describe parameters in different intervals. In sampling process, we use *Metropolis* sampler for jump point, and *NUTS* for other four parameters (see Section 4). After 1000 draws, the returned object *TRACE* including posterior predictive samples are generated from MCMC sampling. The median values from above sampling are chosen as our results.

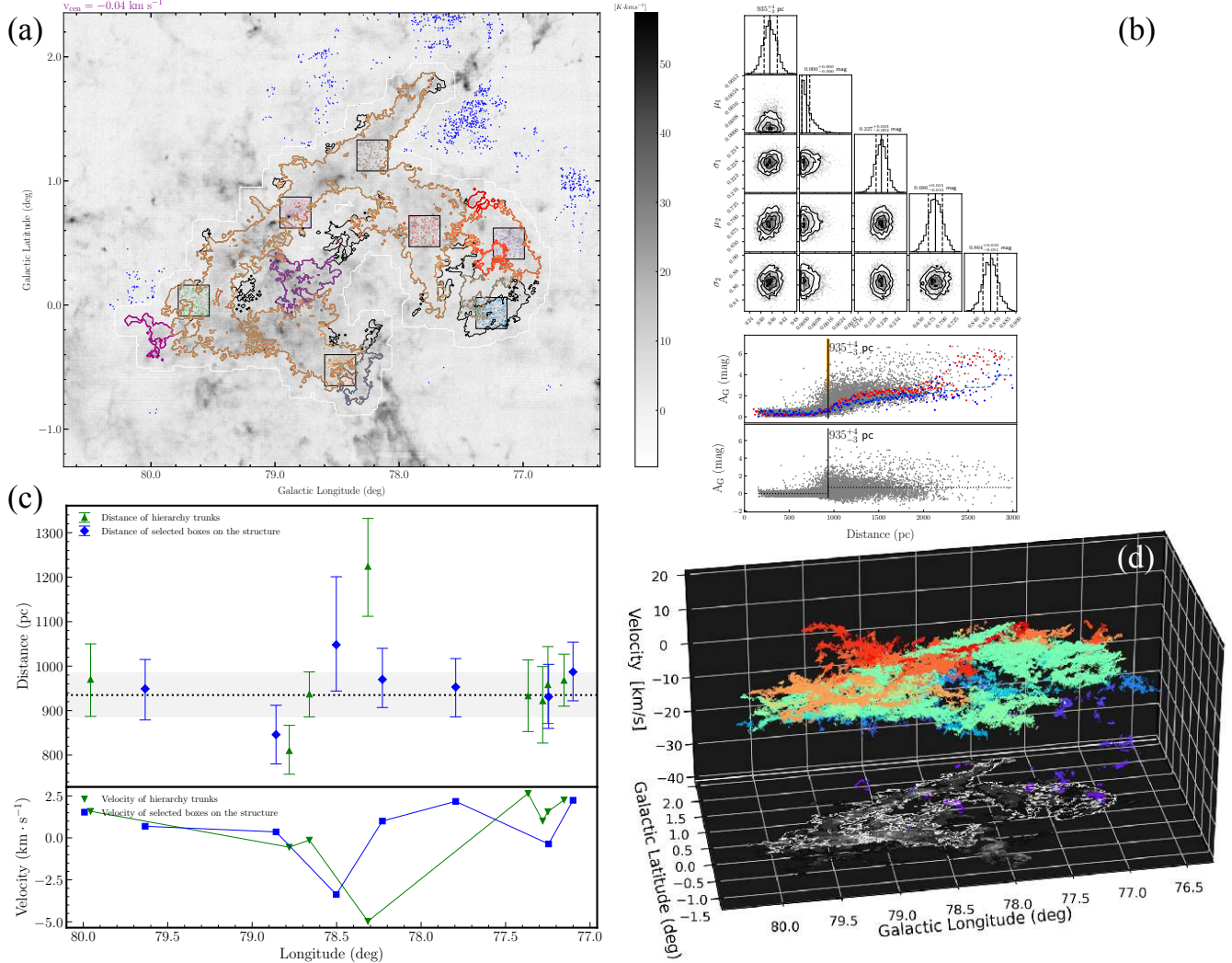


Figure A2. The same as Figure A1, but for MC L889 toward the Cygnus X South region.

In Figure B4a, we compare the distance measurement between *emcee* and *Pymc3* for clouds in Table 1. The distances by *emcee* are in good agreement with posterior predictive samples produced by *Pymc3*. However, large discrepancies can be seen for some cases ($\sim 10\%$).

Based on the 200 simulated samples (shown in Figure B4b), we find that *Pymc3* seems to work better than *emcee* on mock data. But the results from *Pymc3* match the mock data distances so closely with very small errorbars, even when the jumps are not clear enough. This is actually caused by overfitting. Some results from *Pymc3* are not robust due to deviating from preset distance out of uncertainties from sampling (see a case in blue box in Figure B4b). And a case detects multi-jump points (see red box in Figure B4b). Samplings from *Pymc3* are rather sensitive to small variations in A_G , and the detected jumps often deviate from true value (by *emcee* or human judge). We thus choose *emcee* because it gives a more robust sampling result in application to real data by considering baseline fluctuations and A_G dispersion uncertainties.

C. STAR DISTANCES ESTIMATED FROM PARALLAXES

In this work, we simply use MCMC sampling from parallaxes of stars to estimate their distances. In comparison, we follow the method of Bailer-Jones (2015) and Luri et al. (2018) to calculate median/uncertainty of the posterior based on the exponentially decreasing space density (EDSD) prior, the posterior of the uniform distance (UD) prior, the method using naive inverse, and transformation method (Smith & Eichhorn 1996).

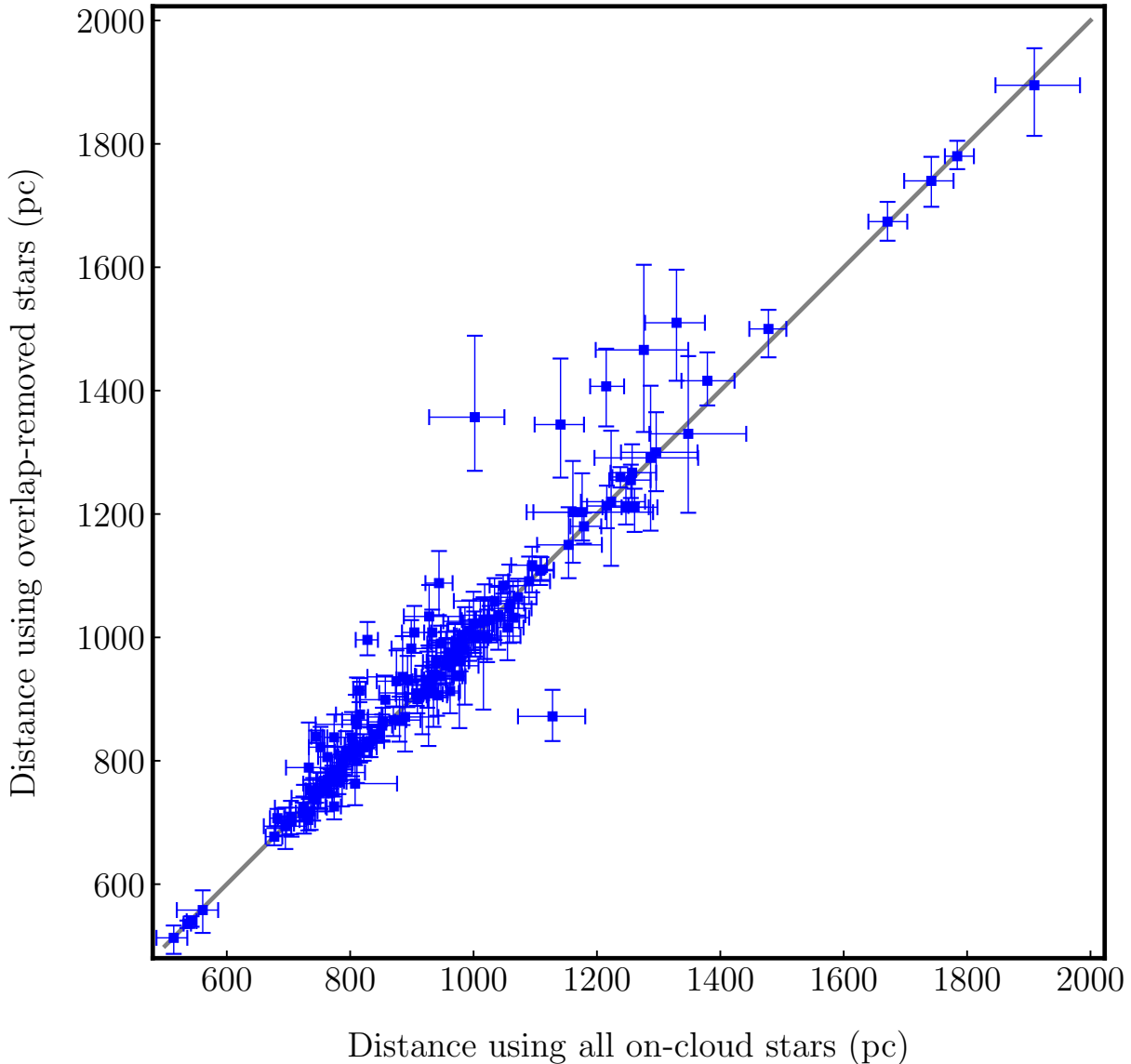


Figure B1. All on-cloud stars (red+black region in Figure 4) versus overlap removed on-cloud stars (red region in Figure 4).

The likelihood function of parallax (ϖ), distance (r) and uncertainty (σ) is,

$$P(\varpi | r, \sigma) = \frac{1}{\sqrt{2\pi}\sigma} \exp\left(-\frac{1}{2\sigma^2} \left(\varpi - \frac{1}{r}\right)^2\right) \quad (\text{C1})$$

Transformation Methods are applied by modifying the parallax ϖ :

$$r^* = \frac{1}{\varpi^*}, \quad \varpi^* = \beta\sigma\phi g_\phi \quad (\text{C2})$$

where

$$\phi = \frac{1}{0.8} \ln\left(1 + e^{\frac{0.8\varpi}{\sigma}}\right) \quad (\text{C3})$$

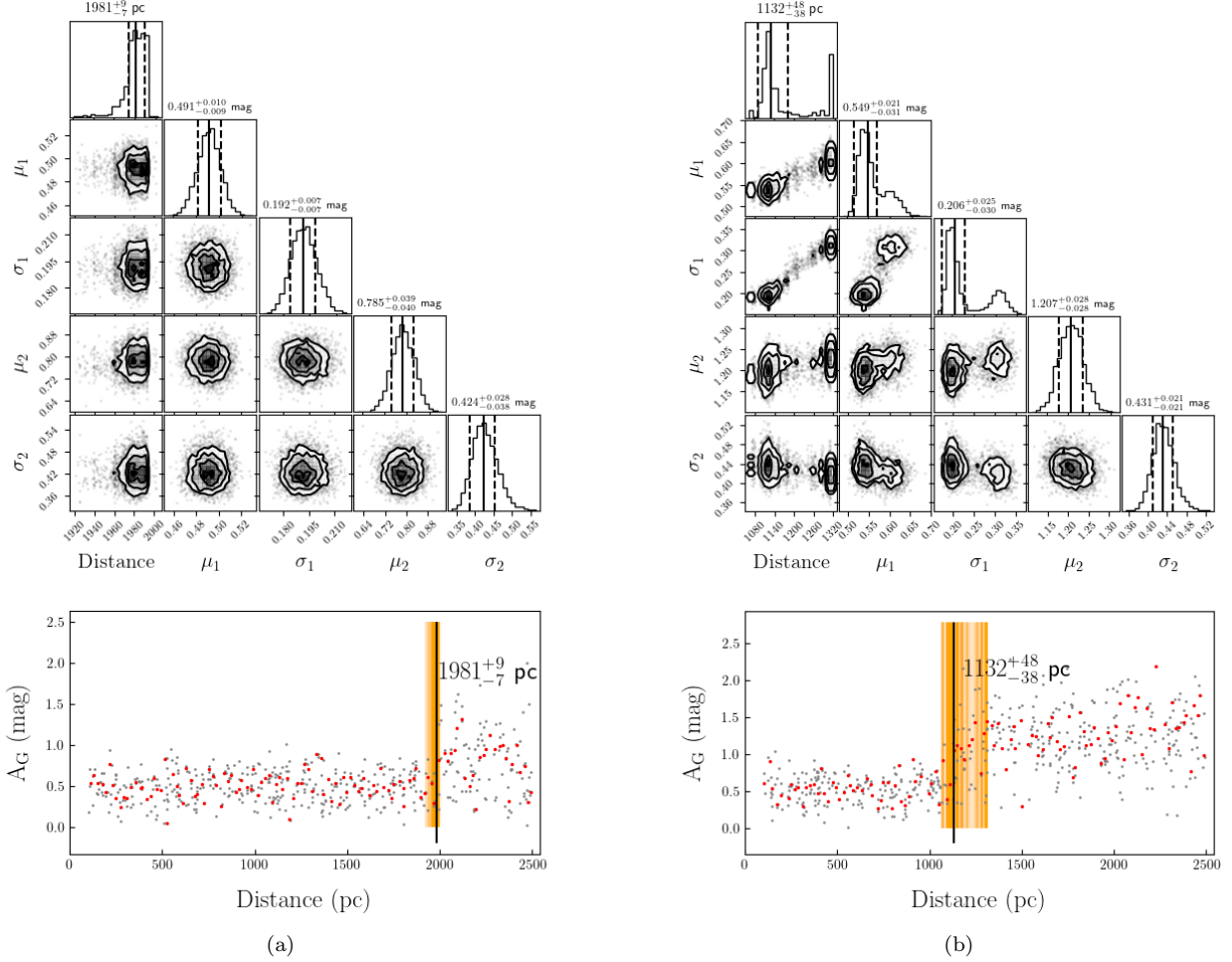


Figure B2. Two examples of measuring distance with mock data based on the Bayes model. Details in the panels can be seen in the caption of Figure 4, but points in lower panel are for the mock data.

and,

$$\begin{cases} g_\phi = 1, & \varpi > 0, \\ g_\phi = e^{-0.605\frac{\varpi^2}{\sigma^2}}, & \varpi \leq 0, \quad \beta = 1.01 \end{cases} \quad (\text{C4})$$

Therefore, the distance module μ^* can be defined as

$$\mu^* = m - \hat{M} = -(5 \log(\hat{\varpi}) + 5) \quad (\text{C5})$$

Finally, the modified parallax ϖ satisfy:

$$\hat{\varpi} = \beta \sigma \left(\frac{1}{e^\phi + e^{\frac{-5\omega}{\sigma}}} + e^\phi \right) \quad (\text{C6})$$

Because our star samples are in a smaller parallax uncertainties ($\leq 20\%$), the discrepancies between different methods can be ignored. Our distances are just like the naive inverse from parallaxes, but the median value and uncertainty are reproduced when we calculate the distance. The correlation of median distances and errors between different methods are presented in Figure C1.

D. INDIVIDUAL CASES IN COMPLICATED EXTINCTION ENVIRONMENT

In addition to the robust distance result confirmed by both Model A and B (class I), some cases are failed to include enough field stars in Model A. For these clouds in the complicated extinction environment, we successfully measured

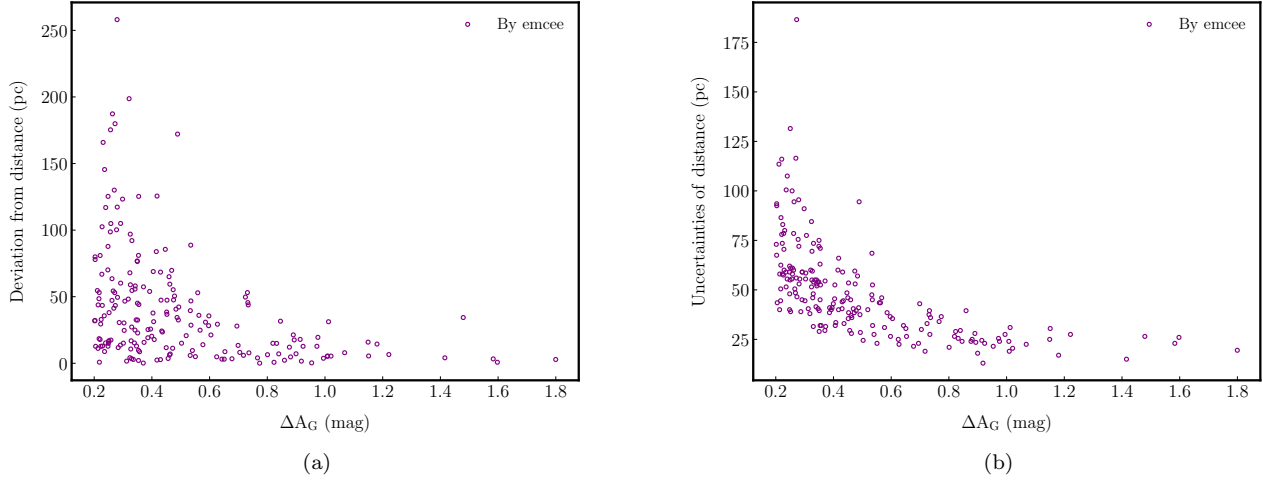


Figure B3. (a) Deviation between distances derived from emcee and preset distances in a relation with increasing ΔA_G . (b) Uncertainties of distances derived from emcee in a relation with increasing ΔA_G .

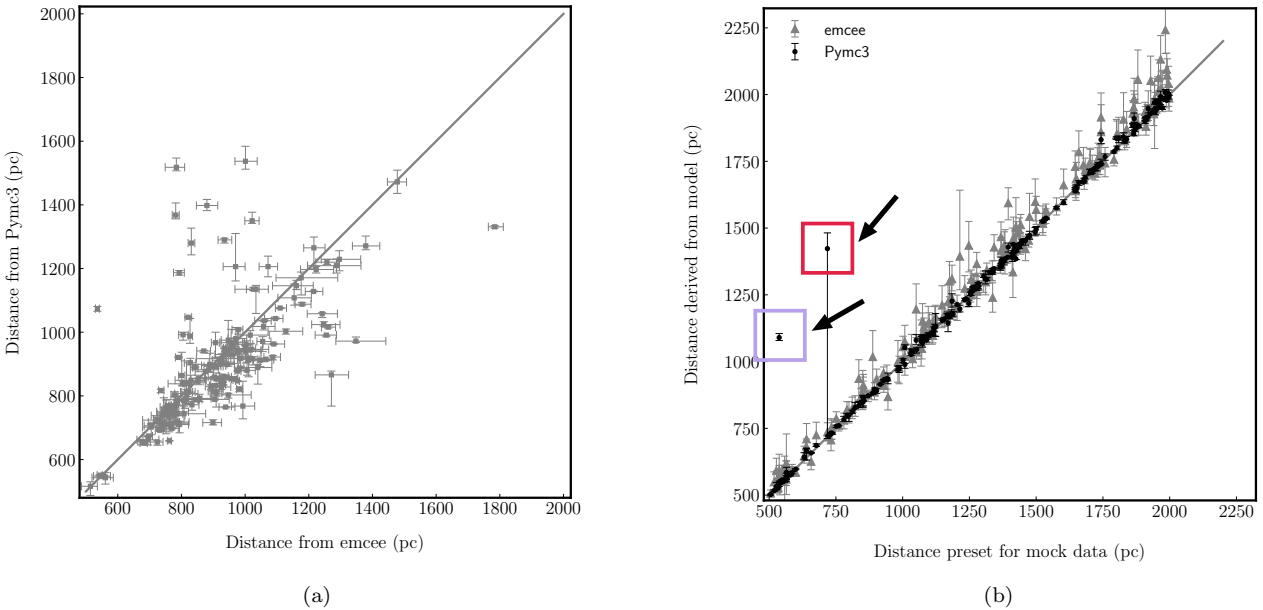


Figure B4. Comparison of distance measurements with different sampling modules. (a) The emcee module versus Pymc3 module in our samples. (b) Distance derived from different modules versus preset distance in mock data.

distances of 22 special cases by Model B because of the prominent extinction on the main body of the clouds. On the other hand, referenced stars near the measured clouds (see orange region in Figure 4b) may share the same but smaller background extinction along the LOS (see Figure 6b). We think distance measurements for these samples alone by Model B are also reliable.

From Figure D1, we can see these clouds match well with the identified gas layers in the text. More clouds with large scale extension are confirmed to be in the 1.3 kpc layer. Especially toward the Cygnus X South region, these clouds

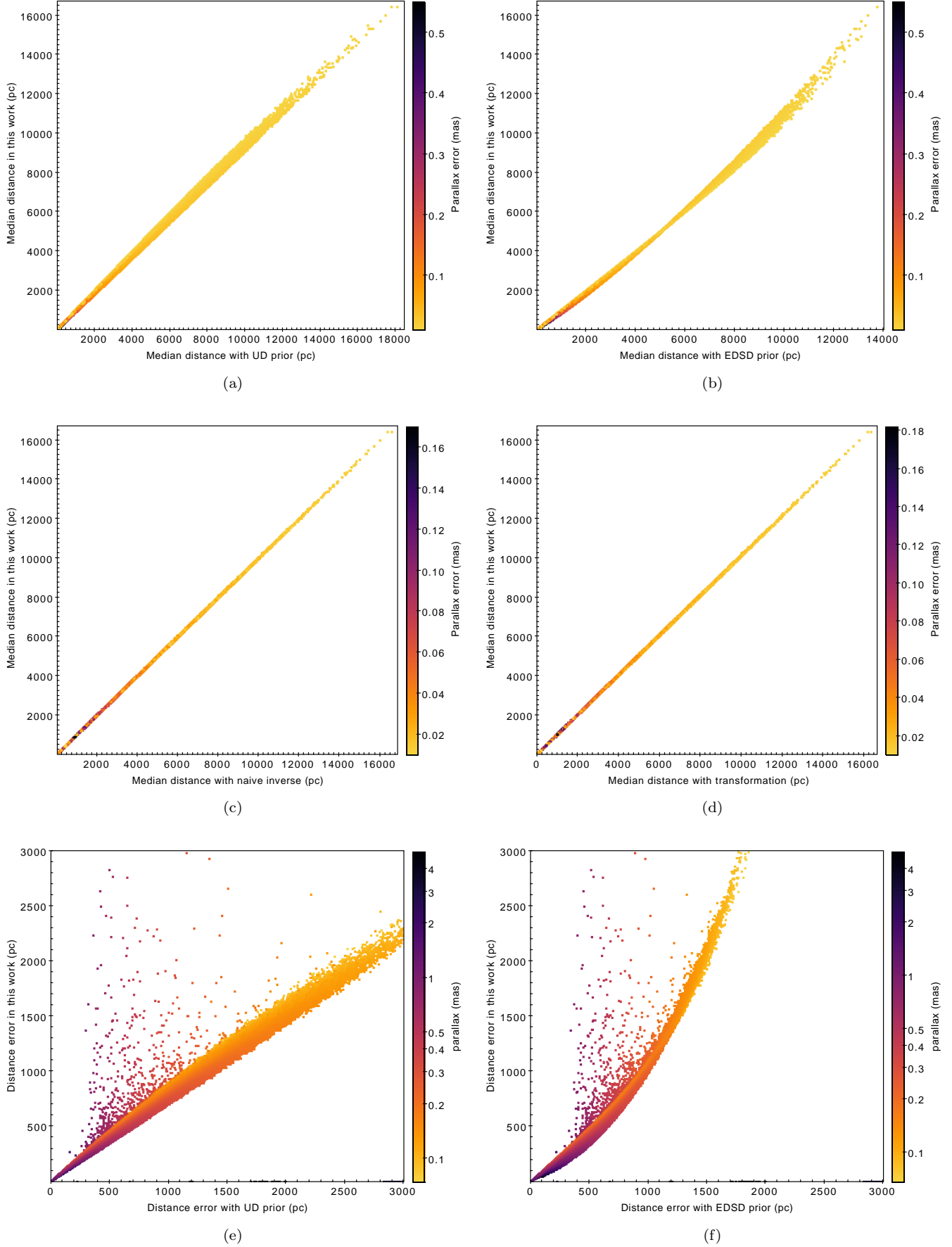


Figure C1. The median and uncertainty of distances derived by different methods compare to this work.

have more contribution on masses, which is consistent with the 1.35 kpc over-density in extinction of the Cygnus X South region (Dharmawardena et al. 2022).

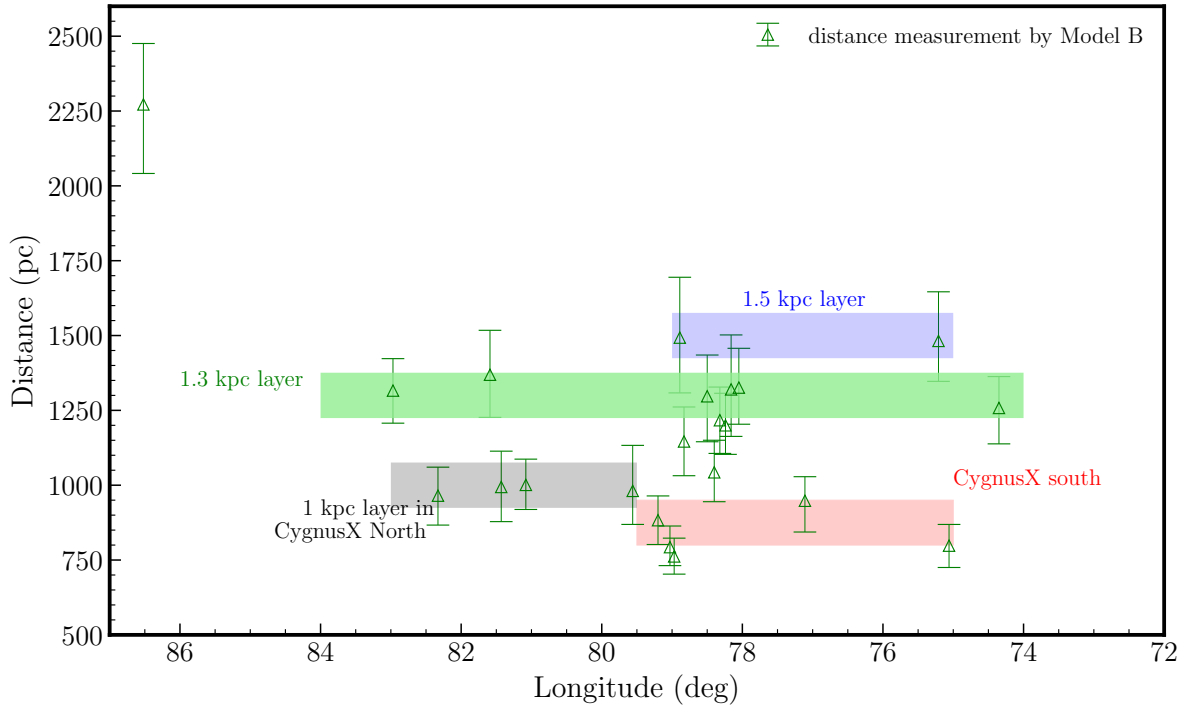


Figure D1. Distances measured by Model B for those 22 clouds in complicated extinction environments. The colorful bands denote gas layers we identified previously.

E. RETRIEVE PART OF FLUX LOSS DURING CLUSTERING

When we make reconstruction using fully fledged clusters from ACORNS, a very small portion of flux missed in the process of clustering. See panel a and b in Figure 2 , the flux loss indicates some Gaussian components are dropped after clustering. We found the dropped components are mainly from three parts. The first is due to large amplitude error from Gaussian fitting. These components are excluded from catalogue before the first loop in clustering. We don't retrieve those components, as it has little influence to the main structure of cloud. The second part is from the components isolated in spatial Euclidean distance or velocity. They could be false identifications by Gaussian fitting, while some are probably from line wings with smaller amplitudes. We drop them because they fail to meet our criteria for fledged clusters. Finally, some extra components are difficult for clustering because of variance of centroid velocity and line width. We find these unassigned components are originated from Gaussian fitting and clustering processes. For some pixels, the over decomposition in GaussPy+ might lead to failure of clustering with an uniform criteria.

We try to retrieve those unassigned components by adding another loop in clustering process. Fully fledged clusters are already formed during first three loops in the clustering process, so further development of the hierarchy is avoided. Next we relax the criteria of velocity and line width to a large extent before last loop, and remove the extra conditions when linking clusters. By using the same strategies of finding the most similar cluster in velocity and line width statistically, those unassigned components are merged into the nearest level of hierarchy. To avoid developing the hierarchy and merging existing clusters together, we skip the “resolving ambiguities” method of ACORNS in final loop we added, but restore the components with smallest variation in equal weight of velocity and line width. Finally, additional 1.5% flux is retrieved in our reconstruction map.

F. YSO CANDIDATES TOWARD THE CYGNUS REGION

Our YSO candidates are selected based on infrared data collected from three surveys: the Spitzer Cygnus-X Legacy Survey (CXLS; Hora et al. 2009), the GLIMPSE360 program (Whitney et al. 2008; Whitney & GLIMPSE360 Team 2009), and the WISE survey (Wright et al. 2010a). We summarise the selection criteria here briefly for each data set, and the analysis of these YSOs will be presented in detail in a future paper (X.-L. Wang, et al. in preparation).

For the CXLS dataset, we select YSO candidates following the prescription in Gutermuth et al. (2009), but update the criteria with the new extinction law from Wang & Chen (2019). The new criteria are,

1. $[I2 - I3] > 0.7$ and $[I1 - I2] > 0.7$;
2. $[I2 - I4] - \sigma_{[I2 - I4]} > 0.5$, $[I1 - I3] - \sigma_{[I1 - I3]} > 0.35$, $[I1 - I2] - \sigma_{[I1 - I2]} > 0.15$, and $[I1 - I3] - \sigma_{[I1 - I3]} \leq 18 \times ([I2 - I4] - \sigma_{[I2 - I4]} - 0.5) + 0.5$;
3. $[K - I1]_0 - \sigma_{[K - I1]} > 0$, $[I1 - I2]_0 - \sigma_{[I1 - I2]} > 0.101$, and $[K - I1]_0 - \sigma_{[K - I1]} > -2.85714 \times ([I1 - I2]_0 - \sigma_{[I1 - I2]} - 0.101) + 0.5$;
4. $[I3 - M1] > 2.5$ for sources without $I4$ measurements;
5. $[I2 - M1] > 2.5$ for sources with no $I3$ and $I4$ measurements.

With these criteria, we selected 24757 as YSO candidates.

For data from the GLIMPSE360 program, we select YSO candidates following Winston et al. (2020), again the extinction law is updated with the Wang & Chen (2019) law. The new criteria are,

1. $0.9375 \times ([J - H] - 0.6 + \sigma_{[J - H]}) + 1.0 + \sigma_{[H - I2]} < [H - I2]$ and $[J - H] > 0$;
2. $0.9811 \times ([H - K] + \sigma_{[H - K]}) + 0.4 + \sigma_{[K - I2]} < [K - I2]$, $[H - K] > 0$, and $[K - I2] > 0.2 + \sigma_{[K - I2]}$;
3. $[I1 - I2]_0 - \sigma_{[I1 - I2]} > 0$, $[K - I1]_0 - \sigma_{[K - I1]} > 0.2 \times [I1 - I2]_0 + 0.3$, and $[K - I1]_0 - \sigma_{[K - I1]} > -([I1 - I2]_0 - \sigma_{[I1 - I2]}) + 0.8$.

With the above criteria, we select 6168 candidates.

For the WISE data, only the first two channels are used in the selection procedure. Since the first two WISE channels have similar central wavelength as the first two IRAC bands, we utilize similar criteria as for the GLIMPSE360 data, but replace $I1$ with $W1$ and $I2$ with $W2$. The selection criteria are,

1. $0.9375 \times ([J - H] - 0.6 + \sigma_{[J - H]}) + 1.0 + \sigma_{[H - W2]} < [H - W2]$ and $[J - H] > 0$;
2. $0.9811 \times ([H - K] + \sigma_{[H - K]}) + 0.4 + \sigma_{[K - W2]} < [K - W2]$, $[H - K] > 0$, and $[K - W2] > 0.2 + \sigma_{[K - W2]}$;
3. $[W1 - W2]_0 - \sigma_{[W1 - W2]} > 0$, $[K - W1]_0 - \sigma_{[K - W1]} > 0.2 \times [W1 - W2]_0 + 0.3$, and $[K - W1]_0 - \sigma_{[K - W1]} > -([W1 - W2]_0 - \sigma_{[W1 - W2]}) + 0.8$.

With the above criteria, we select 25853 candidates.

These three lists of YSO candidates are combined and duplicates are removed, resulting in a total of 50101 YSO candidates. In the current work, we are comparing distribution of YSOs with ^{13}CO traced molecular gas (as displayed in Figure F1 and details in discussion). Therefore we focus on the subsample (22158 candidates) that have Gaia parallaxes. Following Kuhn et al. (2020), possible giant star contaminants are removed, leaving 19220 candidates in our FOV. Finally 11244 candidates are found to be within the interval $[0.5, 3]$ kpc.

REFERENCES

- Abbott, D. C., Biegling, J. H., & Churchwell, E. 1981, ApJ, 250, 645, doi: [10.1086/15942](https://doi.org/10.1086/15942)
- Adler, D. S., & Roberts, William W., J. 1992, ApJ, 384, 95, doi: [10.1086/170854](https://doi.org/10.1086/170854)
- Anderson, L. D., Bania, T. M., Balser, D. S., et al. 2014, ApJS, 212, 1, doi: [10.1088/0067-0049/212/1/1](https://doi.org/10.1088/0067-0049/212/1/1)
- Ando, K., Nagayama, T., Omodaka, T., et al. 2011, PASJ, 63, 45, doi: [10.1093/pasj/63.1.45](https://doi.org/10.1093/pasj/63.1.45)
- Andrae, R., Fouesneau, M., Sordo, R., et al. 2023, A&A, 674, A27, doi: [10.1051/0004-6361/202243462](https://doi.org/10.1051/0004-6361/202243462)
- Astropy Collaboration, Robitaille, T. P., Tollerud, E. J., et al. 2013, A&A, 558, A33, doi: [10.1051/0004-6361/201322068](https://doi.org/10.1051/0004-6361/201322068)
- Astropy Collaboration, Price-Whelan, A. M., Sipőcz, B. M., et al. 2018, AJ, 156, 123, doi: [10.3847/1538-3881/aabc4f](https://doi.org/10.3847/1538-3881/aabc4f)
- Astropy Collaboration, Price-Whelan, A. M., Lim, P. L., et al. 2022, ApJ, 935, 167, doi: [10.3847/1538-4357/ac7c74](https://doi.org/10.3847/1538-4357/ac7c74)
- Bailer-Jones, C. A. L. 2015, PASP, 127, 994, doi: [10.1086/683116](https://doi.org/10.1086/683116)
- Banik, P., & Ghosh, S. K. 2022, ApJL, 931, L30, doi: [10.3847/2041-8213/ac7157](https://doi.org/10.3847/2041-8213/ac7157)
- Beaumont, C. N., Offner, S. S. R., Shetty, R., Glover, S. C. O., & Goodman, A. A. 2013, ApJ, 777, 173, doi: [10.1088/0004-637X/777/2/173](https://doi.org/10.1088/0004-637X/777/2/173)
- Beerer, I. M., Koenig, X. P., Hora, J. L., et al. 2010, ApJ, 720, 679, doi: [10.1088/0004-637X/720/1/679](https://doi.org/10.1088/0004-637X/720/1/679)

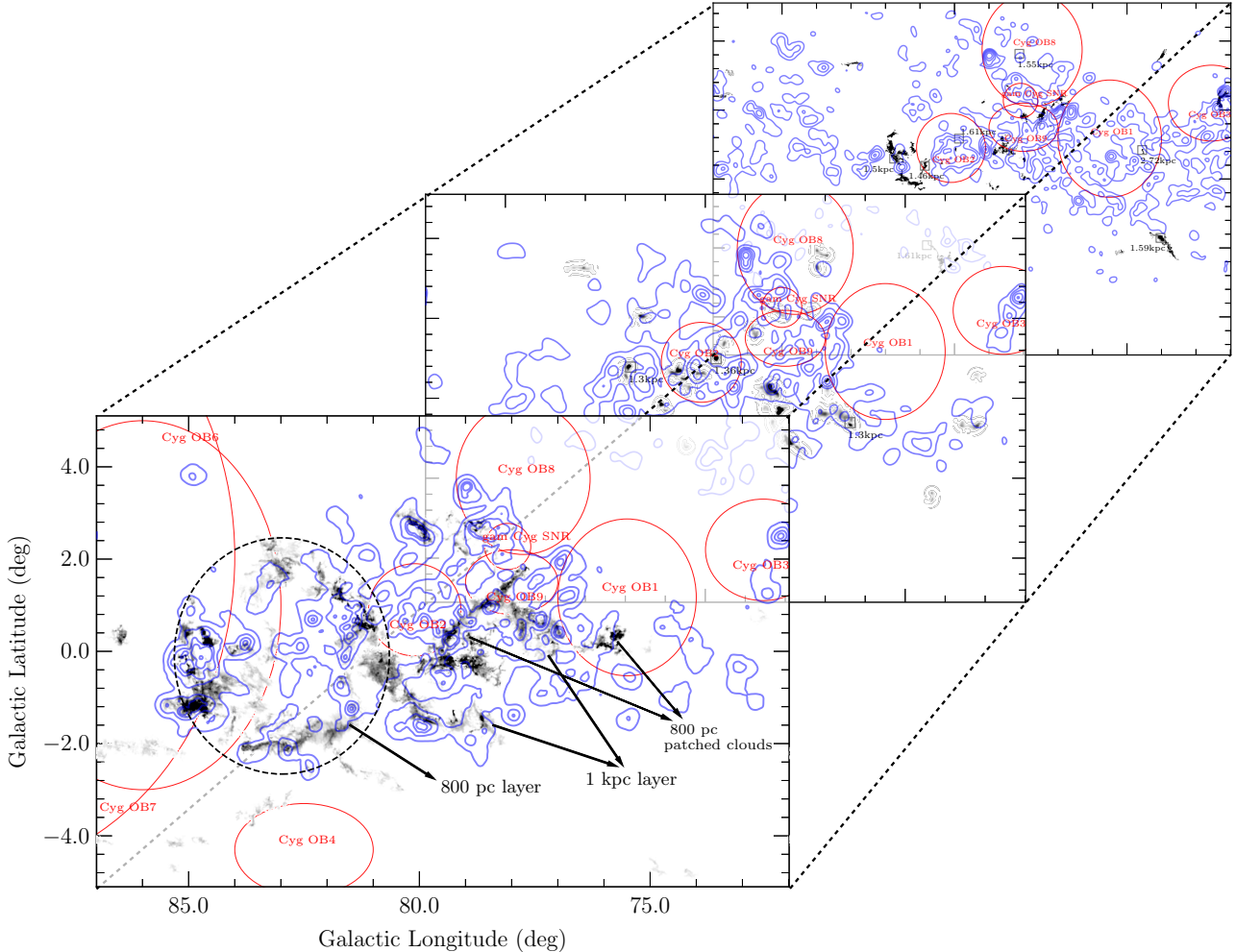


Figure F1. The multiple layers of gas structure with YSO candidates toward the Cygnus region. Similar to Figure 17, grey scale maps are reconstructed by identified MC structures. The dashed ellipse shows a large scale molecular loop with diameter of ~ 56 pc at a distance of 800 pc. Red ellipses show OB associations and SNR, while boxes show the masers in Table 2. The over-density of YSOs candidates is shown as blue contours in each interval. The levels in different intervals are presented as follows: 3σ to 99.5% of the maximum value with an increased step of 25% in a logarithm scale for [500, 1000] pc. 3σ to 99.5% of the maximum value with an increased step of 20% in a logarithm scale for [1000, 1400] pc. 10σ to 99.5% of the maximum value with an increased step of 20% in a logarithm scale for $\gtrsim 1400$ pc. σ (~ 15 deg $^{-1}$) is the noise level of equivalent density map for each intervals.

Berlanas, S. R., Wright, N. J., Herrero, A., Drew, J. E., & Lennon, D. J. 2019, MNRAS, 484, 1838, doi: [10.1093/mnras/stz117](https://doi.org/10.1093/mnras/stz117)

Beuther, H., Wyrowski, F., Menten, K. M., et al. 2022, A&A, 665, A63, doi: [10.1051/0004-6361/202244040](https://doi.org/10.1051/0004-6361/202244040)

Bolatto, A. D., Wolfire, M., & Leroy, A. K. 2013, ARA&A, 51, 207, doi: [10.1146/annurev-astro-082812-140944](https://doi.org/10.1146/annurev-astro-082812-140944)

Bonne, L., Bontemps, S., Schneider, N., et al. 2023, ApJ, 951, 39, doi: [10.3847/1538-4357/acd536](https://doi.org/10.3847/1538-4357/acd536)

Bontemps, S., Motte, F., Csengeri, T., & Schneider, N. 2010, A&A, 524, A18, doi: [10.1051/0004-6361/200913286](https://doi.org/10.1051/0004-6361/200913286)

Bourke, T. L., Garay, G., Lehtinen, K. K., et al. 1997, ApJ, 476, 781, doi: [10.1086/303642](https://doi.org/10.1086/303642)

Bron, E., Daudon, C., Pety, J., et al. 2018, A&A, 610, A12, doi: [10.1051/0004-6361/201731833](https://doi.org/10.1051/0004-6361/201731833)

Burns, R. A., Yamaguchi, Y., Handa, T., et al. 2014, PASJ, 66, 102, doi: [10.1093/pasj/psu094](https://doi.org/10.1093/pasj/psu094)

Cai, J.-J., Yang, J., Zheng, S., et al. 2021, Research in Astronomy and Astrophysics, 21, 304, doi: [10.1088/1674-4527/21/12/304](https://doi.org/10.1088/1674-4527/21/12/304)

Cao, Y., Qiu, K., Zhang, Q., & Li, G.-X. 2022, ApJ, 927, 106, doi: [10.3847/1538-4357/ac4696](https://doi.org/10.3847/1538-4357/ac4696)

- Cao, Y., Qiu, K., Zhang, Q., et al. 2019, ApJS, 241, 1, doi: [10.3847/1538-4365/ab0025](https://doi.org/10.3847/1538-4365/ab0025)
- Cao, Z., Aharonian, F. A., An, Q., et al. 2021, Nature, 594, 33, doi: [10.1038/s41586-021-03498-z](https://doi.org/10.1038/s41586-021-03498-z)
- Cao, Z., Aharonian, F., An, Q., et al. 2023, arXiv e-prints, arXiv:2305.17030, doi: [10.48550/arXiv.2305.17030](https://doi.org/10.48550/arXiv.2305.17030)
- Chen, B. Q., Huang, Y., Yuan, H. B., et al. 2019, MNRAS, 483, 4277, doi: [10.1093/mnras/sty3341](https://doi.org/10.1093/mnras/sty3341)
- Clarke, S. D., Whitworth, A. P., Spowage, R. L., et al. 2018, MNRAS, 479, 1722, doi: [10.1093/mnras/sty1675](https://doi.org/10.1093/mnras/sty1675)
- Colombo, D., Rosolowsky, E., Duarte-Cabral, A., et al. 2019, MNRAS, 483, 4291, doi: [10.1093/mnras/sty3283](https://doi.org/10.1093/mnras/sty3283)
- Comerón, F., Djupvik, A. A., Schneider, N., & Pasquali, A. 2020, A&A, 644, A62, doi: [10.1051/0004-6361/202039188](https://doi.org/10.1051/0004-6361/202039188)
- Comerón, F., Pasquali, A., Rodighiero, G., et al. 2002, A&A, 389, 874, doi: [10.1051/0004-6361:20020648](https://doi.org/10.1051/0004-6361:20020648)
- Creevey, O. L., Sordo, R., Pailler, F., et al. 2023, A&A, 674, A26, doi: [10.1051/0004-6361/202243688](https://doi.org/10.1051/0004-6361/202243688)
- Dame, T. M., Hartmann, D., & Thaddeus, P. 2001, ApJ, 547, 792, doi: [10.1086/318388](https://doi.org/10.1086/318388)
- Dame, T. M., & Thaddeus, P. 1985, ApJ, 297, 751, doi: [10.1086/163573](https://doi.org/10.1086/163573)
- Dame, T. M., Ungerechts, H., Cohen, R. S., et al. 1987, ApJ, 322, 706, doi: [10.1086/165766](https://doi.org/10.1086/165766)
- De Angeli, F., Weiler, M., Montegriffo, P., et al. 2023, A&A, 674, A2, doi: [10.1051/0004-6361/202243680](https://doi.org/10.1051/0004-6361/202243680)
- de Leeuw, J. 1977, Psychometrika, 42, 141, doi: [10.1007/BF02293750](https://doi.org/10.1007/BF02293750)
- Dharmawardena, T. E., Bailer-Jones, C. A. L., Fouesneau, M., & Foreman-Mackey, D. 2022, A&A, 658, A166, doi: [10.1051/0004-6361/202141298](https://doi.org/10.1051/0004-6361/202141298)
- Downes, D., & Rinehart, R. 1966, ApJ, 144, 937, doi: [10.1086/148691](https://doi.org/10.1086/148691)
- Duarte-Cabral, A., Bontemps, S., Motte, F., et al. 2013, A&A, 558, A125, doi: [10.1051/0004-6361/201321393](https://doi.org/10.1051/0004-6361/201321393)
- Duarte-Cabral, A., Colombo, D., Urquhart, J. S., et al. 2021, MNRAS, 500, 3027, doi: [10.1093/mnras/staa2480](https://doi.org/10.1093/mnras/staa2480)
- Egan, M. P., Shipman, R. F., Price, S. D., et al. 1998, ApJL, 494, L199, doi: [10.1086/311198](https://doi.org/10.1086/311198)
- Fang, M., Hillenbrand, L. A., Kim, J. S., et al. 2020, ApJ, 904, 146, doi: [10.3847/1538-4357/abba84](https://doi.org/10.3847/1538-4357/abba84)
- Fitzpatrick, E. L. 1999, PASP, 111, 63, doi: [10.1086/316293](https://doi.org/10.1086/316293)
- Foreman-Mackey, D., Hogg, D. W., Lang, D., & Goodman, J. 2013, PASP, 125, 306, doi: [10.1086/670067](https://doi.org/10.1086/670067)
- Frerking, M. A., Langer, W. D., & Wilson, R. W. 1982, ApJ, 262, 590, doi: [10.1086/160451](https://doi.org/10.1086/160451)
- Ginsburg, A., & Mirocha, J. 2011, PySpecKit: Python Spectroscopic Toolkit, Astrophysics Source Code Library, record ascl:1109.001. <http://ascl.net/1109.001>
- Ginsburg, A., Sokolov, V., de Val-Borro, M., et al. 2022, AJ, 163, 291, doi: [10.3847/1538-3881/ac695a](https://doi.org/10.3847/1538-3881/ac695a)
- Goldsmith, P. F., Heyer, M., Narayanan, G., et al. 2008, ApJ, 680, 428, doi: [10.1086/587166](https://doi.org/10.1086/587166)
- Gong, Y., Ortiz-León, G. N., Rugel, M. R., et al. 2023, A&A, 678, A130, doi: [10.1051/0004-6361/202346102](https://doi.org/10.1051/0004-6361/202346102)
- Gottschalk, M., Kothes, R., Matthews, H. E., Landecker, T. L., & Dent, W. R. F. 2012, A&A, 541, A79, doi: [10.1051/0004-6361/201118600](https://doi.org/10.1051/0004-6361/201118600)
- Gratier, P., Pety, J., Bron, E., et al. 2021, A&A, 645, A27, doi: [10.1051/0004-6361/202037871](https://doi.org/10.1051/0004-6361/202037871)
- Green, G. M., Schlafly, E., Zucker, C., Speagle, J. S., & Finkbeiner, D. 2019, ApJ, 887, 93, doi: [10.3847/1538-4357/ab5362](https://doi.org/10.3847/1538-4357/ab5362)
- Guo, H. L., Chen, B. Q., & Liu, X. W. 2022, MNRAS, 511, 2302, doi: [10.1093/mnras/stac213](https://doi.org/10.1093/mnras/stac213)
- Gutermuth, R. A., Megeath, S. T., Myers, P. C., et al. 2009, ApJS, 184, 18, doi: [10.1088/0067-0049/184/1/18](https://doi.org/10.1088/0067-0049/184/1/18)
- Hacar, A., Tafalla, M., Kauffmann, J., & Kovács, A. 2013, A&A, 554, A55, doi: [10.1051/0004-6361/201220090](https://doi.org/10.1051/0004-6361/201220090)
- Hanson, M. M. 2003, ApJ, 597, 957, doi: [10.1086/378508](https://doi.org/10.1086/378508)
- Hennemann, M., Motte, F., Schneider, N., et al. 2012, A&A, 543, L3, doi: [10.1051/0004-6361/201219429](https://doi.org/10.1051/0004-6361/201219429)
- Henshaw, J. D., Ginsburg, A., Haworth, T. J., et al. 2019, MNRAS, 485, 2457, doi: [10.1093/mnras/stz471](https://doi.org/10.1093/mnras/stz471)
- Henshaw, J. D., Kruijssen, J. M. D., Longmore, S. N., et al. 2020, Nature Astronomy, 4, 1064, doi: [10.1038/s41550-020-1126-z](https://doi.org/10.1038/s41550-020-1126-z)
- Heyer, M., & Dame, T. M. 2015, ARA&A, 53, 583, doi: [10.1146/annurev-astro-082214-122324](https://doi.org/10.1146/annurev-astro-082214-122324)
- Higgs, L. A., Wendker, H. J., & Landecker, T. L. 1994, A&A, 291, 295
- Hiltner, W. A., & Johnson, H. L. 1956, ApJ, 124, 367, doi: [10.1086/146231](https://doi.org/10.1086/146231)
- Hora, J. L., Bontemps, S., Megeath, S. T., et al. 2009, in American Astronomical Society Meeting Abstracts, Vol. 213, American Astronomical Society Meeting Abstracts #213, 356.01
- Hottier, C., Babusiaux, C., & Arenou, F. 2020, Astronomy & Astrophysics, 641, A79, doi: [10.1051/0004-6361/202037573](https://doi.org/10.1051/0004-6361/202037573)
- Hunter, J. D. 2007, Computing in Science and Engineering, 9, 90, doi: [10.1109/MCSE.2007.55](https://doi.org/10.1109/MCSE.2007.55)
- Knödlseder, J. 2000, A&A, 360, 539, doi: [10.48550/arXiv.astro-ph/0007442](https://doi.org/10.48550/arXiv.astro-ph/0007442)
- Kruskal, J. B. 1964, Psychometrika, 29, 115, doi: [10.1007/BF02289694](https://doi.org/10.1007/BF02289694)
- Kuhn, M. A., & Hillenbrand, L. A. 2020, Research Notes of the American Astronomical Society, 4, 224, doi: [10.3847/2515-5172/abd18a](https://doi.org/10.3847/2515-5172/abd18a)

- Kuhn, M. A., Hillenbrand, L. A., Carpenter, J. M., & Avelar Menendez, A. R. 2020, ApJ, 899, 128, doi: [10.3847/1538-4357/aba19a](https://doi.org/10.3847/1538-4357/aba19a)
- Lallement, R., Babusiaux, C., Vergely, J. L., et al. 2019, A&A, 625, A135, doi: [10.1051/0004-6361/201834695](https://doi.org/10.1051/0004-6361/201834695)
- LHAASO Collaboration. 2024, Science Bulletin, 69, 449, doi: [10.1016/j.scib.2023.12.040](https://doi.org/10.1016/j.scib.2023.12.040)
- Li, C., Wang, H., Zhang, M., et al. 2018, ApJS, 238, 10, doi: [10.3847/1538-4365/aad963](https://doi.org/10.3847/1538-4365/aad963)
- Luri, X., Brown, A. G. A., Sarro, L. M., et al. 2018, A&A, 616, A9, doi: [10.1051/0004-6361/201832964](https://doi.org/10.1051/0004-6361/201832964)
- Ma, Y., Wang, H., Li, C., et al. 2021, The Astrophysical Journal Supplement Series, 254, 3, doi: [10.3847/1538-4365/abe85c](https://doi.org/10.3847/1538-4365/abe85c)
- Ma, Y., Wang, H., Li, C., et al. 2021, ApJS, 254, 3, doi: [10.3847/1538-4365/abe85c](https://doi.org/10.3847/1538-4365/abe85c)
- Marchal, A., Miville-Deschénes, M.-A., Orieux, F., et al. 2019, A&A, 626, A101, doi: [10.1051/0004-6361/201935335](https://doi.org/10.1051/0004-6361/201935335)
- Massey, P., & Thompson, A. B. 1991, AJ, 101, 1408, doi: [10.1086/115774](https://doi.org/10.1086/115774)
- Mertsch, P., & Vittino, A. 2021, A&A, 655, A64, doi: [10.1051/0004-6361/202141000](https://doi.org/10.1051/0004-6361/202141000)
- Milam, S. N., Savage, C., Brewster, M. A., Ziurys, L. M., & Wyckoff, S. 2005, ApJ, 634, 1126, doi: [10.1086/497123](https://doi.org/10.1086/497123)
- Miville-Deschénes, M.-A., Murray, N., & Lee, E. J. 2017, ApJ, 834, 57, doi: [10.3847/1538-4357/834/1/57](https://doi.org/10.3847/1538-4357/834/1/57)
- Moscadelli, L., Cesaroni, R., Rioja, M. J., Dodson, R., & Reid, M. J. 2011, A&A, 526, A66, doi: [10.1051/0004-6361/201015641](https://doi.org/10.1051/0004-6361/201015641)
- Motte, F., Bontemps, S., Schilke, P., et al. 2007, A&A, 476, 1243, doi: [10.1051/0004-6361:20077843](https://doi.org/10.1051/0004-6361:20077843)
- Nagahama, T., Mizuno, A., Ogawa, H., & Fukui, Y. 1998, AJ, 116, 336, doi: [10.1086/300392](https://doi.org/10.1086/300392)
- Nagayama, T., Omodaka, T., Handa, T., et al. 2015, PASJ, 67, 66, doi: [10.1093/pasj/psu133](https://doi.org/10.1093/pasj/psu133)
- Orellana, R. B., De Biasi, M. S., & Paíz, L. G. 2021, MNRAS, 502, 6080, doi: [10.1093/mnras/stab457](https://doi.org/10.1093/mnras/stab457)
- Ortiz-León, G. N., Menten, K. M., Brunthaler, A., et al. 2021, A&A, 651, A87, doi: [10.1051/0004-6361/202140817](https://doi.org/10.1051/0004-6361/202140817)
- Pan, H.-A., Fujimoto, Y., Tasker, E. J., et al. 2015, MNRAS, 453, 3082, doi: [10.1093/mnras/stv1843](https://doi.org/10.1093/mnras/stv1843)
- Panopoulou, G. V., & Lenz, D. 2020, ApJ, 902, 120, doi: [10.3847/1538-4357/abb6f5](https://doi.org/10.3847/1538-4357/abb6f5)
- Pedregosa, F., Varoquaux, G., Gramfort, A., et al. 2011, Journal of Machine Learning Research, 12, 2825, doi: [10.48550/arXiv.1201.0490](https://doi.org/10.48550/arXiv.1201.0490)
- Peek, J. E. G., Tchernyshyov, K., & Miville-Deschenes, M.-A. 2022, ApJ, 925, 201, doi: [10.3847/1538-4357/ac3f34](https://doi.org/10.3847/1538-4357/ac3f34)
- Petzler, A., Dawson, J. R., & Wardle, M. 2021, ApJ, 923, 261, doi: [10.3847/1538-4357/ac2f42](https://doi.org/10.3847/1538-4357/ac2f42)
- Pineda, J. L., Goldsmith, P. F., Chapman, N., et al. 2010, ApJ, 721, 686, doi: [10.1088/0004-637X/721/1/686](https://doi.org/10.1088/0004-637X/721/1/686)
- Quintana, A. L., & Wright, N. J. 2021, MNRAS, 508, 2370, doi: [10.1093/mnras/stab2663](https://doi.org/10.1093/mnras/stab2663)
- . 2022, MNRAS, 515, 687, doi: [10.1093/mnras/stac1526](https://doi.org/10.1093/mnras/stac1526)
- Rastorguev, A. S., Zabolotskikh, M. V., Sitnik, T. G., et al. 2023, Astrophysical Bulletin, 78, 119, doi: [10.1134/S1990341323020050](https://doi.org/10.1134/S1990341323020050)
- Reid, M. J., Menten, K. M., Brunthaler, A., et al. 2019, ApJ, 885, 131, doi: [10.3847/1538-4357/ab4a11](https://doi.org/10.3847/1538-4357/ab4a11)
- Reipurth, B., & Schneider, N. 2008, in Handbook of Star Forming Regions, Volume I, ed. B. Reipurth, Vol. 4, 36
- Rice, T. S., Goodman, A. A., Bergin, E. A., Beaumont, C., & Dame, T. M. 2016, ApJ, 822, 52, doi: [10.3847/0004-637X/822/1/52](https://doi.org/10.3847/0004-637X/822/1/52)
- Riener, M., Kainulainen, J., Beuther, H., et al. 2020, A&A, 633, A14, doi: [10.1051/0004-6361/201936814](https://doi.org/10.1051/0004-6361/201936814)
- Riener, M., Kainulainen, J., Henshaw, J. D., et al. 2019, A&A, 628, A78, doi: [10.1051/0004-6361/201935519](https://doi.org/10.1051/0004-6361/201935519)
- Rygl, K., Brunthaler, A., Menten, K. M., et al. 2011, in Proceedings of 10th European VLBI Network Symposium and EVN Users Meeting: VLBI and the new generation of radio arrays — PoS(10th EVN Symposium) (Manchester, UK: Sissa Medialab), 103, doi: [10.22323/1.125.0103](https://doi.org/10.22323/1.125.0103)
- Rygl, K. L. J., Brunthaler, A., Sanna, A., et al. 2012, A&A, 539, A79, doi: [10.1051/0004-6361/201118211](https://doi.org/10.1051/0004-6361/201118211)
- Salvatier, J., Wiecki, T. V., & Fonnesbeck, C. 2016, PyMC3: Python probabilistic programming framework, Astrophysics Source Code Library, record ascl:1610.016, <http://ascl.net/1610.016>
- Schneider, N., Bontemps, S., Simon, R., et al. 2006, A&A, 458, 855, doi: [10.1051/0004-6361:20065088](https://doi.org/10.1051/0004-6361:20065088)
- Schneider, N., Csengeri, T., Bontemps, S., et al. 2010, A&A, 520, A49, doi: [10.1051/0004-6361/201014481](https://doi.org/10.1051/0004-6361/201014481)
- Schneider, N., Simon, R., Bontemps, S., Comerón, F., & Motte, F. 2007, A&A, 474, 873, doi: [10.1051/0004-6361:20077540](https://doi.org/10.1051/0004-6361:20077540)
- Schneider, N., Bontemps, S., Motte, F., et al. 2016, A&A, 591, A40, doi: [10.1051/0004-6361/201628328](https://doi.org/10.1051/0004-6361/201628328)
- Schneider, N., Bonne, L., Bontemps, S., et al. 2023, Nature Astronomy, doi: [10.1038/s41550-023-01901-5](https://doi.org/10.1038/s41550-023-01901-5)
- Schuller, F., Csengeri, T., Urquhart, J. S., et al. 2017, A&A, 601, A124, doi: [10.1051/0004-6361/201628933](https://doi.org/10.1051/0004-6361/201628933)
- Shan, W., Yang, J., Shi, S., et al. 2012, IEEE Transactions on Terahertz Science and Technology, 2, 593, doi: [10.1109/TTHZ.2012.2213818](https://doi.org/10.1109/TTHZ.2012.2213818)
- Shetty, R., Collins, D. C., Kauffmann, J., et al. 2010, ApJ, 712, 1049, doi: [10.1088/0004-637X/712/2/1049](https://doi.org/10.1088/0004-637X/712/2/1049)

- Smith, Haywood, J., & Eichhorn, H. 1996, MNRAS, 281, 211, doi: [10.1093/mnras/281.1.211](https://doi.org/10.1093/mnras/281.1.211)
- Sokolov, V., Pineda, J. E., Buchner, J., & Caselli, P. 2020, ApJL, 892, L32, doi: [10.3847/2041-8213/ab8018](https://doi.org/10.3847/2041-8213/ab8018)
- Staude, H. J., Lenzen, R., Dyck, H. M., & Schmidt, G. D. 1982, ApJ, 255, 95, doi: [10.1086/159807](https://doi.org/10.1086/159807)
- Straizys, V., Kazlauskas, A., Vansevicius, V., & Cernis, K. 1993, Baltic Astronomy, 2, 171, doi: [10.1515/astro-1993-0202](https://doi.org/10.1515/astro-1993-0202)
- Su, Y., Yang, J., Zhang, S., et al. 2019, ApJS, 240, 9, doi: [10.3847/1538-4365/aaf1c8](https://doi.org/10.3847/1538-4365/aaf1c8)
- Su, Y., Yang, J., Yan, Q.-Z., et al. 2020, ApJ, 893, 91, doi: [10.3847/1538-4357/ab7fff](https://doi.org/10.3847/1538-4357/ab7fff)
- Sun, L., Chen, X., Fang, M., et al. accepted by AAS, 2024
- Sun, M., Jiang, B., Zhao, H., & Ren, Y. 2021a, ApJS, 256, 46, doi: [10.3847/1538-4365/ac1601](https://doi.org/10.3847/1538-4365/ac1601)
- Sun, Y., Yang, J., Yan, Q.-Z., et al. 2021b, ApJS, 256, 32, doi: [10.3847/1538-4365/ac11fe](https://doi.org/10.3847/1538-4365/ac11fe)
- Takekoshi, T., Fujita, S., Nishimura, A., et al. 2019, ApJ, 883, 156, doi: [10.3847/1538-4357/ab3a55](https://doi.org/10.3847/1538-4357/ab3a55)
- Umemoto, T., Minamidani, T., Kuno, N., et al. 2017, PASJ, 69, 78, doi: [10.1093/pasj/psx061](https://doi.org/10.1093/pasj/psx061)
- Wang, C., Feng, H., Yang, J., et al. 2023, AJ, 165, 106, doi: [10.3847/1538-3881/acafee](https://doi.org/10.3847/1538-3881/acafee)
- Wang, S., & Chen, X. 2019, ApJ, 877, 116, doi: [10.3847/1538-4357/ab1c61](https://doi.org/10.3847/1538-4357/ab1c61)
- Wendker, H. J., Higgs, L. A., & Landecker, T. L. 1991, A&A, 241, 551
- Whitney, B., & GLIMPSE360 Team. 2009, in American Astronomical Society Meeting Abstracts, Vol. 214, American Astronomical Society Meeting Abstracts #214, 210.01
- Whitney, B., Arendt, R., Babler, B., et al. 2008, GLIMPSE360: Completing the Spitzer Galactic Plane Survey, Spitzer Proposal ID #60020
- Wilson, T. L., Rohlfs, K., & Hüttemeister, S. 2009, Tools of Radio Astronomy, doi: [10.1007/978-3-540-85122-6](https://doi.org/10.1007/978-3-540-85122-6)
- Winston, E., Hora, J. L., & Tolls, V. 2020, AJ, 160, 68, doi: [10.3847/1538-3881/ab99c8](https://doi.org/10.3847/1538-3881/ab99c8)
- Wright, E. L., Eisenhardt, P. R. M., Mainzer, A. K., et al. 2010a, AJ, 140, 1868, doi: [10.1088/0004-6256/140/6/1868](https://doi.org/10.1088/0004-6256/140/6/1868)
- Wright, N. J., Drake, J. J., Drew, J. E., & Vink, J. S. 2010b, ApJ, 713, 871, doi: [10.1088/0004-637X/713/2/871](https://doi.org/10.1088/0004-637X/713/2/871)
- Wright, N. J., Drew, J. E., & Mohr-Smith, M. 2015, MNRAS, 449, 741, doi: [10.1093/mnras/stv323](https://doi.org/10.1093/mnras/stv323)
- Xu, Y., Li, J. J., Reid, M. J., et al. 2013, ApJ, 769, 15, doi: [10.1088/0004-637X/769/1/15](https://doi.org/10.1088/0004-637X/769/1/15)
- Xu, Y., Reid, M., Dame, T., et al. 2016, Science Advances, 2, e1600878, doi: [10.1126/sciadv.1600878](https://doi.org/10.1126/sciadv.1600878)
- Yamagishi, M., Nishimura, A., Fujita, S., et al. 2018, ApJS, 235, 9, doi: [10.3847/1538-4365/aaab4b](https://doi.org/10.3847/1538-4365/aaab4b)
- Yan, Q.-Z., Yang, J., Su, Y., Sun, Y., & Wang, C. 2020, ApJ, 898, 80, doi: [10.3847/1538-4357/ab9f9c](https://doi.org/10.3847/1538-4357/ab9f9c)
- Yan, Q.-Z., Yang, J., Su, Y., et al. 2021a, ApJ, 922, 8, doi: [10.3847/1538-4357/ac214f](https://doi.org/10.3847/1538-4357/ac214f)
- Yan, Q.-Z., Yang, J., Sun, Y., Su, Y., & Xu, Y. 2019a, ApJ, 885, 19, doi: [10.3847/1538-4357/ab458e](https://doi.org/10.3847/1538-4357/ab458e)
- Yan, Q.-Z., Yang, J., Sun, Y., et al. 2021b, A&A, 645, A129, doi: [10.1051/0004-6361/202039768](https://doi.org/10.1051/0004-6361/202039768)
- Yan, Q.-Z., Yang, J., Yang, S., Sun, Y., & Wang, C. 2021c, ApJ, 910, 109, doi: [10.3847/1538-4357/abe628](https://doi.org/10.3847/1538-4357/abe628)
- Yan, Q.-Z., Zhang, B., Xu, Y., et al. 2019b, A&A, 624, A6, doi: [10.1051/0004-6361/201834337](https://doi.org/10.1051/0004-6361/201834337)
- Yu, B., Chen, B. Q., Jiang, B. W., & Zijlstra, A. 2019, MNRAS, 488, 3129, doi: [10.1093/mnras/stz1940](https://doi.org/10.1093/mnras/stz1940)
- Yuan, L., Yang, J., Du, F., et al. 2022, ApJS, 261, 37, doi: [10.3847/1538-4365/ac739f](https://doi.org/10.3847/1538-4365/ac739f)
- . 2023, ApJ, 958, 7, doi: [10.3847/1538-4357/acf9ef](https://doi.org/10.3847/1538-4357/acf9ef)
- Zamora-Avilés, M., Ballesteros-Paredes, J., & Hartmann, L. W. 2017, MNRAS, 472, 647, doi: [10.1093/mnras/stx1995](https://doi.org/10.1093/mnras/stx1995)
- Zhang, B., Reid, M. J., Menten, K. M., Zheng, X. W., & Brunthaler, A. 2012, A&A, 544, A42, doi: [10.1051/0004-6361/201219587](https://doi.org/10.1051/0004-6361/201219587)
- Zhang, S., Xu, Y., & Yang, J. 2014, AJ, 147, 46, doi: [10.1088/0004-6256/147/3/46](https://doi.org/10.1088/0004-6256/147/3/46)
- Zhang, S., Yang, J., Xu, Y., et al. 2020, ApJS, 248, 15, doi: [10.3847/1538-4365/ab879a](https://doi.org/10.3847/1538-4365/ab879a)
- Zhao, H., Jiang, B., Li, J., et al. 2020, ApJ, 891, 137, doi: [10.3847/1538-4357/ab75ef](https://doi.org/10.3847/1538-4357/ab75ef)
- Zucker, C., Alves, J., Goodman, A., Meingast, S., & Galli, P. 2023, in Astronomical Society of the Pacific Conference Series, Vol. 534, Protostars and Planets VII, ed. S. Inutsuka, Y. Aikawa, T. Muto, K. Tomida, & M. Tamura, 43, doi: [10.48550/arXiv.2212.00067](https://doi.org/10.48550/arXiv.2212.00067)
- Zucker, C., Speagle, J. S., Schlafly, E. F., et al. 2020, A&A, 633, A51, doi: [10.1051/0004-6361/201936145](https://doi.org/10.1051/0004-6361/201936145)
- . 2019, ApJ, 879, 125, doi: [10.3847/1538-4357/ab2388](https://doi.org/10.3847/1538-4357/ab2388)